

# Atomic traps for efficient state detection of a single atom

**Diplomarbeit**

im Studiengang Diplom Physik

angefertigt an der Fakultät für Physik

der Ludwig-Maximilians-Universität München

Arbeitsgruppe Prof. Dr. Harald Weinfurter

von

**Michael Krug**

München, den 20. Mai 2007

Erstgutachter: Prof. Dr. H. Weinfurter

Zweitgutachter: Prof. Dr. R. Kersting



”Physics is like sex: sure, it may  
give some practical results, but  
that’s not why we do it.”

*Richard P. Feynman*

# Contents

<b>1</b>	<b>Introduction</b>	<b>1</b>
<b>2</b>	<b>Theory</b>	<b>4</b>
2.1	Entanglement . . . . .	4
2.1.1	Spin-1/2 system . . . . .	4
2.2	Bell's inequality . . . . .	7
2.2.1	Einstein-Podolski-Rosen paradox . . . . .	7
2.2.2	Bell's inequality . . . . .	9
2.2.3	Quantum mechanical predictions . . . . .	12
2.2.4	Loopholes . . . . .	13
2.2.5	Applications of entanglement . . . . .	15
2.3	Quantum mechanical basics of $^{87}\text{Rb}$ . . . . .	18
2.3.1	Fine structure . . . . .	18
2.3.2	Hyperfine structure . . . . .	19
2.3.3	Zeeman-effect . . . . .	20
2.4	Interaction of light with a single atom . . . . .	20
2.4.1	The interaction Hamiltonian . . . . .	22
2.4.2	Rabi oscillations . . . . .	23
2.4.3	Optical Bloch equations . . . . .	24
2.5	Trapping of a single atom . . . . .	28
2.5.1	Magneto-optical trap . . . . .	28
2.5.2	Optical dipole trap . . . . .	30
<b>3</b>	<b>From theory to experiment</b>	<b>38</b>
3.1	Decay-scheme . . . . .	38

## Contents

---

3.2	State detection of a single atom . . . . .	40
3.2.1	STIRAP . . . . .	40
3.2.2	Ionisation . . . . .	47
3.2.3	Detection of the ionisation fragments . . . . .	50
<b>4</b>	<b>Experimental setup</b>	<b>53</b>
4.1	Vacuum chamber . . . . .	55
4.2	Laser system . . . . .	58
4.2.1	Cooling and repump laser . . . . .	58
4.2.2	Dipole trap Laser . . . . .	61
4.2.3	Ionisation Laser . . . . .	62
4.3	Magneto-optical trap . . . . .	64
4.3.1	Optics . . . . .	64
4.3.2	Quadrupole coils . . . . .	66
4.4	Determination of the atom number . . . . .	67
4.5	Optical dipole trap . . . . .	68
4.5.1	Experimental results . . . . .	74
<b>5</b>	<b>Summary and outlook</b>	<b>79</b>
<b>A</b>	<b>Appendix</b>	<b>81</b>
A.1	Addition of angular momenta . . . . .	81
A.2	Spontaneous decay as a source of entanglement . . . . .	83
A.2.1	Spontaneous decay in a two-level system . . . . .	83
A.3	The mobile lab . . . . .	86
A.4	Laser system . . . . .	88
A.5	Power stabilisation . . . . .	90
A.6	Photos of the setup . . . . .	91
	<b>Bibliography</b>	<b>93</b>



# 1 Introduction

*Was the world wave function waiting to jump for thousands of millions of years until a single-celled living creature appeared? Or did it have to wait a little longer for some more highly qualified measurer- with a Ph.D.?* asked J.S. Bell [1] in 1981 and pointed out the main focus in the understanding of quantum mechanics. Especially entangled states [2], which means non-separable two or many particle states, give raise to vivid discussions. Many of the founders of quantum mechanics, namely Schrödinger and Einstein [2, 3], opposed to the Copenhagen interpretation of quantum mechanics proposed by Bohr et. al. [4]. This interpretation reveals that the observer forms a single, indivisibly combined system with the object to be observed. This system can not be analysed correctly by dividing it into separate and distinct parts. As a consequence, quantum theory generally makes no prediction about the result of a single measurement, only the probability of the result can be calculated [5].

Contrary to this Einstein intended to rescue local realism [3] and in an Gedankenexperiment he motivated, together with Podolsky and Rosen [3], the extension of quantum mechanics by additional parameters that nowadays are called *local hidden variables* (LHV). Later on, Bell was able to predict that there is an upper bound for the expectation value of spin correlation measurements using a simplified version of the EPR Gedankenexperiment by Bohm [5]. This upper bound is not conform with the predictions of quantum mechanics [6]. Bell distilled inequalities that revealed parameters, which could be tested by experiments. A violation of these inequalities could now reveal whether nature obeys local realism or not.

The first experiments testing Bell's inequality were performed using entangled photon pairs generated in the cascade decay of calcium atoms [7, 8]. In an improved experiment Aspect et al. [9, 10] also addressed, for the first time, the problem of

locality by performing a fast, though non-random switching of the measurement bases [11].

Up to now, there have been many experiments testing Bell's inequality and practically all observations were in favour of quantum mechanics. However, all these experiments were subject to two major loopholes and therefore still allow in principle a local realistic description of the experiment.

The first one is the so-called locality loophole. It considers a possible remote interaction between two distant measurement apparatus or two entangled particles [5] as long as the two measurement events are not space-like separated [1]. In 1998, Weihs et. al. [12] performed the first experimental violation of Bell's inequality under strict relativistic locality conditions with entangled photons. With this experiment the locality loophole was closed, but due to the low detection efficiency of single photons, one still has to assume that the detected sample of photons behaves like the whole ensemble. This *fair sampling* assumption gives rise to the next loophole, the so-called detection loophole. The detection loophole describes, that the measured sub-ensemble behaves according to quantum mechanics while the entire ensemble still can be described by local realistic theories.

Atoms can be detected with high efficiency [13, 14] in contrast to photons. In 2001 Rowe et. al. [14] performed a test of Bell's inequality using two entangled ions and were thus able to close the detection loophole. However the distance between the two ions in this experiment was vanishingly small, so the locality loophole was left open.

Still, a final loophole free test of Bell's inequality has to be performed because no experiment has closed both loopholes simultaneously until now. Hence, strictly speaking, a local realistic description of nature can not be fully ruled out so far.

One possibility to perform such a loophole free test could be to combine the high detection efficiency of the internal states of single atoms [15, 16] with a space-like separation of two independent setups. The key ingredient for such a test is the entanglement between atoms and photons [13, 16]. In this way, one can combine long-distance entanglement mediated by the photons and the high detection efficiency of the atomic states.

Now, in the onset of the experiment described in this thesis, we start with two

---

atoms at a distance far enough to ensure space-like separation. Next, each atom is entangled with a single photon and the two photons are guided to an intermediate location. A Bell state measurement on the photons swaps the entanglement [17, 18] onto the atoms and we can detect the state of each atom with high efficiency. To close the locality loophole, the detection of the internal state of the atoms must be faster than the speed of light times the distance between the atoms. This can be realised in the future via an enhanced, so-called ionisation detection of the atoms.

**Overview** The work done in this thesis contributes mainly to the grand project of a loophole free test of Bell's inequality. The necessary steps for the trapping and detection of a single atom in an improved optical dipole trap are described. This new, second trap allows a significantly tighter focus and thus higher collection efficiency compared to the previous setup [13, 15, 16, 19].

The second chapter gives a short introduction into the main physical background important for our experiment. In the third chapter the decay used to generate atom-photon entanglement and estimations concerning the planned, improved detection scheme for the internal atomic states now based on ionisation detection are explained. The fourth chapter describes the main experimental steps achieved during this thesis. Hereby, the focus lies on the setup of the magneto-optical trap and the optical dipole trap which will be used for the trapping of a single atom. Furthermore, the laser system, necessary for trapping, detection and ionisation of the atom, will be presented. At the end of the chapter, first results observing a single atom in the optical dipole trap will be discussed. Finally, the fifth chapter sums up the calculations and the experimental results towards a final loophole-free test of Bell's inequality.

# 2 Theory

The long-term goal of our experiment is the accomplishment of a loophole free test of Bell's inequality with two entangled atoms. Therefore this chapter will give a short overview about entanglement [2, 5] and the derivation of Bell's inequality [6] inspired by the Einstein-Podolsky-Rosen paradoxon [3]. The second part gives an overview about the atomic structure of  $^{87}\text{Rb}$  [20] and its interaction with light [21, 22].

## 2.1 Entanglement

I will describe in this chapter the properties of spin-1/2 systems (qubits) within the framework of quantum mechanics. The objections of Einstein, Podolski and Rosen in their famous paper [3] to the Copenhagen interpretation of quantum mechanics [4] are presented and a derivation of Bell's inequality shows that the prediction of quantum mechanics can not agree with the assumption of local realism. The next step will be a possible application of entanglement of two qubits and furthermore entanglement swapping and teleportation [18].

### 2.1.1 Spin-1/2 system

In contrast to a classical bit, in quantum mechanics a two-level system, the so-called qubit, is allowed to be in a superposition state, which can be written as

$$|\Psi\rangle = \alpha |0\rangle + \beta |1\rangle \tag{2.1}$$

with  $\alpha, \beta \in \mathbb{C}$  are the quantum mechanical amplitudes. If we consider a spin-1/2 system we can write the qubit as

$$|\Psi\rangle = \alpha |\uparrow\rangle + \beta |\downarrow\rangle. \quad (2.2)$$

The probability to measure  $|\uparrow\rangle(|\downarrow\rangle)$  is given by  $|\alpha|^2$  ( $|\beta|^2$ ), respectively, and the normalisation condition requires  $|\alpha|^2 + |\beta|^2 = 1$ . A global phase does not affect the outcome of the measurement, so we can rewrite eq. 2.2

$$|\Psi\rangle = \cos \frac{\theta}{2} |\uparrow\rangle + e^{i\phi} \sin \frac{\theta}{2} |\downarrow\rangle \quad (2.3)$$

with  $\theta, \phi \in \mathbb{R}$ .

In this way every quantum mechanical system with a two-dimensional degree of freedom is equivalent to a qubit. Its state can be represented on the surface of a Bloch sphere [23], determined by the angles  $\theta$  and  $\phi$  (see fig. 2.1).

The measurement process in quantum mechanics is described as the projection of  $|\Psi\rangle$  onto the eigenstates of a Hermitian operator  $\mathcal{A}$  with the expectation value  $\langle \mathcal{A} \rangle = \langle \Psi | \mathcal{A} | \Psi \rangle$ . For a spin-1/2 system the Pauli-matrices

$$\sigma_x = \begin{pmatrix} 0 & 1 \\ 1 & 0 \end{pmatrix}, \sigma_y = \begin{pmatrix} 0 & i \\ -i & 0 \end{pmatrix}, \sigma_z = \begin{pmatrix} 1 & 0 \\ 0 & -1 \end{pmatrix} \quad (2.4)$$

form a set of complementary operators with the eigenvalues  $\pm 1$  and the corresponding eigenstates

$$|\uparrow\rangle_x = \sqrt{\frac{1}{2}} (|\downarrow\rangle_z + |\uparrow\rangle_z) \quad (2.5)$$

$$|\downarrow\rangle_x = \sqrt{\frac{1}{2}} (|\downarrow\rangle_z - |\uparrow\rangle_z) \quad (2.6)$$

$$|\uparrow\rangle_y = \sqrt{\frac{1}{2}} (|\downarrow\rangle_z + i |\uparrow\rangle_z) \quad (2.7)$$

$$|\downarrow\rangle_y = \sqrt{\frac{1}{2}} (i |\downarrow\rangle_z + |\uparrow\rangle_z) \quad (2.8)$$

where  $|\uparrow\rangle_z$  and  $|\downarrow\rangle_z$  are the eigenstates of  $\sigma_z$ .

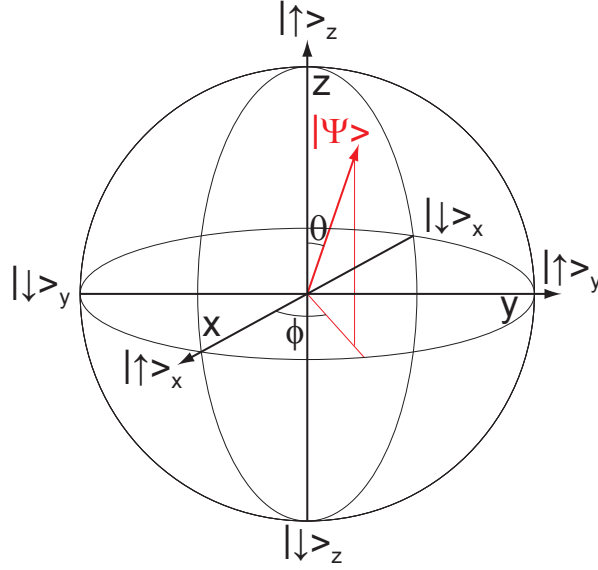


Figure 2.1: The Bloch sphere: Every qubit state can be represented as a point on the surface of the sphere and is defined by the spherical angles  $\theta$  and  $\phi$ .

### 2.1.1.1 Bell states

If we extend our considerations to a two qubit system we get a four dimensional Hilbert space. This Hilbert space is not separable if the two qubits are entangled<sup>1</sup> which means that the combined wave function  $|\Psi\rangle$  can not be described as a tensor product of the sub-states, hence

$$|\Psi\rangle \neq |\Psi\rangle_a \otimes |\Psi\rangle_b. \quad (2.9)$$

One important feature of these states is that the state  $|\Psi\rangle$  is a well defined quantum state in contrast to the single sub-systems  $|\Psi\rangle_a$  or  $|\Psi\rangle_b$ . We can not consider the maximally entangled sub-systems  $|\Psi\rangle_a$  or  $|\Psi\rangle_b$  separately. The outcome of a measurement on just one sub-state  $|\Psi\rangle_a$  is random for every measurement basis  $\mathcal{A}$ . On the other hand we know the outcome of the measurement on  $|\Psi\rangle_b$  in a definite basis  $\mathcal{B}$  with certainty, if we know the result of the measurement of  $|\Psi\rangle_a$  in the basis  $\mathcal{A}$ . For two spin-1/2 systems we can find a set of four separable eigenstates  $|\uparrow\rangle_z |\uparrow\rangle_z$ ,

<sup>1</sup>This can be realised in the spontaneous decay of a spin-0 particles as proposed by Bohm [5].

$|\uparrow\rangle_z |\downarrow\rangle_z$ ,  $|\downarrow\rangle_z |\uparrow\rangle_z$  and  $|\downarrow\rangle_z |\downarrow\rangle_z$  and define a new basis of four maximally entangled states, the so-called Bell states:

$$|\Psi^-\rangle = \sqrt{\frac{1}{2}} (|\uparrow\rangle_z |\downarrow\rangle_z - |\downarrow\rangle_z |\uparrow\rangle_z) \quad (2.10)$$

$$|\Psi^+\rangle = \sqrt{\frac{1}{2}} (|\uparrow\rangle_z |\downarrow\rangle_z + |\downarrow\rangle_z |\uparrow\rangle_z) \quad (2.11)$$

$$|\Phi^-\rangle = \sqrt{\frac{1}{2}} (|\uparrow\rangle_z |\uparrow\rangle_z - |\downarrow\rangle_z |\downarrow\rangle_z) \quad (2.12)$$

$$|\Phi^+\rangle = \sqrt{\frac{1}{2}} (|\uparrow\rangle_z |\uparrow\rangle_z + |\downarrow\rangle_z |\downarrow\rangle_z) \quad (2.13)$$

$|\Psi^-\rangle$  is the antisymmetric singlet state and the other three are symmetric triplet states. This means that exchanging the particles gives a global minus-sign on the state (anti-symmetric) or the state remains the same (symmetric).

We can write the states 2.10-2.13 in complementary bases  $\sigma_x$  and  $\sigma_y$ . If we consider, e.g.,  $|\Psi^+\rangle$  we can write the transformations

$$|\Psi^+\rangle = \sqrt{\frac{1}{2}} (|\downarrow\rangle_x |\downarrow\rangle_x + |\uparrow\rangle_x |\uparrow\rangle_x) \quad (2.14)$$

$$= \sqrt{\frac{1}{2}} (|\downarrow\rangle_y |\downarrow\rangle_y - |\uparrow\rangle_y |\uparrow\rangle_y). \quad (2.15)$$

In this way it is shown that an entangled state remains entangled when changing the measurement basis as it is not possible to find a basis in which the state is separable. This correlation of the two entangled systems is one of the key elements of quantum mechanics. The discussion about the physical reality behind the measurement results on entangled states led to the EPR paradoxon and the development of Bell's inequality.

## 2.2 Bell's inequality

### 2.2.1 Einstein-Podolski-Rosen paradox

Analysing the states<sup>2</sup> 2.10-2.13 one observes a characteristic property. If we measure only one qubit in a basis  $\mathcal{A}$ , the result is completely random, but if we measure

<sup>2</sup>Schrödinger called this state in 1935 *entangled* (*verschränkt*) [2].

both in the same basis the result of the first qubit determines the result of the second with certainty. The reason for this was discussed controversially from the beginning of quantum mechanics [3, 4] until the present. The Copenhagen interpretation stated that for a quantum mechanical system a physical property does not exist in a common sense until it is measured. The measurement process (the observation) provides the system with the property.

Einstein's objection against the interpretation that an observer has to be taken into account led to the publication of the article *Can quantum mechanical description of physical reality be considered complete?* [3] together with Podolski and Rosen. They proposed three claims that should be fulfilled by a physical theory:

1. Completeness: *every element of the physical reality must have a counterpart in the physical theory* [3].
2. Realism: *If, without in any way disturbing a system, we can predict with certainty (i.e. with probability equals to unity) the value of a physical quantity, then there exists an element of physical reality corresponding to this physical quantity* [3].
3. Locality: *The real factual situation of the system  $S_2$  is independent of what is done with the system  $S_1$ , which is spatially separated from the former* [24].

They proposed a Gedankenexperiment with two in space and momentum entangled particles. Separated in space one performs a momentum and position measurement, respectively. Measuring the position of particle 1 one can, according to quantum mechanics, predict with certainty the outcome of a position measurement of particle 2, hence this position is an element of physical reality. In the same way one can show that the momentum of particle 2 is an element of the physical reality as well, resulting in a strong contradiction with the Heisenberg uncertainty principle.

This was in contradiction to quantum mechanics and N. Bohr replied [4] that the definition of an element of reality has to be made with the experimental apparatus included. Hence it is not justified to speak of the simultaneous reality of complementary degrees of freedom. He rejected their conclusion of quantum mechanics being incomplete. There was no result in this discussion as it ended because of Einstein's

death. Einstein was a big authority in theoretical physics so people tried to justify his claims. They developed theories with hidden variables, i.e. variables attached on the particle that are not described by quantum mechanics, but are an object of physical reality. These local hidden variables (LHV) should completely determine the measurement results of the particles.

The momentum-space entanglement in EPR's Gedankenexperiment was mathematically difficult due to the infinite dimensions in the corresponding Hilbert space. Bohm developed a similar formulation using spin-1/2 particles in the spin singlet state  $|\Psi^-\rangle$  generated by the decay of a spin-0 system that were easier to deal with [5]. Based on these considerations Bell derived his inequality [6].

### 2.2.2 Bell's inequality

The question Bell considered is: Do theories with local-hidden variables make predictions different from those of quantum mechanics? Until 1964 there was no criterion to distinguish between local realism and quantum mechanics, but J.S. Bell pointed out [6] that theories, based on Einstein's local realism principle, must predict measurement outcomes in disagreement with the predictions of quantum mechanics and he derived an inequality using these observables that allows to distinguish the predictions of quantum mechanics from LHV theories.

For the derivation we assume a large number of spin-1/2 particles in a LHV-world<sup>3</sup> and a certain fraction of them has the following properties [22, 25]:

- If  $S_z$  is measured, we obtain a plus sign with certainty.
- If  $S_x$  is measured, we obtain a minus sign with certainty<sup>4</sup>.

---

<sup>3</sup>To distinguish particles in a LHV world and in a quantum mechanical world, states of the former are written as  $|\pm\rangle$  and quantum mechanical states are written as  $|\uparrow\downarrow\rangle$ .

<sup>4</sup>Proponents of alternative theories agree that we are not able to determine  $S_x$  and  $S_z$  simultaneously, but we do not assert to be able to measure them simultaneously. We just label our particles (i.e. hidden variables) with a definite value in more than one direction.

## 2 Theory

---

A particle that satisfies these requirements belongs to the state<sup>5</sup>  $|+z, -x\rangle$ . This is diametrically opposed to quantum mechanics but the source provides particles in the state  $|+z, -x\rangle$  and  $|+z, +x\rangle$  with equal probability. Performing an  $S_z$  and  $S_x$  measurement the predictions of quantum mechanics for  $|\uparrow\rangle_z$  are reproduced by the provided ensemble.

Now we assume we have two particles. The entire system is supposed to be in the singlet state, so in order to reproduce the predictions of quantum mechanics the two particles have to be in the following states:

$$\begin{array}{cc} \text{particle 1} & \text{particle 2} \\ | +z, -x \rangle & \leftrightarrow | -z, +x \rangle \end{array} \quad (2.16)$$

$$| +z, +x \rangle \leftrightarrow | -z, -x \rangle \quad (2.17)$$

$$| -z, +x \rangle \leftrightarrow | +z, -x \rangle \quad (2.18)$$

$$| -z, -x \rangle \leftrightarrow | +z, +x \rangle \quad (2.19)$$

and all states should be equally populated with 25% each. According to EPR's locality assumptions we can conclude:

If observer A, let's call her Alice, measures  $S_z$  on particle 1 of 2.16, her result is +1 with certainty. This is independent of the measurement of observer B, Bob, to ensure that the outcome of Alice's measurement does not depend on the basis Bob chooses to measure (locality condition).

We have no contradictions to the predictions of quantum mechanics so far, but, if we extend our model, it will lead to predictions different from the quantum mechanical ones.

We consider now three measurement bases defined by three unit vectors  $\hat{\mathbf{a}}$ ,  $\hat{\mathbf{b}}$ ,  $\hat{\mathbf{c}}$  that in general are not mutually perpendicular. If we now consider  $| -a, +b, +c \rangle$  as a particle in a defined state and perform measurements on it we get the results

- -1 along  $\hat{\mathbf{a}}$
- +1 along  $\hat{\mathbf{b}}$

---

<sup>5</sup>This is just one particle, but it has two variables that define its state. This is exactly what a local hidden variable theory would say.

Population	particle 1	particle 2
$N_1$	$ +a, +b, +c\rangle$	$ -a, -b, -c\rangle$
$N_2$	$ +a, +b, -c\rangle$	$ -a, -b, +c\rangle$
$N_3$	$ +a, -b, +c\rangle$	$ -a, +b, -c\rangle$
$N_4$	$ +a, -b, -c\rangle$	$ -a, +b, +c\rangle$
$N_5$	$ -a, +b, +c\rangle$	$ +a, -b, -c\rangle$
$N_6$	$ -a, +b, -c\rangle$	$ +a, -b, +c\rangle$
$N_7$	$ -a, -b, +c\rangle$	$ +a, +b, -c\rangle$
$N_8$	$ -a, -b, -c\rangle$	$ +a, +b, +c\rangle$

Table 2.1: All possible anticorrelated spin states with hidden variables and their populations  $N_i \in [0, 1]$ .

- +1 along  $\hat{\mathbf{c}}$

The particles still have to fulfil relations similar to eq. 2.16-2.19. In our case particle 2 has to show perfect anticorrelations of the measurement results [26] and has to be in the state  $|+a, -b, -c\rangle$ . With permutations we get the eight states in tab. 2.1 that are mutually exclusive and have the population  $N_i$ .

Alice now measures e.g.  $\mathbf{S}_1 \cdot \hat{\mathbf{a}}$  to be +1 on particle 1 and Bob the same for  $\mathbf{S}_2 \cdot \hat{\mathbf{b}}$  on particle 2, so the system must be either in the state 3 or 4 according to tab. 2.1. The population of every single state is non-negative and hence we must have

$$N_3 + N_4 \leq (N_2 + N_4) + (N_3 + N_7). \quad (2.20)$$

$\mathbb{P}(|+a, +b\rangle)$  is the probability that Alice measures  $\mathbf{S}_1 \cdot \hat{\mathbf{a}}$  the result +1 and Bob obtains the result +1 for measurements in the bases  $\mathbf{S}_2 \cdot \hat{\mathbf{b}}$ . Apparently we get

$$\mathbb{P}(|+a, +b\rangle) = \frac{(N_3 + N_4)}{\sum_{i=1}^8 N_i} \quad (2.21)$$

$$\mathbb{P}(|+a, +c\rangle) = \frac{(N_2 + N_4)}{\sum_{i=1}^8 N_i} \quad (2.22)$$

$$\mathbb{P}(|+c, +b\rangle) = \frac{(N_3 + N_7)}{\sum_{i=1}^8 N_i}. \quad (2.23)$$

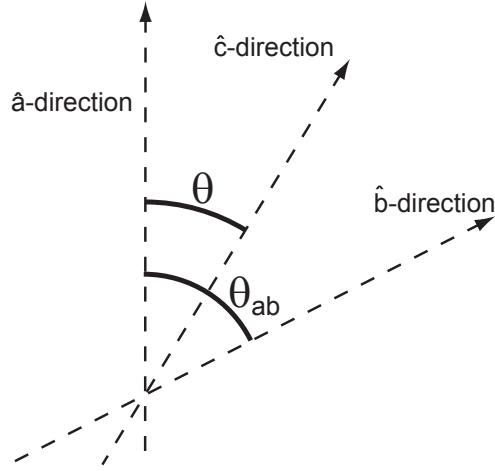


Figure 2.2: Definition of the angles between the measurement directions  $\hat{\mathbf{a}}$ ,  $\hat{\mathbf{b}}$  and  $\hat{\mathbf{c}}$ .

Rewriting eq. 2.20, we get the inequality

$$\mathbb{P}( |+_a, +_b \rangle ) \leq \mathbb{P}( |+_a, +_c \rangle ) + \mathbb{P}( |+_c, +_b \rangle ) \quad (2.24)$$

that should be fulfilled by every theory based on EPR's locality and realism principle. This inequality is one version of Bell's inequality that allows now to distinguish between EPR's locality and realism principle and quantum mechanics [22, 25].

### 2.2.3 Quantum mechanical predictions

We now want to calculate the terms in eq. 2.24 in the framework of quantum mechanics. In contrast to the above, we are not talking about fractions of particle pairs  $N_i / \sum_{i=1}^8 N_i$  with different properties, but have the whole ensemble in the singlet state

$$|\Psi^-\rangle = \sqrt{\frac{1}{2}} ( |\uparrow\rangle_z |\downarrow\rangle_z - |\downarrow\rangle_z |\uparrow\rangle_z ), \quad (2.25)$$

which shows anticorrelation in any measurement basis.

If Alice finds  $\mathbf{S}_1 \cdot \hat{\mathbf{a}}$  to be positive than Bob must get a negative sign when he measures  $\mathbf{S}_2 \cdot \hat{\mathbf{a}}$ . To evaluate the probability  $\mathbb{P}( |+ \rangle_a |+ \rangle_b )$  we set the quantisation axis  $\hat{\mathbf{b}}$  to

enclose an angle  $\theta_{ab}$  with respect to  $\hat{\mathbf{a}}$  as shown in fig. 2.2. Bob's particle has to be in an eigenstate of  $\mathbf{S}_2 \cdot \hat{\mathbf{a}}$  with negative eigenvalue, so the probability that the  $\mathbf{S}_2 \cdot \hat{\mathbf{b}}$  measurement yields a positive value is  $\sin^2 \frac{\theta_{ab}}{2}$  and we get

$$\mathbb{P}(|\uparrow\rangle_a, |\uparrow\rangle_b) = \frac{1}{2} \sin^2 \frac{\theta_{ab}}{2}, \quad (2.26)$$

where the factor 1/2 comes from the fact that Alice's measurement result +1 has the probability 1/2. In the same way we get the values for  $\mathbb{P}(|\uparrow\rangle_a, |\uparrow\rangle_c)$  and  $\mathbb{P}(|\uparrow\rangle_c, |\uparrow\rangle_b)$  and putting these terms into Bell's inequality we obtain

$$\sin^2 \frac{\theta_{ab}}{2} \leq \sin^2 \frac{\theta_{ac}}{2} + \sin^2 \frac{\theta_{cb}}{2}. \quad (2.27)$$

If we choose  $\hat{\mathbf{a}}$ ,  $\hat{\mathbf{b}}$  and  $\hat{\mathbf{c}}$  to lie in a plane and  $\hat{\mathbf{c}}$  bisect the angle defined by  $\hat{\mathbf{a}}$  and  $\hat{\mathbf{b}}$ :

$$\theta_{ac} = \theta_{cb} = \theta \quad (2.28)$$

$$\theta_{ab} = 2\theta, \quad (2.29)$$

we get

$$\sin^2 \theta \leq 2 \sin^2 \frac{\theta}{2}. \quad (2.30)$$

In this way eq. 2.27 is violated for

$$0 < \theta < \frac{\pi}{2} \quad (2.31)$$

and thus the quantum mechanical predictions are not compatible with Bell's inequality as we get, for example, for  $\theta = \frac{\pi}{4}$

$$0.500 \leq 0.292. \quad (2.32)$$

This is obviously a wrong statement. With this inequality we now have a way to decide experimentally if physical reality can be described by means of local realism or not.

### 2.2.4 Loopholes

The violation of 2.27 was observed in many experiments [9, 10, 11, 12, 14]. However, a violation of this inequality does not necessarily rule out all LHV theories. What one has to take care of are two loopholes that arise in all of these experiments:

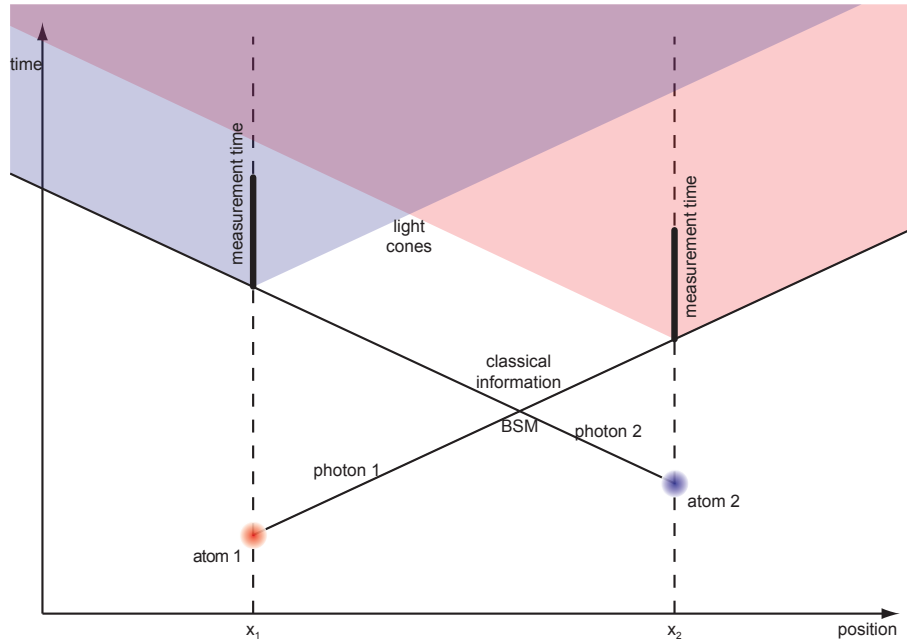


Figure 2.3: Space-time diagram of the experimental process in a suggested loophole free Bell test: Each atom emits a photon which polarisation is entangled with the internal atomic state. At the junction of the two photons a Bell state measurement (BSM) is performed. If the two photons are in the state  $|\Psi^-\rangle$ , classical information is sent back and the state of the atoms is measured whereby the entire procedure to measure the state of the atom must be completed within the time  $\tau_{measurement} < c \cdot (x_1 - x_2)$ .

1. Detection loophole: If only a certain subset of the entangled particles is detected, one has to assume that they are a representative sample of the entire ensemble. In order not to have to rely on this *fair sampling* assumption a large fraction of the entangled particles must be detected.
2. Locality loophole: One fundamental request of Einstein was the independence of the measurement processes, when the two particles are far separated. If one assumes that no interaction faster than the speed of light is possible this requires that the two experimental apparatus' have to be space-like separated with respect to their measurement time (see fig. 2.3).

The experiments to observe a violation of Bell's inequality used either entangled photons [12] or entangled trapped ions [14]. The detection efficiency of ions is very high but the distance between the two ions was too small to close the locality loophole. In the former experiment entangled photons were used under strict locality conditions but the detection efficiency was very low.

## 2.2.5 Applications of entanglement

The concept of entanglement is not just interesting for the fundamental concepts of nature but also has some practical implications. It is the basic ingredient for almost all quantum information applications [18]. This chapter will give a short introduction into the main applications namely quantum teleportation and entanglement swapping.

### 2.2.5.1 Quantum teleportation

One problem in quantum information experiments is the transfer of an unknown quantum state to a remote location. Measuring the unknown state and sending the result to Bob is not possible as the measurement will destroy the quantum state and the information necessary for its reconstruction is lost<sup>6</sup>. With the quantum

---

<sup>6</sup>After the measurement the particle is in an eigenstate of the Hamiltonian applied, not in the original state.

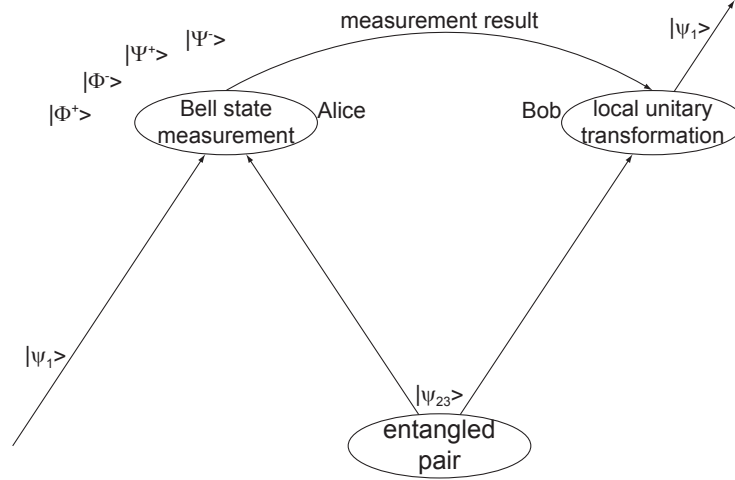


Figure 2.4: Principle of quantum teleportation: The initial state  $|\psi_1\rangle$  expands the Hilbert space of the entangled pair. The result of the Bell state measurement of Alice is reported classically to Bob and with a local unitary transformation  $|\Psi_1\rangle$  is transferred to particle 3.

teleportation protocol [27] we can overcome this problem and we can transfer the unknown state  $|\Psi\rangle_1 = (\alpha|\uparrow\rangle + \beta|\downarrow\rangle)_1$  from Alice to Bob without sending the particle itself. In this protocol Alice and Bob initially share a pair of entangled particles in the state  $|\Psi^-\rangle$ .

Assuming the initial particle to be in the state  $|\Psi\rangle_1$  and labelling the entangled pair by 2 and 3, we can write the combined three particle state in the following way:

$$|\Psi\rangle = |\Psi\rangle_1 \otimes |\Psi\rangle_{23} = (\alpha|\uparrow\rangle + \beta|\downarrow\rangle)_1 \otimes (|\uparrow\rangle|\downarrow\rangle - |\downarrow\rangle|\uparrow\rangle)_{23} / \sqrt{2} \quad (2.33)$$

reformulating we get

$$\begin{aligned} |\Psi\rangle = & \frac{1}{2} [ |\Psi^-\rangle_{12} (-\alpha|\uparrow\rangle_3 - \beta|\downarrow\rangle_3) \\ & + |\Psi^+\rangle_{12} (-\alpha|\uparrow\rangle_3 + \beta|\downarrow\rangle_3) \\ & + |\Phi^-\rangle_{12} (+\alpha|\downarrow\rangle_3 + \beta|\uparrow\rangle_3) \\ & + |\Phi^+\rangle_{12} (+\alpha|\downarrow\rangle_3 - \beta|\uparrow\rangle_3) ] \end{aligned} \quad (2.34)$$

If now Alice performs a measurement of the initial particle 1 and particle 2 from

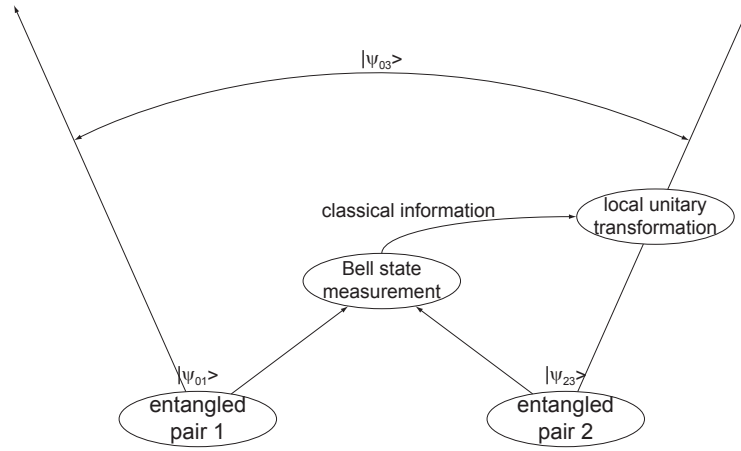


Figure 2.5: Principle of entanglement swapping: Two entangled atom-photon pairs are generated. The photons 1 and 2 are subjected to a Bell state measurement. This measurement projects the two atoms 0 and 3 onto an entangled state  $|\Psi_{03}\rangle$ .

the entangled state in the Bell basis, particle 3 is left in one of the four states of eq. 2.34. E.g. if Alice measures  $|\Psi^-\rangle_{12}$  particle 3 is in the state  $|\Psi\rangle = \alpha|\uparrow\rangle + \beta|\downarrow\rangle$  (neglecting a global phase). For the other three possible outcomes Bob has to perform one of three unitary transformations  $\mathcal{U}$  necessary to transform the state of particle 3 into the original state of particle 1 (see fig. 2.4). For this, Alice has to send the measured result (2 bit of classical information) to Bob, but not more.

The unitary transformations are the following. If Alice measures  $|\Psi^+\rangle_{12}$  Bob has to flip the sign of the particle, for  $|\Phi^-\rangle_{12}$  he has to flip the spin and for  $|\Phi^+\rangle_{12}$  both transformations have to be applied. In this way the initial state of particle 1 is reconstructed on the remote particle 3.

### 2.2.5.2 Entanglement swapping

We now take two entangled pairs with which we can expand the teleportation mechanism to create two entangled particles that never interacted before [17]. The difference to the former case is that particle 1 itself now is a part of an entangled

pair in the state  $|\Psi^-\rangle_{01}$  as shown in fig. 2.5. The entire state can be written as

$$\begin{aligned} |\Psi\rangle_{0123} &= |\Psi^-\rangle_{01} \otimes |\Psi^-\rangle_{23} \\ &= \frac{1}{2} (|\Psi^+\rangle_{03} \otimes |\Psi^+\rangle_{12} - |\Psi^-\rangle_{03} \otimes |\Psi^-\rangle_{12} \\ &\quad - |\Phi^+\rangle_{03} \otimes |\Phi^+\rangle_{12} + |\Phi^-\rangle_{03} \otimes |\Phi^-\rangle_{12}) \end{aligned} \quad (2.35)$$

Then the particles 0 and 3 are in one of the four Bell states 2.16-2.19, if Alice performs a Bell state measurement on the particles 1 and 2. Applying the unitary transformation  $\mathcal{U}$  on one side conditioned upon measurement outcome the initial state  $|\Psi\rangle_{01}$  gets teleported onto the state  $|\Psi\rangle_{03}$  as in the preceding chapter.

The entanglement swapping protocol is very important for applications in quantum communication and quantum computing, namely the setup of a quantum network and quantum repeater [28].

## 2.3 Quantum mechanical basics of $^{87}\text{Rb}$

We use  $^{87}\text{Rb}$  in our experiment. This element is an alkaline metal with only one valence electron ( $e^-$ ). The structure of the atomic transitions is well suited for our experiment as it approximates a  $\Lambda$  decay scheme [13, 15, 16]. It can be trapped in a magneto-optical trap and in an optical dipole trap and hence we can get a single  $^{87}\text{Rb}$  atom for the experiment.

### 2.3.1 Fine structure

The transitions  $|5^2S_{1/2}\rangle \rightarrow |5^2P_{1/2}\rangle$  and  $|5^2S_{1/2}\rangle \rightarrow |5^2P_{3/2}\rangle$  from the ground to the first excited state form a fine-structure doublet that is not degenerate. It occurs as a result of the coupling between the orbital angular momentum  $\mathcal{L}$  and the spin angular momentum  $\mathcal{S}$  of the valence electron. In order to obtain the new angular momentum eigenstates (see in Eq. A.5), we can define a new operator

$$\mathcal{J} = \mathcal{L} \oplus \mathcal{S} \quad (2.36)$$

and the corresponding eigenvalues lie in the range

$$|L - S| \leq J \leq L + S. \quad (2.37)$$

Applying  $\mathcal{J}$  on a state  $|\Psi\rangle$  of  $^{87}\text{Rb}$  we get

$$\mathcal{J}^2 |\Psi\rangle = J(J+1)\hbar^2 |\Psi\rangle \quad (2.38)$$

$$\mathcal{J}_z |\Psi\rangle = m_J \hbar |\Psi\rangle. \quad (2.39)$$

The energy of every particular level is shifted according to the value of  $J$ . In our case of  $^{87}\text{Rb}$  in the ground state  $|5^2S_{1/2}\rangle$  the valence  $e^-$  has the principal quantum number  $n = 5$ . The spin of the  $e^-$  is  $1/2$  and hence in the ground state  $L = 0$  leads to  $J = 1/2$ . In the first excited state, the spin-orbit coupling causes a split of the energies ( $\approx 0.0295\text{eV}$  or  $\approx 14.7\text{nm}$ ) between the transition  $|5^2S_{1/2}\rangle \rightarrow |5^2P_{1/2}\rangle$  and  $|5^2S_{1/2}\rangle \rightarrow |5^2P_{3/2}\rangle$ , where  $L = 1$  and hence we have a fine structure with two levels,  $|5^2P_{1/2}\rangle$  and  $|5^2P_{3/2}\rangle$ . They are easily distinguishable in ordinary absorption spectroscopy measurements and belong to the D<sub>1</sub>- and D<sub>2</sub>-line, respectively. This nomenclature is based on the transitions of sodium where they were first observed experimentally and led to the postulation of an electron spin in the year 1925 [29].

### 2.3.2 Hyperfine structure

The total electron angular momentum  $\mathcal{J}$  also couples to the total nuclear angular momentum  $\mathcal{I}$  which is  $I = 3/2$  for  $^{87}\text{Rb}$ . We get the total angular momentum of the atom by

$$\mathcal{F} = \mathcal{J} \oplus \mathcal{I} \quad (2.40)$$

and as above

$$|J - I| \leq F \leq J + I. \quad (2.41)$$

For the  $^{87}\text{Rb}$  ground state  $|5^2S_{1/2}\rangle$  and the excited state  $|5^2P_{1/2}\rangle$ ,  $F$  can take values  $F = 1$  or  $F = 2$  and for the excited state,  $|5^2P_{3/2}\rangle$ ,  $F$  can take all the values  $F = 0, 1, 2, 3$ .

The energy shifts of these levels are in the GHz range, hence much smaller than the fine structure. The Hamiltonian describing the hyperfine structure for each of the D-line components is [30]

$$\mathcal{H}_{hfs} = A_{hfs} \mathcal{I} \cdot \mathcal{J} + B_{hfs} \frac{3(\mathcal{I} \cdot \mathcal{J})^2 + \frac{3}{2}(\mathcal{I} \cdot \mathcal{J}) - I(I+1)J(J+1)}{2I(2I-1)J(2J-1)}. \quad (2.42)$$

Magnetic Dipole constant, $5^2S_{1/2}$	$A_{5^2S_{1/2}}$	$h \cdot 3.41734130545215(5)$ GHz	[31]
Magnetic Dipole constant, $5^2P_{1/2}$	$A_{5^2P_{1/2}}$	$h \cdot 408.328(15)$ MHz	[32]
Magnetic Dipole constant, $5^2P_{3/2}$	$A_{5^2P_{3/2}}$	$h \cdot 84.7185(20)$ MHz	[33]
Electric quadrupole constant, $5^2P_{3/2}$	$B_{5^2P_{3/2}}$	$h \cdot 12.4965(37)$ MHz	[33]

Table 2.2:  $^{87}\text{Rb}$  D-transition hyperfine structure constants

The energy shift between the single levels denotes as

$$\Delta E_{hfs} = \frac{1}{2}A_{hfs}K + B_{hfs}\frac{\frac{3}{2}K(K+1) - 2I(I+1)J(J+1)}{2I(2I-1)2J(2J-1)} \quad (2.43)$$

with  $K = F(F+1) - I(I+1) - J(J+1)$ .  $A_{hfs}$  and  $B_{hfs}$  are the magnetic dipole and the electric quadrupole constants, respectively, and are listed in Table 2.2. These values arise from high accuracy measurements described in [31, 32, 33].

### 2.3.3 Zeeman-effect

For each hyperfine level with quantum number  $F$  (see Eq. A.13), there exist  $2F+1$  magnetic sublevels that are degenerate. This degeneracy is broken by applying an external magnetic field, and the interaction is described by the Hamiltonian

$$\begin{aligned} \mathcal{H}_B &= \frac{\mu_B}{\hbar} (g_S \mathcal{S} + g_L \mathcal{L} + g_I \mathcal{I}) \\ &= \frac{\mu_B}{\hbar} (g_S \mathcal{S}_z + g_L \mathcal{L}_z + g_I \mathcal{I}_z). \end{aligned} \quad (2.44)$$

In the case of 2.44 we took the  $\vec{B}$ -field to be along the z-direction. Whenever the energy shift caused by the magnetic field is small compared to the hyperfine splitting, 2.44 reduces to

$$\mathcal{H}_B = \mu_B g_F \mathcal{F}_z B_z \quad (2.45)$$

with the Landé  $g_F$ -factor quoted in fig. 2.6.

## 2.4 Interaction of light with a single atom

Until now we considered only an isolated free atom. Next we extend our considerations to an atom in an electro-magnetic field. Since light fields affect the internal

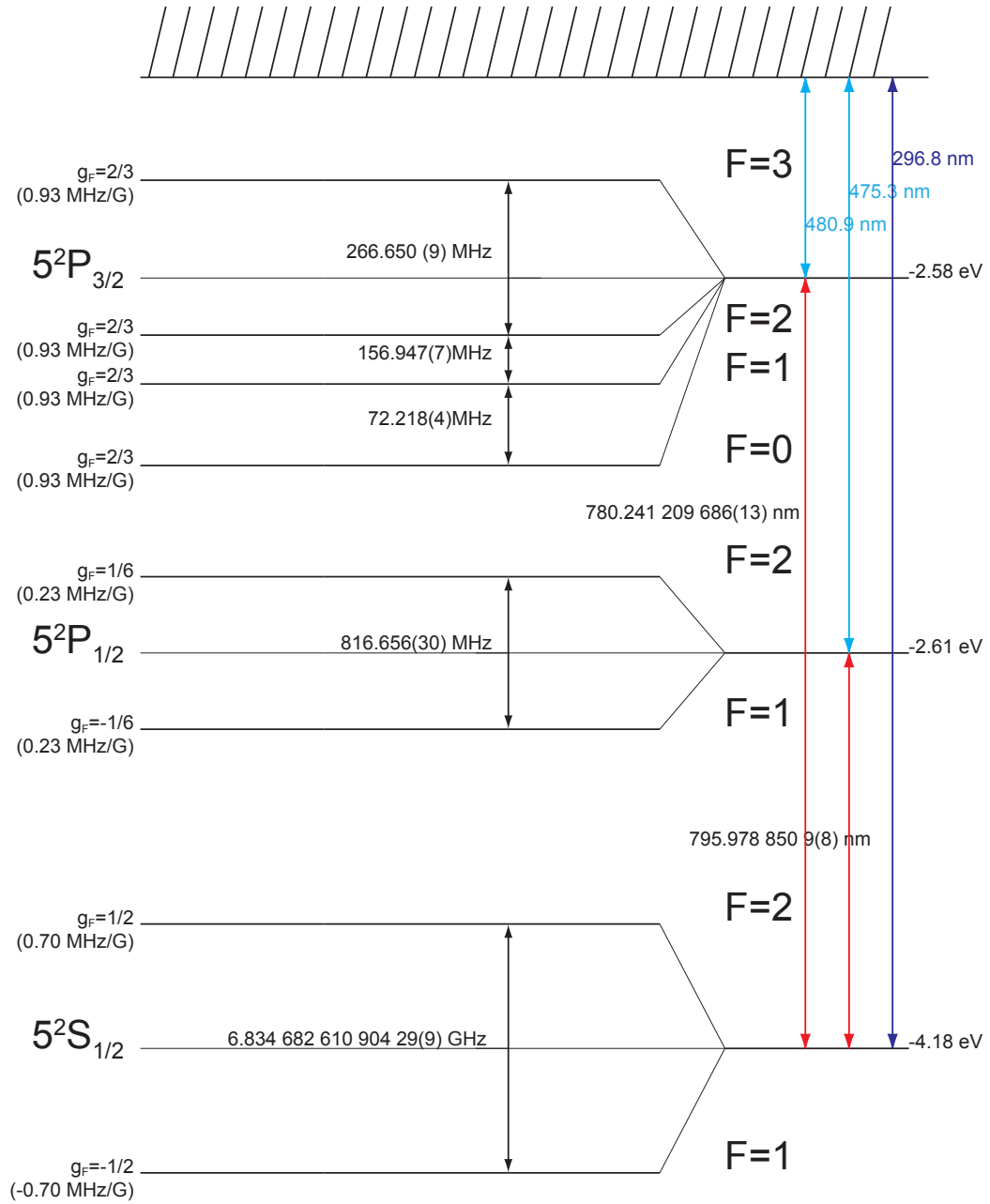


Figure 2.6: Level scheme of  $^{87}\text{Rb}$  (not to scale)

states of the atom I will sketch theoretical aspects of light-matter interaction which are relevant for the understanding of various experimental techniques [21, 34, 35].

### 2.4.1 The interaction Hamiltonian

The time-dependent Schrödinger equation for an atom interacting with an electromagnetic field is

$$\mathcal{H}\Psi(\mathbf{r}, t) = i\hbar \frac{\partial \Psi(\mathbf{r}, t)}{\partial t}. \quad (2.46)$$

The Hamiltonian  $\mathcal{H} = \mathcal{H}_0 + \mathcal{H}'$  is composed of the Hamiltonian of the free atom  $\mathcal{H}_0$  and the Hamiltonian  $\mathcal{H}'$  which describes the interaction with the electro-magnetic field. For  $\mathcal{H}_0$  we get a complete set of orthogonal spatial eigenfunctions  $\phi_k(\mathbf{r})$  with the eigenvalues  $\hbar\omega_k$ . Therefore one can decompose any  $\Psi(\mathbf{r}, t)$  in the basis of the  $\phi_k(\mathbf{r})$

$$\Psi(\mathbf{r}, t) = \sum_k c_k(t) \phi_k(\mathbf{r}) e^{-i\omega_k t}. \quad (2.47)$$

Inserting this into Eq. 2.46 we get

$$i\hbar \frac{dc_j}{dt} = \sum_k c_k(t) \mathcal{H}'_{jk} e^{i\omega_{jk} t} \quad (2.48)$$

with  $\mathcal{H}'_{jk} = \langle \phi_j | \mathcal{H}' | \phi_k \rangle$  and  $\omega_{jk} = \omega_j - \omega_k$ . As the classical electric field  $\mathcal{E}(\mathbf{r}, t) = \mathbf{E}_0 \cos(kz - \omega_l t)$  interacts with the electric dipole  $\mathbf{d}$  of the atom the Hamiltonian  $\mathcal{H}'$  can be written as

$$\mathcal{H}' = \mathcal{E}(\mathbf{r}, t) \cdot \mathbf{d} = \mathbf{E}_0 \cdot \mathbf{d} \cos(kz - \omega_l t) \quad (2.49)$$

assuming the volume of interaction of the electric field with the atom is smaller than the wavelength of the light (electric dipole approximation). Now we get

$$\begin{aligned} \mathcal{H}'_{jk} &= \langle \phi_j | \mathbf{E}_0 \cdot \mathbf{d} \cos(kz - \omega_l t) | \phi_k \rangle \\ &= \langle \phi_j | \mathbf{E}_0 \cdot \mathbf{d} | \phi_k \rangle \cos(kz - \omega_l t) \\ &= \hbar \Omega_{jk} \cos(kz - \omega_l t) \end{aligned}$$

where we defined the Rabi-frequency as  $\Omega_{jk} = \frac{1}{\hbar} \langle \phi_j | \mathbf{E}_0 \cdot \mathbf{d} | \phi_k \rangle$ . These Rabi-frequencies describe the coupling strength between the atom and the electro-magnetic field depending on the transition dipole moment  $\langle \phi_j | \mathbf{d} | \phi_k \rangle$ .

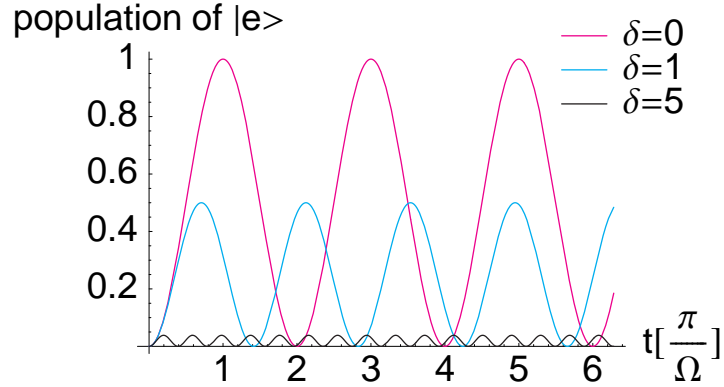


Figure 2.7: Rabi-oscillations of a two-level system without spontaneous decay. For increasing detuning  $\delta$  the amplitude of the oscillations decreases and the frequency  $\Omega'$  increases.

### 2.4.2 Rabi oscillations

If we consider a two level atom with the ground state  $|g\rangle$  and the excited state  $|e\rangle$  the state of the atom can be written as

$$|\Psi(t)\rangle = c_g(t) |g\rangle + c_e(t) |e\rangle \quad (2.50)$$

with  $|c_g|^2 + |c_e|^2 = 1$ . We want to drive the system to the excited state with an electro-magnetic wave  $\mathcal{E}(\mathbf{r}, t) = \mathbf{E}_0 \cos(kz - \omega_l t)$ . The electro-magnetic field has a detuning  $\delta = \omega_l - \omega_{ge}$  to the atomic transition frequency. Inserting this into eq. 2.48 and neglecting terms oscillating with  $e^{i(\omega_l + \omega_{ge})}$  compared to oscillation terms  $e^{i(\omega_l - \omega_{ge})}$  we get the population probabilities<sup>7</sup>

$$c_g(t) = \left( \cos \frac{\Omega' t}{2} - i \frac{\delta}{\Omega'} \sin \frac{\Omega' t}{2} \right) e^{\frac{i\delta t}{2}} \quad (2.51)$$

$$c_e(t) = -i \frac{\Omega}{\Omega'} \sin \frac{\Omega' t}{2} e^{-\frac{i\delta t}{2}} \quad (2.52)$$

with  $\Omega' = \sqrt{\Omega^2 + \delta^2}$ . This frequency is called Rabi frequency. On resonance, i.e.  $\delta = 0$ , the Rabi frequency is equal to the frequency with which the population

<sup>7</sup>This approximation is called *rotating wave approximation* (RWA) [21].

probabilities  $|c_g|^2$  and  $|c_e|^2$  oscillate (see fig. 2.7).

If we apply a light pulse of length  $T_\pi = \frac{\pi}{\Omega}$  for  $\delta = 0$ , starting in the ground state  $|g\rangle$  the probability that the atom is in the excited state  $|e\rangle$  is unity. These pulses are called  $\pi$ -pulses.

### 2.4.3 Optical Bloch equations

So far we did not consider spontaneous decay of the atom from the excited state  $|e\rangle$ . To describe this effect we have to introduce the density operator [21]

$$\rho = |\Psi\rangle\langle\Psi|, \quad (2.53)$$

that is Hermitian. All information about a system in a pure state is stored in the wave function  $|\Psi\rangle$ . We can determine the expectation values of the operator  $\mathcal{A}$  by

$$\langle\mathcal{A}\rangle = \langle\Psi|\mathcal{A}|\Psi\rangle \quad (2.54)$$

If we expand the wavefunction in a basis set  $\{|\phi_n\rangle\}$  we can write  $|\Psi\rangle$  as

$$|\Psi\rangle = \sum_{i=1}^n c_i |\phi_i\rangle. \quad (2.55)$$

In this way the matrix elements of  $\rho$  become

$$\rho_{ij} = \langle\phi_i|\rho|\phi_j\rangle = \langle\phi_i|\Psi\rangle\langle\Psi|\phi_j\rangle = c_i c_j^* \quad (2.56)$$

and the normalisation of the wavefunction yields  $\text{Tr}(\rho) = \langle\Psi|\Psi\rangle = 1$ .

The diagonal matrix elements are the probabilities  $|c_j|^2 \in [0, 1]$  to be in the state  $|\phi_i\rangle$ , whereas the off-diagonal elements  $c_i c_j^*$  are called coherences depending on the phase difference between  $c_i$  and  $c_j$ .

In this way we can rewrite eq. 2.54

$$\langle\mathcal{A}\rangle = \left\langle \sum_i c_i \phi_i \left| \mathcal{A} \right| \sum_j c_j \phi_j \right\rangle = \text{Tr}(\rho\mathcal{A}) \quad (2.57)$$

and for the pure state we get

$$\rho = \begin{pmatrix} c_e c_e^* & c_e c_g^* \\ c_g c_e^* & c_g c_g^* \end{pmatrix}. \quad (2.58)$$

$\rho$  contains  $n^2$  independent parameters even as  $\rho$  is Hermitian.

If we now consider a statistical mixture of several states  $\{|\Psi_n\rangle\}$  we can not describe the system with a single, pure wavefunction. The density operator hence reads

$$\rho = \sum_i p_i |\Psi_i\rangle \langle \Psi_i|, \quad (2.59)$$

where  $p_i$  is the statistical probability that the system is in the state  $|\Psi_i\rangle$ .

The time evolution of  $\rho$  has to satisfy the Schrödinger equation 2.46

$$i\hbar \frac{\partial \rho}{\partial t} = \sum_i p_i (\mathcal{H} |\Psi_i\rangle \langle \Psi_i| - |\Psi_i\rangle \langle \Psi_i| \mathcal{H}) \quad (2.60)$$

and hence we get for the time evolution of the density matrix:

$$i\hbar \frac{d\rho}{dt} = [\mathcal{H}, \rho]. \quad (2.61)$$

Now we can use the density operator to describe spontaneous decay. The spontaneous decay from the excited state leads to additional loss from  $|e\rangle$  to  $|g\rangle$  in addition to the coherent dynamic and the time evolution of the excited states becomes

$$\frac{d\rho_{ee}}{dt} = -\gamma\rho_{ee}. \quad (2.62)$$

The set of differential equations we obtain for our case of a two level atom in the rotating frame, using RWA,

$$\begin{aligned} \frac{d\rho_{gg}}{dt} &= \gamma\rho_{ee} + \frac{i}{2}(\Omega^* \tilde{\rho}_{eg} - \Omega \tilde{\rho}_{ge}) \\ \frac{d\rho_{ee}}{dt} &= -\gamma\rho_{ee} + \frac{i}{2}(\Omega \tilde{\rho}_{ge} - \Omega^* \tilde{\rho}_{eg}) \\ \frac{d\tilde{\rho}_{ge}}{dt} &= -\left(\frac{\gamma}{2} + i\delta\right) \tilde{\rho}_{ge} + \frac{i\Omega^*}{2}(\rho_{ee} - \rho_{gg}) \\ \frac{d\tilde{\rho}_{eg}}{dt} &= -\left(\frac{\gamma}{2} - i\delta\right) \tilde{\rho}_{eg} + \frac{i\Omega}{2}(\rho_{gg} - \rho_{ee}) \end{aligned} \quad (2.63)$$

with  $\tilde{\rho}_{ge} = \rho_{ge} e^{i\delta t}$ . These equations are called the optical Bloch equations (OBE).

### 2.4.3.1 Steady-state solutions of the Optical Bloch equations

We can use some relationships of the four differential equations to come to a steady state solution of eq. 2.63. First of all we have  $\rho_{gg} + \rho_{ee} = 1$  because of population conservation and  $\frac{d\rho_{gg}}{dt} = -\frac{d\rho_{ee}}{dt}$ . Using the fact  $\rho_{ge} = \rho_{eg}^*$  and defining the population difference  $w = \rho_{gg} - \rho_{ee}$  we see that

$$\frac{d\tilde{\rho}_{eg}}{dt} = -\left(\frac{\gamma}{2} - i\delta\right)\tilde{\rho}_{eg} + \frac{i\Omega w}{2} \quad (2.64)$$

$$\frac{dw}{dt} = -\gamma w - i(\Omega\tilde{\rho}_{eg}^* - \Omega^*\tilde{\rho}_{eg}) + \gamma \quad (2.65)$$

which are different from the equations 2.51 and 2.52 not including spontaneous decay as shown in fig. 2.7.

First of all we want to get the steady-state solution so we set all the time derivatives to zero

$$\frac{d\tilde{\rho}_{eg}}{dt} = 0 = \frac{dw}{dt} \quad (2.66)$$

and we get

$$w = \frac{1}{1+s} \quad (2.67)$$

$$\tilde{\rho}_{eg} = \frac{i\Omega}{2\left(\frac{\gamma}{2} - i\delta\right)(1+s)}. \quad (2.68)$$

The saturation parameter  $s$  is given by

$$s = \frac{|\Omega|^2}{2\left|\left(\frac{\gamma}{2} - i\delta\right)\right|^2} = \frac{|\Omega|^2/2}{\delta^2 + \gamma^2/4} \quad (2.69)$$

Introducing an on-resonance ( $\delta = 0$ ) saturation parameter

$$s_0 = \frac{2|\Omega|^2}{\gamma^2} = \frac{I}{I_s} \quad (2.70)$$

the last equation becomes

$$s = \frac{s_0}{1 + (2\delta/\gamma)^2} \quad (2.71)$$

with the saturation intensity given by

$$I_s = \frac{2\pi^2\hbar c}{3\lambda^3\tau}, \quad (2.72)$$

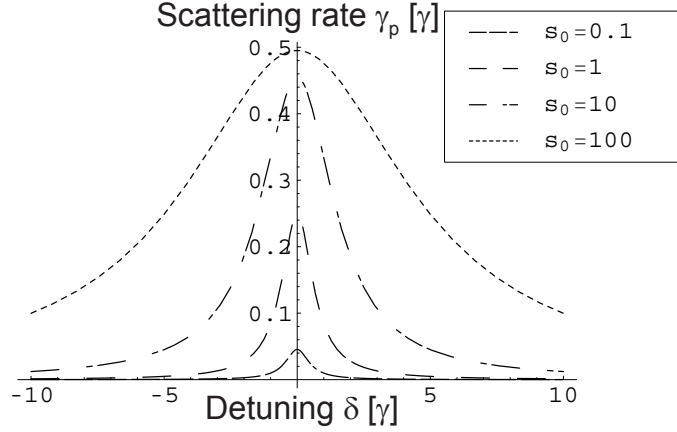


Figure 2.8: Steady state population of  $|e\rangle$  depending on the detuning  $\delta$  for various saturation parameters.

where  $\tau$  is the lifetime of the excited state. In this way one can rewrite the population of the excited state for  $t \rightarrow \infty$

$$\rho_{ee}^{\infty} = \frac{1}{2}(1 - w) = \frac{s}{2(1 + s)} = \frac{s_0}{1 + s_0 + (2\delta/\gamma)^2} \quad (2.73)$$

We can distinguish between the two cases,  $s \gg 1$  and  $s \ll 1$ . For low intensities mainly the ground state is populated, as  $\lim_{s \rightarrow 0} \rho_{ee} = 0$ . Increasing the intensity of the driving field i.e. the laser power, the excited state population  $\rho_{ee}$  saturates to  $1/2$ .

We can calculate the scattering rate  $\Gamma$ , the number of photons scattered by the atom and re-emitted isotropically during the decay back to the ground state, when the absorption and decay rate are equal.

$$\Gamma = \gamma \rho_{ee}^{\infty} = \frac{s_0 \gamma / 2}{1 + s_0 + (2\delta/\gamma)^2} = \frac{s_0}{1 + s_0} \frac{\gamma / 2}{1 + (2\delta/\gamma')^2} \quad (2.74)$$

with the power-broadened line width  $\gamma' = \sqrt{1 + s_0} \gamma$  of the transition.

On resonance the maximum scattering rate is  $\Gamma = \frac{\gamma}{2}$ . This occurs as on resonance half of the population is in the excited state in contrast to off-resonant excitation

$|\delta| > 0$ . With higher intensities  $s_0$  the linewidth of the absorption line is broadened due to power saturation (see fig. 2.8).

## 2.5 Trapping of a single atom

To realise our experiment with a single atom, a technique for single atom trapping is required. This is done in two steps. The first one is to trap a cloud of atoms ( $\approx 20000$ , see fig. 4.14) inside a magneto-optical trap. This provides us with a reservoir of cold atoms from where atoms can be loaded into an optical dipole trap (ODT) formed by a far red-detuned laser beam focused to  $1 \mu m$ . For such tight beam focus a *blockade* mechanism [36] prevents loading of more than one atom into the trap.

### 2.5.1 Magneto-optical trap

The magneto-optical trap is widely used for the trapping of neutral atoms. It employs both optical and magnetic fields and was first demonstrated in 1987 [37]. The trap is operated with an inhomogeneous magnetic field and exploits the Doppler shift for cooling and the Zeeman splitting for trapping.

#### 2.5.1.1 Trapping mechanism

I will explain the process of trapping in a magneto-optical trap on a simplified model of an atom. In this case the atom has only one magnetic sublevel in the ground state and three sublevels in the excited state. The magnetic field is a quadrupole field with a zero point and a linearly increasing field in its direct vicinity. The sublevels of the excited state split due to the Zeeman effect (see Eq. 2.44) and the transition frequencies are changed by  $\omega_Z = \mu' B / \hbar$  with  $\mu' = (g_e m_e - g_g m_g)$  the effective magnetic moment of the used transition (see fig. 2.6). For the two counterpropagating circularly polarised laser beams of equal intensity, detuned by  $\delta$  below resonance, the absorption rate of the atoms changes as the appropriate levels get shifted towards resonance or become more off-resonant. Thus an atom at rest has an equal radiation pressure from both sides only in the zero point of the magnetic

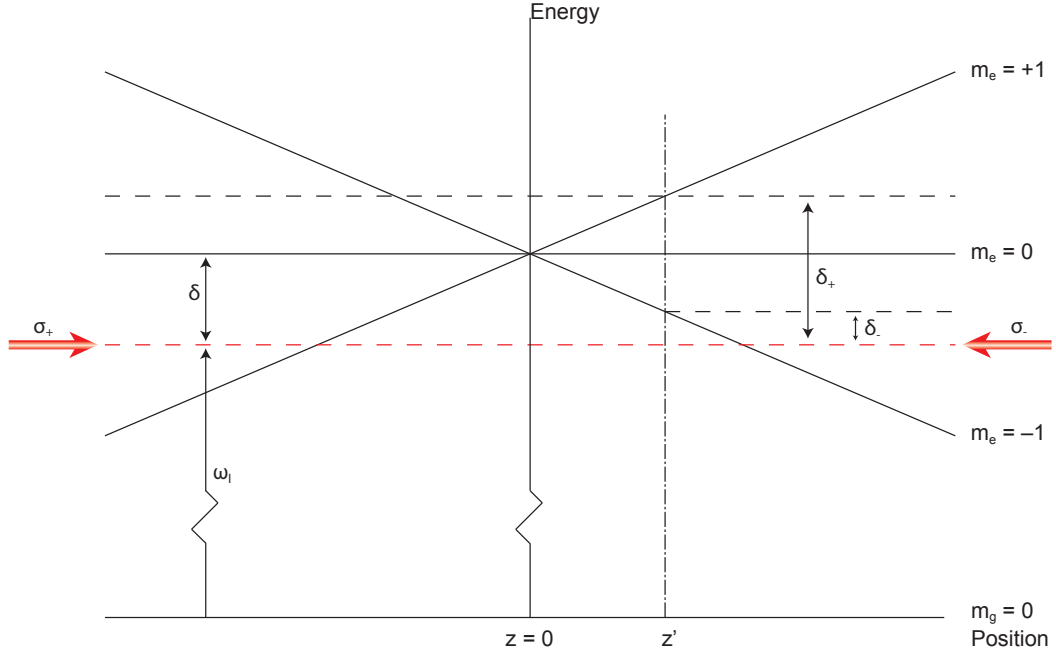


Figure 2.9: Schematic arrangement for a magneto-optical trap [21]

field. This leads to an confinement at the origin. The second effect is the Doppler shift. When the atom is moving towards the incident beam it is closer to resonance. In this way, it absorbs more light coming from this direction and is slowed down. This leads to overall cooling of the atom velocity.

In the terms of fig. 2.9 and 2.10, an atom moving to the right at a position  $z > 0$  absorbs with higher probability light from the  $\sigma_-$  beam. This way, the atom is decelerated, since a photon is absorbed from the right side, but the re-emission is isotropically. Hence the atoms experience a force back to the origin. The same happens on the other side when  $z < 0$  with the signs changed.

The force experienced by the atom can be written as

$$\vec{F}_{\pm} = \pm \frac{\hbar \vec{k} \gamma}{2} \frac{s_0}{1 + s_0 + (\delta_{\pm}/\gamma)^2} \quad (2.75)$$

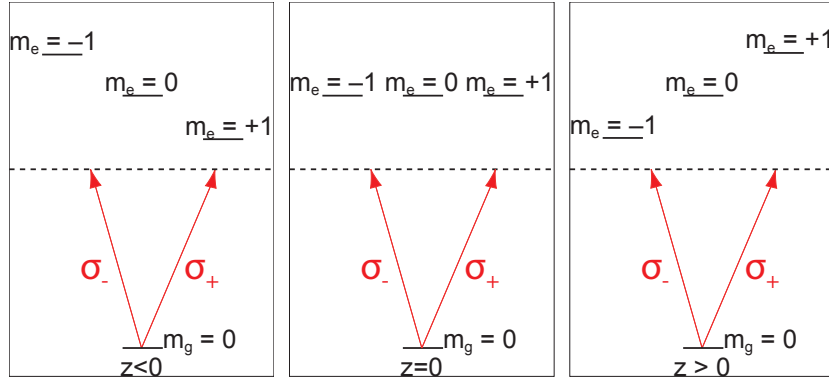


Figure 2.10: Position dependent Zeeman-shifts in a magneto-optical trap:

$z < 0$ : The  $m_e = -1$  gets lifted off-resonant (left).

$z = 0$ : The Zeeman levels are degenerate (middle).

$z > 0$ : The  $m_e = -1$  is shifted towards the light field frequency (right).

with the detuning

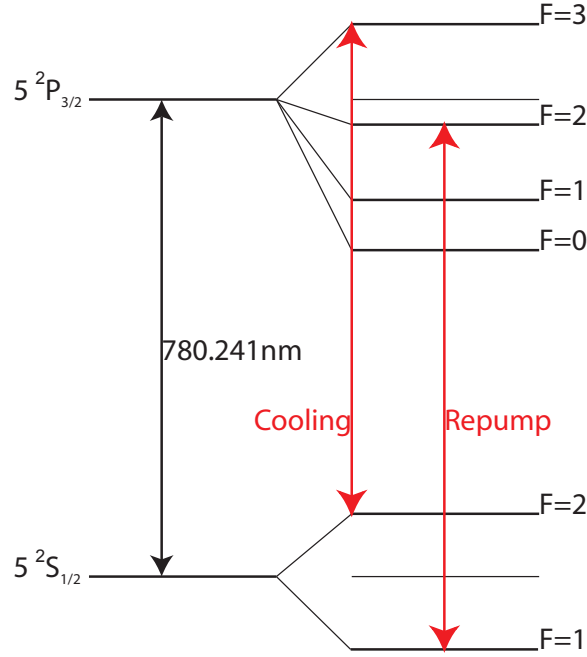
$$\delta_{\pm} = \delta \mp \vec{k} \cdot \vec{v} \pm \mu' B / \hbar. \quad (2.76)$$

As we have to trap  $^{87}\text{Rb}$  atoms, the level scheme is more complicated as in the description above. The main difference is the hyperfine structure, so  $^{87}\text{Rb}$  can absorb off-resonant light and get excited into the  $|5^2P_{3/2}, F = 2\rangle$  state (see fig. 2.11). From there it can decay to the  $|5^2S_{1/2}, F = 1\rangle$  state. In this case it would stop scattering light. To counteract this we excite it back to  $|5^2P_{3/2}, F = 2\rangle$  with repump light as illustrated in fig. 2.11 and keep the atom in the cooling cycle.

## 2.5.2 Optical dipole trap

The trapping of a single atom is a crucial step in our experiment. Provided with a reservoir of cold atoms by the magneto-optical trap we load the optical dipole trap with a single atom. This chapter gives a short introduction about the trapping mechanism and the forces that arise from the interaction with off-resonant laser light.

A light beam induces a dipole moment of the atom due to the oscillatory electric field and this generates a potential either attractive or repulsive, depending whether


 Figure 2.11: Level scheme of  $^{87}\text{Rb}$  for the magneto-optical trap

the light field is red or blue detuned from the atomic transition. We are using a red detuned optical dipole trap, so the force is attractive and the trap centre is at the position of the highest electric field, i.e. the focus of the laser beam.

### 2.5.2.1 Oscillator model

In an optical dipole trap the oscillating electric field of the trap beam induces a dipole moment  $\mathbf{d} = \alpha(\omega)\mathbf{E}$  oscillating with the same frequency  $\omega$  as the driving field  $\mathbf{E}$ . Here  $\alpha$  is the complex polarisability of the atom, different from the polarisabilities of Tab. 3.2 as these are valid only for the DC stark shift. On the basis of the classical Lorentz oscillator model [38] one can derive

$$\alpha = 6\pi\epsilon_0 c^3 \frac{\Gamma/\omega_0^2}{\omega_0^2 - \omega^2 - i(\omega^3/\omega_0^2)\Gamma}. \quad (2.77)$$

with  $\omega_0$  being the atomic transition frequency and  $\Gamma$  the on-resonance damping rate. Semiclassically  $\alpha$  can be computed with a two level atom interacting with a

radiation field. The potential of the interaction between the electric field and the dipole moment is

$$U_{dip} = -\frac{1}{2} \langle \mathbf{d} \mathbf{E} \rangle = -\frac{1}{2\epsilon_0^2 c} \Re(\alpha) \bar{I} \quad (2.78)$$

with  $\bar{I} = 2\epsilon_0 c E_0^2$  indicating the mean intensity of the trap beam and the brackets denote the time averages over the fast oscillating terms. Here we see that the potential is proportional to the intensity and the real part of the polarisability, whereas the imaginary part of the polarisability is proportional to the scattering rate

$$\Gamma_{sc} = \frac{P_{abs}}{\hbar\omega} = -\frac{\langle \dot{\mathbf{d}} \mathbf{E} \rangle}{\hbar\omega} = -\frac{1}{\hbar\epsilon_0 c} \Im(\alpha) \bar{I} \quad (2.79)$$

When  $\Gamma_{sc} \ll \Gamma$  the Lorentzian and the semiclassical picture have the same results. The damping rate  $\Gamma$  is given by

$$\Gamma = \frac{\omega_0^3}{3\pi\epsilon_0 \hbar c^3} |\langle e | \hat{\mathbf{d}} | g \rangle|^2, \quad (2.80)$$

where  $\hat{\mathbf{d}}$  is the electric dipole operator connecting the ground and excited states. Putting all together we can get the dipole potential and the scattering rate in the RWA

$$U_{dip} = -\frac{3\pi c^2}{2\omega_0^3} \left( \frac{\Gamma}{\omega_0 - \omega} + \frac{\Gamma}{\omega_0 + \omega} \right) I(\mathbf{r}) \approx \frac{3\pi c^2}{2\omega_0^3} \frac{\Gamma}{\Delta} I(\mathbf{r}) \quad (2.81)$$

$$\Gamma_{sc} = \frac{3\pi c^2}{2\hbar\omega_0^3} \left( \frac{\Gamma}{\omega_0 - \omega} + \frac{\Gamma}{\omega_0 + \omega} \right)^2 I(\mathbf{r}) \approx \frac{3\pi c^2}{2\hbar\omega_0^3} \left( \frac{\Gamma}{\Delta} \right)^2 I(\mathbf{r}) \quad (2.82)$$

with  $\Delta = \omega - \omega_0$  the detuning of the trap beam relative to the atomic resonance.

Dipole traps often use a focused laser beam so the intensity gets maximal in the focus. We have to distinguish two cases:

- $\Delta < 0$ :  $U_{dip}$  is negative and the atom gets attracted to the maximum of the so-called red detuned light field,
- $\Delta > 0$ :  $U_{dip}$  is positive and the atom experiences a repulsive force out of the focus.

In our case  $\Delta < 0$  and we get a conservative potential as drawn in fig: 2.12. Scattering light of the MOT beams effects friction and an atom is loaded from of the magneto-optical trap into the optical dipole trap.

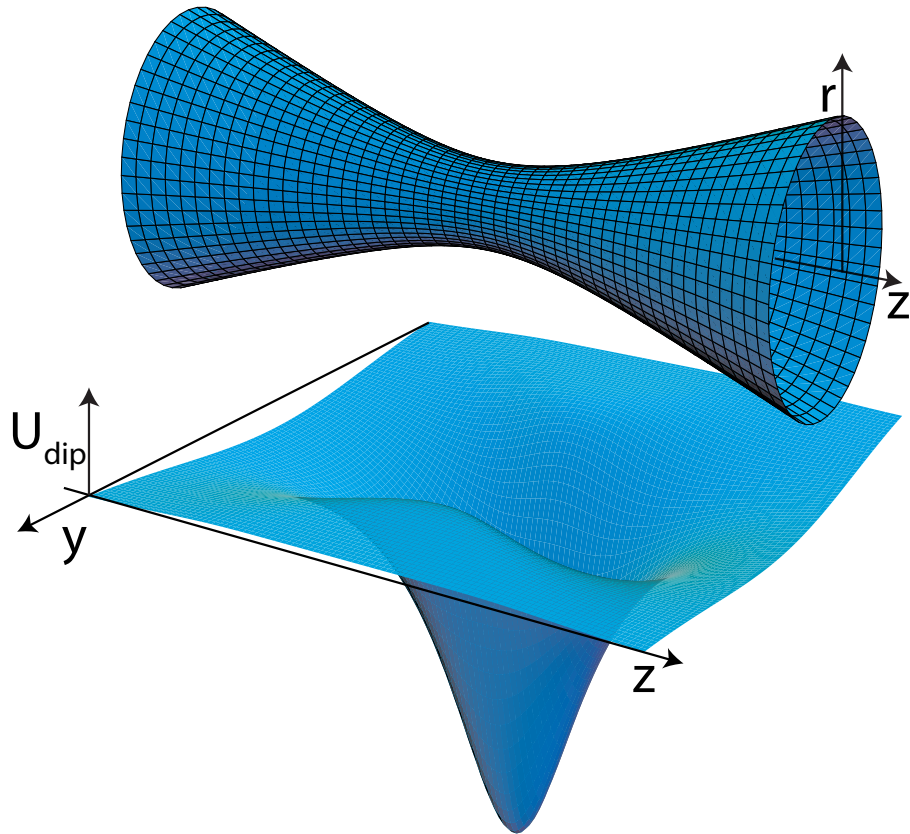


Figure 2.12: The upper figure shows the waist of the focused laser beam around the origin and the lower figure shows the potential induced by the light field in the  $z$ - $y$ -plane. In our setup we get a maximum trap depth of 1 mK

### 2.5.2.2 Quantum mechanical approach

In a fully quantum mechanical description the dipole trap effect can be treated as a second-order perturbation effect [22] of the atom with the perturbation Hamiltonian  $\mathcal{H}_{ED} = -\hat{\mathbf{d}}\hat{\mathbf{E}}$ . For non-degenerate states we get an energy shift  $\Delta E_i$  of

$$\Delta E_i = \sum_{j \neq i} \frac{|\langle j | \mathcal{H}_{ED} | i \rangle|^2}{E_i - E_j} \quad (2.83)$$

with  $E_i$  as the eigenvalues of the unperturbed Hamiltonian in the dressed state picture (see fig. 2.13).

We have a light field of frequency  $\omega$  and photon number  $N$ . In the first case, the atom is in the ground state  $|i\rangle$  and the light field consists of  $N$  photons, so the unperturbed energy  $E_i$  of the system is  $E_g = N\hbar\omega$ . In the second case, the atom is excited to the state  $|j\rangle$  with the eigenvalue  $\hbar\omega_j$  by absorbing one photon, the energy of the unperturbed system  $E_j = \hbar\omega_j + (N-1)\hbar\omega = \hbar\Delta_j + N\hbar\omega$ , where  $\Delta_j = \omega_j - \omega_0$  is the detuning of the light field to the atomic transition.

If we look at a simplified two level atom, eq. 2.83 becomes

$$\Delta E_{g/e} = \pm \frac{|\langle e | \hat{\mathbf{d}} | g \rangle|^2}{\Delta} |E(\vec{r})|^2 = \pm \frac{3\pi c^2}{2\omega_0^3} \frac{\Gamma}{\Delta} I(\vec{r}) \quad (2.84)$$

for the ground and excited states respectively.

The potential is the same as in the classical picture, but here the origin of the attractive force is generated by the light shift. As the atom is at low saturation mainly in the ground state the light shift of the ground state causes the relevant trapping potential.

**Multi-level atoms:** In the real experiment the atomic structure is more complicated. To get the trapping potential right we have to include the substructure into our calculations. We take all possible matrix elements  $\hat{\mathbf{d}}_{ij} = \langle g_i | \hat{\mathbf{d}} | e_j \rangle$  into account and introduce the reduced dipole matrix element  $\|\mathbf{d}\|$  depending on the wavefunction of the  $e^-$  and directly related to the decay rate of the transition we are dealing with. So the matrix elements reduce to

$$\mathbf{d}_{ij} = c_{ij} \|\mathbf{d}\|. \quad (2.85)$$

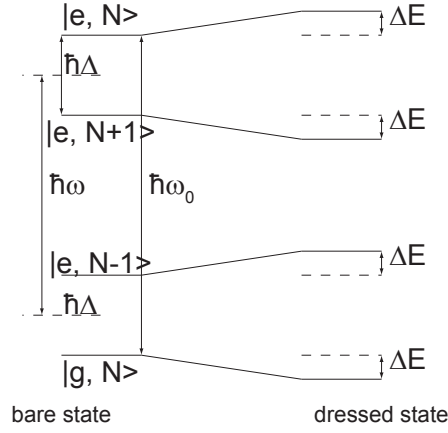


Figure 2.13: Dressed state picture:

The interaction between the atom and the light gives rise to an energy shift  $\Delta E$  (light shift) of the ground  $|g\rangle$  and excited  $|e\rangle$  state. The bare states have the transition frequency  $\omega_0$  and the light field's frequency is  $\omega$ .

The coefficients  $c_{ij} \in \mathbb{R}$  specify the transition strengths of the specific sublevels. These depend on the applied light field polarisations and the angular momenta of the respective atomic levels [21, 22].

We can neglect higher excited states in our calculations for the dipole potential [15].

**Rubidium-87** Neglecting further excited states than the first one, we can calculate the dipole potential according to eq. 2.83. This is the case if the hyperfine splitting of both the  $5^2S_{1/2}$  and  $5^2P_{3/2}$  states are smaller than the detuning  $\Delta$  of the trap laser. For the ground state  $5^2S_{1/2}$  with the total angular momentum  $F$  and the magnetic quantum number  $m_F$ , we get for the dipole potential

$$U_{dip} = \frac{\pi c^2 \Gamma}{2\omega_0^3} \left( \frac{2 + \wp g_F m_F}{\Delta_{2,F}} + \frac{1 - \wp g_F m_F}{\Delta_{1,F}} \right) \cdot I(\mathbf{r}) \quad (2.86)$$

with  $g_F$  the atomic Landé factor,  $\wp = \pm 1, 0$  for  $\sigma^\pm$ - or  $\pi$ -polarised light and  $\Delta_{1,F}$  and  $\Delta_{2,F}$  is the detuning to the D<sub>1</sub> and D<sub>2</sub> line respectively [38].

Because of the different potentials for certain magnetic sublevels it is important for our trap to shine in only linearly polarised light. Otherwise we would lose the spectral indistinguishability of the decay channels used for atom-photon entanglement [15].

For the scattering rate we get for linear polarised light

$$\Gamma_{sc} = \frac{\pi c^2 \Gamma^2}{2 \hbar \omega_0^3} \left( \frac{2}{\Delta_{2,F}^2} + \frac{1}{\Delta_{1,F}^2} \right) \cdot I(\mathbf{r}). \quad (2.87)$$

### 2.5.2.3 Single atom dipole trap with a Gaussian beam

We can create a three dimensional confinement of the atoms if we focus down the trap light, see fig. 2.12. For a Gaussian TEM<sub>00</sub> mode propagating along the z-axis we get the intensity

$$I(\mathbf{r}) = \frac{2P}{\pi w^2(z)} e^{-\frac{2r^2}{w^2(z)}}. \quad (2.88)$$

Here  $P$  is the power of the laser beam and  $r$  is the distance from the optical axis. The waist  $w(z)$  of the beam is the  $1/e^2$  radius and given by

$$w(z) = w_0 \sqrt{1 + z^2/z_R^2} \quad (2.89)$$

with the Rayleigh length  $z_R = \frac{\pi w_0^2}{\lambda}$ , the beam waist  $w_0$  and the wavelength  $\lambda$ . With all these one can calculate the maximum trap depth  $U_0$  for a two level atom

$$U_0 = \frac{3c^2}{\omega_0^3 w_0^2} \frac{\Gamma}{\Delta} P. \quad (2.90)$$

If we focus the trap beam down to a  $w_0 \leq 5 \mu\text{m}$  a blockade mechanism occurs and the number of atom trapped inside the optical dipole trap is either zero or one [19, 36]. This is caused by light-induced two-body collisions.

When this two-body collisions occur, two processes can take place. First, the atom is not in the  $5^2S_{1/2}, F = 1$ , the absolute ground state, but in the  $5^2S_{1/2}, F = 2$  state. The transition energy released in an inelastic collision is enough to eject both atoms out of the trap, even the transition energy is small. On the other hand, when the atom is in the excited state a loosely bound Rb<sub>2</sub> molecule can be formed. The recoil

of the spontaneously emitted photon kicks out both atoms of the trap while the molecule dissociates.

In the first case, the collision changes the attractive potential of the  $5^2S_{1/2} \rightarrow 5^2P_{3/2}$  molecular state to the repulsive  $5^2S_{1/2} \rightarrow 5^2P_{1/2}$  state potential. In the later, the molecule decays to the unbound ground state. The kinetic energy, necessary to leave the trap, arises in both processes from the fact, that the emitted photon of the  $\text{Rb}_2$  molecule has a longer wavelength than the photon absorbed during the formation of the molecules.

## 3 From theory to experiment

In our experiment we want to use the spontaneous decay of a single  $^{87}\text{Rb}$  atom to generate spin-entanglement between the atom and the emitted photon, thereby interfacing quantum memories (atoms) and quantum information channels (photons). To perform a loophole free test of Bell's inequality we aim to use the entanglement swapping protocol as described in 2.2.5.2 to generate entanglement between two remote atoms. For this purpose we need two entangled atom-photon pairs, whereby the atoms are trapped at remote locations. In order to close the detection and locality loophole at the same time we need a highly efficient and ultra-fast atomic state detection technique. While ordinary fluorescence techniques, based on the detection of several scattered photons, prove to be highly efficient [16], the respective measurement duration is limited for dipole transitions in the UV to NIR range by several  $10 \mu\text{s}$ . This would require a separation of the atoms by many 100 km. To overcome this drawback, we propose to use a state-selective laser ionisation process [22, 39, 40, 41] which should allow to perform projective spin measurements on a single trapped  $^{87}\text{Rb}$  atom in the sub- $\mu\text{s}$  domain.

In this chapter I will present the decay scheme for the generation of atom-photon entanglement [13] and all relevant experimental (respective theoretical) aspects of the atomic state detection.

### 3.1 Decay-scheme

Suppose a single optically trapped  $^{87}\text{Rb}$  is prepared in the first excited state  $|5^2P_{3/2}, F' = 0\rangle$  (see fig. 3.1). This state has zero angular momentum and decays into the ground state  $|5^2S_{1/2}, F = 1\rangle$  with angular momentum of  $F = 1$ . Due to conservation of angular momentum the polarisation of the emitted photon gets non-

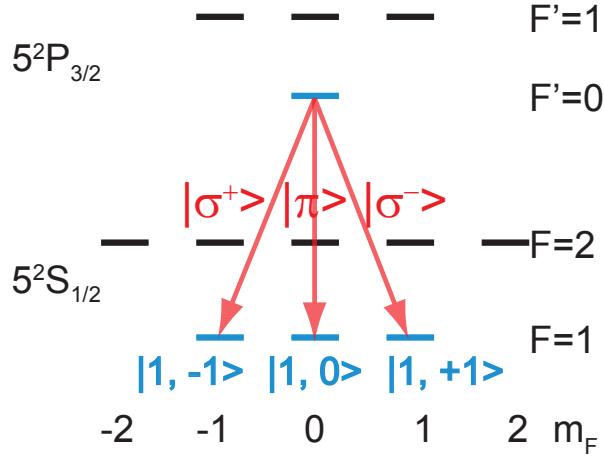


Figure 3.1: From the excited state  $|5^2P_{3/2}, F' = 0\rangle$  the single  $^{87}\text{Rb}$  atom can spontaneously decay into the ground state  $|5^2S_{1/2}, F = 1\rangle$  that has an angular momentum of  $F = 1$  with the projections  $m_F = 0, \pm 1$  onto the quantisation axis

classically correlated to the magnetic quantum number  $m_F = 0, \pm 1$  of the  $F = 1$  hyperfine ground state. Hence we get the entangled atom-photon state

$$\begin{aligned}
 |\Psi\rangle &= \sqrt{\frac{1}{8\pi}} \left[ \sqrt{\frac{1}{2}(1 + \cos^2 \theta)} (|\sigma^+\rangle |1, -1\rangle + |\sigma^-\rangle |1, +1\rangle) + \sin \theta |\pi\rangle |0, 0\rangle \right] \\
 &\otimes \sum_{\theta, \omega} g_\omega |\theta, \omega\rangle,
 \end{aligned} \tag{3.1}$$

where the atomic ground states are labelled by  $|F, m_F\rangle$ , the photonic polarisation states by  $|\sigma^\pm\rangle$  and  $|\pi\rangle$  and  $\theta$  describes the emission angle of the single photon with respect to the quantisation axis. The spatial and frequency mode of the emitted photon is described by  $\sum_{\theta, \omega} g_\omega |\theta, \omega\rangle$  [16]. If one restricts the observation of the photon (see appendix A.2.1.3) to the quantisation axis (or any other well defined axis)  $\pi$ -light is not observed and we get

$$|\Psi\rangle = \sqrt{\frac{1}{2}} (|\sigma^+\rangle |1, -1\rangle + |\sigma^-\rangle |1, +1\rangle) \tag{3.2}$$

Although the atom and the photon are spin-1 particles with this trick we reduce the Hilbert-space of each particle to a system with two degrees of freedom, i.e. a qubit, and get a maximally entangled atom-photon Bell state.

## 3.2 State detection of a single atom

In order to verify the entanglement between the atom and the photon, we must be able to read out the internal state of the atom. This state detection scheme consists of three steps (see fig. 3.2).

In a first step a stimulated adiabatic Raman passage (STIRAP) to the  $|5^2S_{1/2}, F = 2\rangle$  state is performed. With this technique one defines the measurement basis of the atom. After the transfer, the atom is illuminated with laser light resonant to the cycling transition  $|5^2S_{3/2}, F = 2\rangle \rightarrow |5^2P_{3/2}, F = 3\rangle$ . Together with a laser pulse at a wavelength of 473 nm the atom is excited to the continuum thereby breaking it up into an electron and a  $\text{Rb}^+$  ion. In the third step these ionisation fragments are detected with so called channel electron multipliers (CEM). With this techniques it should be possible to detect the atomic spin state within less than 1  $\mu\text{s}$  with a minimum efficiency of 0.95.

### 3.2.1 STIRAP

To analyse the Zeeman superposition state in arbitrary measurement bases we can use an extension of a stimulated adiabatic Raman passage the so-called tripod-STIRAP [15]. In contrast to Raman transitions with nearly resonant pulses of precise duration, this process is robust against moderate variations of the interaction parameters (intensity, pulse duration) of the STIRAP system, as long as the adiabaticity is maintained.

If one considers an atom with two ground states  $|1\rangle$  and  $|3\rangle$  and an excited state  $|2\rangle$  coupled by an electro-magnetic field  $\Omega_{12}$  (see fig. 3.3) two specific states exist with the following properties:

- The atom is initially in the state  $|3\rangle$  then nothing will happen. The light does not couple to  $|3\rangle$ , no transfer between the two ground states occurs and no

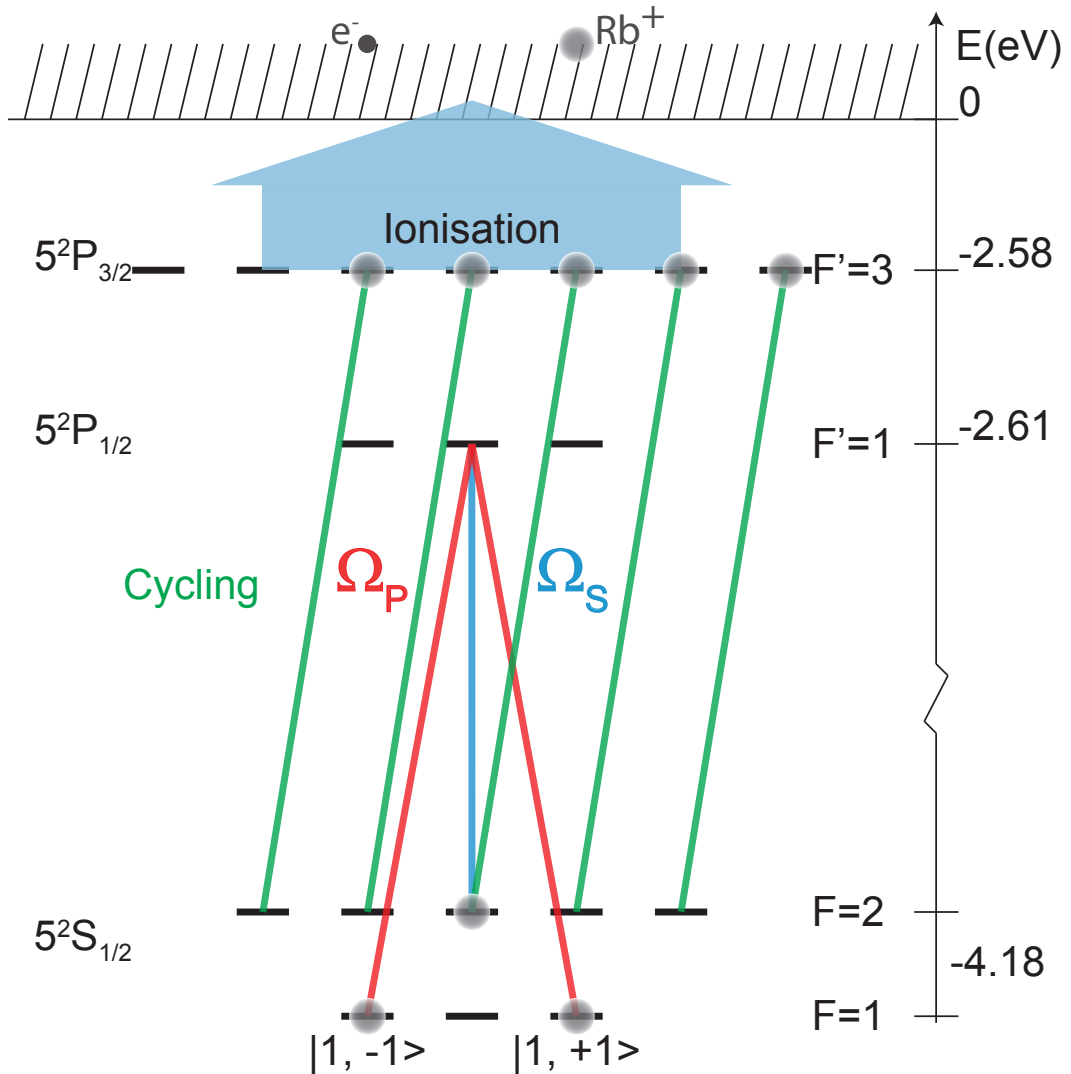


Figure 3.2: State selective ionisation after the  $\Lambda$ -decay. Starting at the Zeeman-sublevels the atom gets transferred with a stimulated adiabatic Raman passage to the state  $|5^2S_{1/2}, F = 2\rangle$ , excited to the state  $|5^2P_{3/2}, F' = 3\rangle$  and further on ionised.

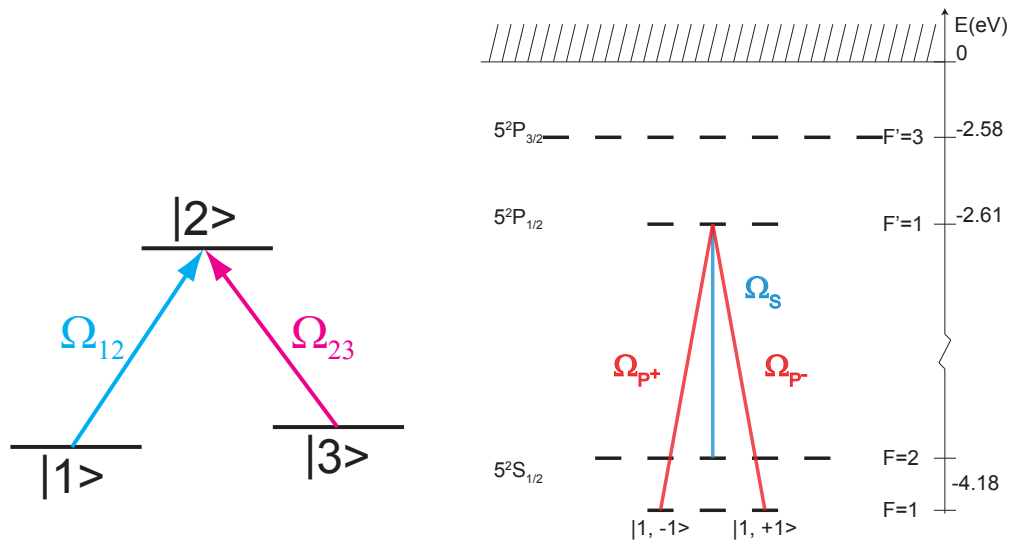


Figure 3.3: Left: The state  $|1\rangle$  is a bright state in a 3-level system, if we apply only  $\Omega_{12}$  whereas  $|3\rangle$  is a dark state with respect to the applied light field. Right: STIRAP transition of the two magnetic sublevels  $|5^2S_{1/2}, F=1, m_F = \pm 1\rangle$  to the hyperfine state  $5^2S_{1/2}, F=2$  of  $^{87}\text{Rb}$ .

light is scattered. Therefore state  $|3\rangle$  is called *dark state*.

- If the atom is initially in the state  $|1\rangle$ , orthogonal to the state  $|3\rangle$  it will be excited to the state  $|2\rangle$ . Via spontaneous emission the state  $|3\rangle$  gets populated and after a sufficiently large number of scattering events all the population gets transferred into  $|3\rangle$ . This process is called *optical pumping* and the initial atomic state is called a *bright state*.

Knowing this, one can think about the energy-degenerated Zeeman sublevels  $m_F = \pm 1$  of the hyperfine ground level  $F = 1$  of  $^{87}\text{Rb}$  (see fig. 3.3). If the light field with a specific polarisation does not couple to the initial ground state superposition the atom is in a dark state, whereas the light field with the orthogonal polarisation couples to the state.

More general, one can show that if two laser fields  $\Omega_{P+}$  and  $\Omega_{P-}$  couple to the transitions  $|+1\rangle \rightarrow |3\rangle$  and  $|-1\rangle \rightarrow |3\rangle$ , respectively, the relative phase  $\xi$  defines a dark ( $|\Psi_D\rangle$ ) and a bright ( $|\Psi_B\rangle$ ) superposition state

$$|\Psi_D\rangle = \cos \alpha \cdot |-1\rangle - \sin \alpha \cdot e^{i\xi} |+1\rangle \quad (3.3)$$

$$|\Psi_B\rangle = \cos \alpha \cdot |-1\rangle + \sin \alpha \cdot e^{i\xi} |+1\rangle \quad (3.4)$$

and therefore the atomic measurement basis. In our experiment the light fields  $\Omega_{P+}$  and  $\Omega_{P-}$  are generated by one laser field propagating along the quantisation axis  $z$ . Because this polarisation can be decomposed into a superposition of  $\sigma^+$ - and  $\sigma^-$ -polarisation with a relative phase and amplitude given by the polarisation, this allows to distinguish between different superpositions of the Zeeman sub-levels  $m_F = \pm 1$

**Theoretical model:** In the tripod stimulated adiabatic Raman passage the atom is described as a four level system with the two initial atomic ground states  $|\pm 1\rangle$ , the excited state  $|5^2P_{3/2}, F = 3\rangle = |2\rangle$  and the state we want to transfer to  $|5^2S_{1/2}, F = 2\rangle = |3\rangle$  (see fig. 3.4). In the rotating wave approximation and neglecting spontaneous decay from the  $|5^2P_{3/2}, F = 3\rangle$  state, the Schrödinger equation for the probability amplitudes is given by

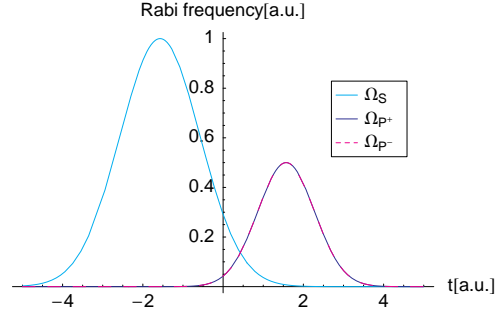


Figure 3.4: The three Gaussian pulses  $\Omega_S$ ,  $\Omega_{P+}$  and  $\Omega_{P-}$  are a possible realisation of the STIRAP. With these pulses a superposition of the states  $|+1\rangle$  and  $|-1\rangle$  can be transferred adiabatically to the state  $|3\rangle$ .

$$\frac{d}{dt}\mathbf{C}(t) = -i\mathbf{W}(t) \cdot \mathbf{C}(t) \quad (3.5)$$

with  $|\Psi(t)\rangle = c_{-1}|-1\rangle + c_2|2\rangle + c_{+1}|+1\rangle + c_3|3\rangle$  and

$$\mathbf{C}(t) = \begin{pmatrix} c_{-1} \\ c_2 \\ c_{+1} \\ c_3 \end{pmatrix} \quad (3.6)$$

and the time evolution operator

$$\mathbf{W}(t) = \begin{pmatrix} 0 & \Omega_{P+}(t) & 0 & 0 \\ \Omega_{P+}(t) & 0 & \Omega_{P-}(t) & \Omega_S(t) \\ 0 & \Omega_{P-}(t) & 0 & 0 \\ 0 & \Omega_S(t) & 0 & 0 \end{pmatrix}. \quad (3.7)$$

If we add the constant phase factors to the atomic states we get, without loss of

generality, the new states:

$$\begin{aligned} |\widetilde{-1}\rangle &= |-1\rangle \\ |\widetilde{+1}\rangle &= e^{-i(\Phi_{P^-} - \Phi_{P^+})} | +1\rangle \\ |\widetilde{2}\rangle &= e^{-i\Phi_{P^+}} |2\rangle \\ |\widetilde{3}\rangle &= e^{-i\Phi_S} |3\rangle \end{aligned}$$

and can define  $\Omega_{P^+}(t)$ ,  $\Omega_{P^-}(t)$  and  $\Omega_S(t)$  as real Rabi frequencies of the pump and Stokes pulses (see fig 3.2). The four eigenstates of  $\mathbf{W}(t)$  are then

$$\begin{aligned} \Phi_1(t) &= \begin{pmatrix} \cos \theta_t \\ 0 \\ -\sin \theta_t \\ 0 \end{pmatrix}, & \Phi_2(t) &= \begin{pmatrix} \sin \phi_t \sin \theta_t \\ 0 \\ \sin \phi_t \cos \theta_t \\ -\cos \phi_t \end{pmatrix} \\ \Phi_3(t) &= \begin{pmatrix} \cos \phi_t \cos \theta_t \\ 1 \\ \cos \phi_t \cos \theta_t \\ -\sin \phi_t \end{pmatrix}, & \Phi_4(t) &= \begin{pmatrix} \cos \phi_t \sin \theta_t \\ -1 \\ \cos \phi_t \cos \theta_t \\ \sin \phi_t \end{pmatrix}. \end{aligned}$$

The entire state  $|\Psi\rangle$  can be written as a linear superposition of the eigenvectors  $|\Psi\rangle = \sum_{i=1}^4 b_i \Phi_i$ . The time dependency of these states depends on the time dependent light fields  $\Omega_{P^+}(t)$ ,  $\Omega_{P^-}(t)$  and  $\Omega_S(t)$ :

$$\tan \theta_t = \frac{\Omega_{P^+}(t)}{\Omega_{P^-}(t)} \quad (3.8)$$

$$\tan \phi_t = \frac{\Omega_S(t)}{\sqrt{\Omega_{P^+}^2(t) + \Omega_{P^-}^2(t)}} \quad (3.9)$$

We want to transfer the state 3.4 to  $|3\rangle$ . Looking at the eigenvectors  $\Phi_i(t)$  of  $\mathbf{W}(t)$ , for the states  $\Phi_1(t)$  and  $\Phi_2(t)$  the amplitude of the excited state is 0. Then no spontaneous decay can occur which makes the state important for us.  $\Phi_1$  and  $\Phi_2$  are called the adiabatic eigenvectors<sup>1</sup>. In our experiment we want to transfer well

<sup>1</sup>An adiabatic change of state happens if the eigenstates change as the time evolution operator, hence  $\frac{d}{dt}b_i = 0$

### 3 From theory to experiment

---

defined superposition states. This requires that the ratio of  $\Omega_{P+}$  and  $\Omega_{P-}$  is constant over time. In this way  $\theta_t$  and therefore the state  $\Phi_1$  only depend on the light field polarisation, defined by the fields  $\Omega_{P+}$  and  $\Omega_{P-}$ . For the transfer  $|\pm 1\rangle \rightarrow |3\rangle$  we start with the Stokes pulse  $\Omega_S$  and after a certain time the two pump pulses  $\Omega_{P\pm}$  as shown in fig. 3.4 are switched on adiabatically while the Stokes pulse  $\Omega_S$  is switched off. As the Rabi frequencies  $\Omega_{P+}$  and  $\Omega_{P-}$  are the same, we therefore get for the angles in 3.9

$$\phi_{t \rightarrow -\infty} = \frac{\pi}{2}, \quad \phi_{t \rightarrow \infty} = 0 \quad (3.10)$$

$$\tan \theta_t = \frac{\Omega_{P+}(t)}{\Omega_{P-}(t)} = \text{const.} \Rightarrow \theta_{t \rightarrow \infty} = \text{const.} \quad (3.11)$$

In this way the atomic state  $|\Psi\rangle_B$  in eq. 3.4 is transferred to  $|3\rangle$  depending on the population of the initial state and the polarisations of the STIRAP pulses.

With the angles 3.11 the populations  $P_i$  of the various states  $|i\rangle$  become

$$P_3(t \rightarrow \infty) = |\cos \alpha \sin \theta_\infty + \sin \alpha \cos \theta_\infty e^{i\Delta}|^2 \quad (3.12)$$

$$P_{-1}(t \rightarrow \infty) + P_{+1}(t \rightarrow \infty) = 1 - P_3(t \rightarrow \infty) \quad (3.13)$$

The phase between the pump pulses  $\phi_{P+} - \phi_{P-}$  and the atomic state  $\xi$  determine the phase  $\Delta = \xi - (\phi_{P+} - \phi_{P-})$  [42].

Adjusting the phase  $\phi_{P+} - \phi_{P-}$  of the pump pulses defines which superposition is transferred to  $|3\rangle$  and provides an opportunity to analyse any superposition of the states  $|\pm 1\rangle$  if we fulfil the condition for an adiabatic change of atomic population, i.e., the angles 3.9 change slowly ( $\frac{d}{dt}\theta_t \ll \Omega(t) \gg \frac{d}{dt}\phi_t$ ) compared to the effective Rabi frequency

$$\Omega_{eff}(t) = \sqrt{\Omega_{P+}^2(t) + \Omega_{P-}^2(t) + \Omega_S^2(t)}. \quad (3.14)$$

Experimentally this is realised by high laser power leading to high Rabi frequencies to keep the overall time of the analysis short.

With the STIRAP technique the atomic state  $|5^2S_{1/2}, F = 1\rangle$  can be transferred very fast within less than 50 ns and with a high accuracy to the  $|5^2S_{1/2}, F = 2\rangle$  state for

Ionisation cross section $\sigma_p[m^2]$	wavelength [nm]	ref.
$(1.4 \pm 0.1) \cdot 10^{-21}$	413.1	[43]
$(1.3 \pm 0.1) \cdot 10^{-21}$	406.7	[43]
$(1.0 \pm 0.3) \cdot 10^{-21}$	440	[44]
$(1.5 \pm 0.2) \cdot 10^{-21}$	476.5	[45]
$(1.1 \pm 0.3) \cdot 10^{-21}$	425.6	[40]

Table 3.1: Ionisation cross section of the  $5^2P_{3/2}$  state of  $^{87}\text{Rb}$  for different wavelengths.

any superposition of the magnetic sublevels  $|\pm 1\rangle$ . In this way the measurement basis of the atomic state can be selected. Together with the polarisation measurement of the emitted photon this detection process allows to verify the entanglement between the atom and the photon [13, 16].

### 3.2.2 Ionisation

With the STIRAP technique the Zeeman qubit  $|F = 1, m_F = \pm 1\rangle$  is in a coherent manner mapped onto two non-degenerate hyperfine ground levels  $|F = 1\rangle$  and  $|F = 2\rangle$  of the  $5^2S_{1/2}$  ground state. In order to read out the atomic hyperfine levels we plan to state-selectively ionise the atom. Therefore a detection laser pulse excites the atom (if it was transferred to  $F = 2$ ) to the  $|5^2P_{3/2}, F' = 3\rangle$  state, from where a laser at a wavelength of 473 nm couples it to an unbound continuum state breaking it up into a photoelectron  $e^-$  and a  $\text{Rb}^+$ -ion.

The main property of an ionisation process is that the final state  $|f\rangle$  belongs to the continuum. Therefore the transition rate  $\Gamma_{i \rightarrow f}$  from a bound state to a continuum state is given by Fermi's golden rule

$$\Gamma_{i \rightarrow f} = \frac{2\pi}{\hbar} |\langle f | \mathcal{H}' | i \rangle|^2 \rho(E_i + E_p), \quad (3.15)$$

where  $E_i = -\hbar\omega_{ion} = -E_{ion}$  is the ionisation energy of the initial state  $|i\rangle$ ,  $E_p = \hbar\omega_p$  the energy of a photon of the ionisation laser,  $\mathcal{H}'$  the interaction Hamiltonian (see

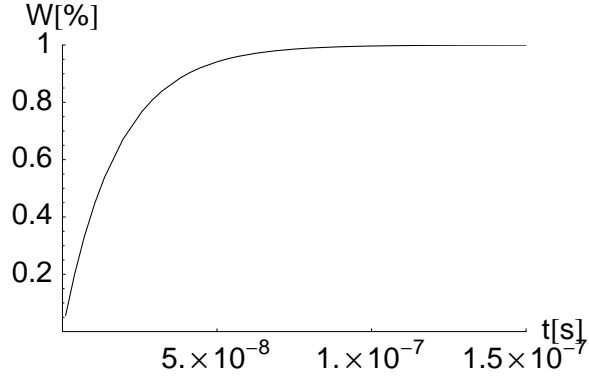


Figure 3.5: Calculated ionisation probability  $W$  of a  $^{87}\text{Rb}$  atom as a function of time  $t$  for the parameters: laser power  $P = 100$  mW, beam waist  $1 \mu\text{m}$ , wavelength  $\lambda_p = 473$  nm and ionisation cross section  $\sigma_p = 1.5 \cdot 10^{-21} \text{ m}^2$ .

e.g. eq. 2.49)) and  $\rho$  the density of states within  $[E_i, E_p]$ . If we want to express the transition rate  $\Gamma_{i \rightarrow f}$  as a scattering cross-section one can do this with the help of the photon flux density  $\Phi = \frac{I_p}{\hbar\omega_p}$ , i.e. the number of photons travelling through the cross section per unit time,

$$\Gamma_{i \rightarrow f}(\omega_p, I_p) = \sigma_p(\omega_p)\Phi. \quad (3.16)$$

The ionisation energies of the  $5^2S_{1/2}$  and  $5^2P_{3/2}$  states are 4.2 eV and 2.6 eV, respectively. For the  $5^2P_{3/2}$  state this corresponds to a transition wavelength of  $\lambda < 479$  nm.

In order to estimate the time needed to ionise the trapped  $^{87}\text{Rb}$  atom, we get for the mean transition rate

$$\Gamma_{i \rightarrow f} = \Gamma_{ion} = \frac{I_p f \sigma_p}{E_p}. \quad (3.17)$$

Because the atomic transition  $|5^2S_{1/2}, F = 2\rangle \rightarrow |5^2P_{3/2}, F' = 3\rangle$  is saturated by the detection laser, we can estimate the mean population  $f$  of the  $|5^2P_{3/2}, F' = 3\rangle$  state to be 0.5. In a simple rate-equation model the probability to ionise the trapped

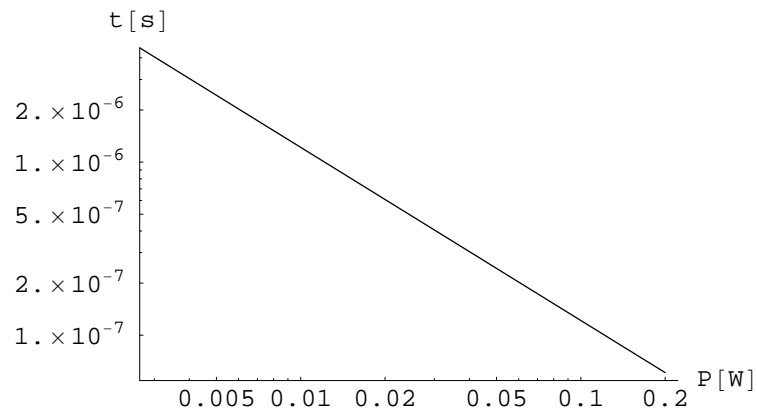


Figure 3.6: Time  $t$  needed to obtain an ionisation probability  $W$  of 99.9% as a function of the power  $P$  of the blue laser at a wavelength of  $\lambda_P = 473$  nm, for a beam waist  $w_0 = 1.0\mu\text{m}$  and an ionisation cross section of  $\sigma = 1.5 \cdot 10^{-21}\text{m}^2$ . For a laser power of 100 mW the ionisation time is 121.6 ns.

### 3 From theory to experiment

Ground state polarizability	$\alpha_0(5^2S_{1/2})$	$h \cdot 0.0794(16)Hz/(V/cm)^2$	[46]
D <sub>1</sub> scalar polarizability	$\alpha_0(5^2P_{1/2})$	$h \cdot 0.201706(16)Hz/(V/cm)^2$	[47]
D <sub>2</sub> scalar polarizability	$\alpha_0(5^2P_{3/2})$	$h \cdot 0.21410(8)Hz/(V/cm)^2$	[48]
D <sub>2</sub> tensor polarizability	$\alpha_2(5^2P_{3/2})$	$-h \cdot 0.0406(8)Hz/(V/cm)^2$	[48]

Table 3.2: Scalar polarisabilities of the  $5^2S_{1/2}$  ground and the  $5^2P_{1/2}$ ,  $5^2P_{3/2}$  excited states and the tensor polarizability of the  $5^2P_{3/2}$  state.

atom is given by [45]:

$$\begin{aligned}
 \frac{dW(t)}{dt} &= -\Gamma_{ion}W(t) \\
 W(t) &= 1 - e^{-\Gamma_{ion}t} \\
 &= 1 - e^{-\frac{I_p\sigma_p}{2E_p}t}
 \end{aligned}
 \tag{3.18}$$

Fig. 3.5 shows the calculated ionisation probability as a function of time. For  $\lambda_p = 473$  nm the ionisation cross section can be well approximated by  $\sigma_p = 1.5 \cdot 10^{-21}$  m<sup>2</sup> [45]. Using 100 mW of laser power focused down to a waist of 1  $\mu$ m we can ionise the atom after 120 ns with a certainty of 99.9% (see fig. 3.6).

#### 3.2.3 Detection of the ionisation fragments

After the ionisation pulse we have to detect whether the atom was ionised or not. Therefore we have to detect the fragments of the ionised atom.

For this purpose we use two opposing channel electron multipliers (CEM) which are used for the detection of the photoelectron and the Rb<sup>+</sup>-ion, respectively. Therefore we have to apply an electric field between the two detectors, so that the e<sup>-</sup> and the Rb<sup>+</sup> are accelerated to the respective CEM.

Analogous to a magnetic field causing the Zeeman effect, the applied electric field gives rise to the DC Stark effect. For a static electric field  $E_z$  (i.e. the shift is small compared to the hyperfine splitting), the energy shift [20] of the Zeeman sublevels

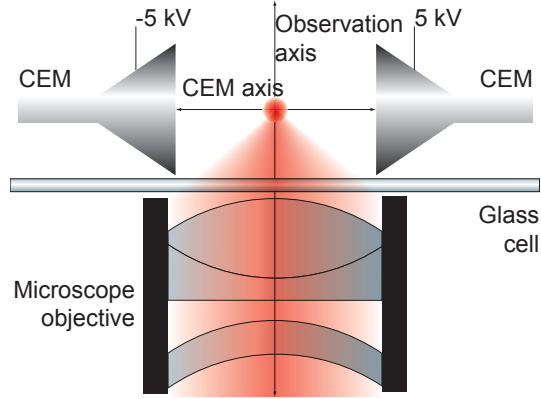


Figure 3.7: The symmetry axis of the CEMs is perpendicular to the observation direction of scattered fluorescence light.

is given by

$$\begin{aligned} \Delta E_{|J,I,F,m_F\rangle} &= -\frac{1}{2}\alpha_0 E_z^2 - \frac{1}{2}\alpha_2 E_z^2 \times \\ &\times \frac{[3m_F^2 - F(F+1)][3X(X-1) - 4F(F+1)J(J+1)]}{(2F+3)(2F+2)(F(2F-1)J(2J-1))}, \end{aligned} \quad (3.19)$$

with

$$X = F(F+1) + J(J+1) - I(I+1). \quad (3.20)$$

and  $\alpha_0$  and  $\alpha_2$  being the scalar and tensor polarizability (See tab. 3.2). The second term depending on the tensor polarisability  $\alpha_2$  is nonvanishing only for  $j = 3/2$  levels. The first term shifts all the magnetic sublevels with a given  $j$  together. Especially for the  $5^2S_{1/2}$ ,  $F = 1$  ground state the DC-Stark effect shifts all magnetic sublevels by the same amount. This important property guarantees that even if we apply electric acceleration field gradients of 10 kV/cm the atom-photon entanglement remains unaffected.

**Summary** As a conclusion we can say that it is possible to detect the magnetic sublevels of a single  $^{87}\text{Rb}$  atom in the  $|5^2S_{1/2}, F = 1\rangle$  state within  $1 \mu\text{s}$  via state-selective ionisation. The atom-photon entanglement is not disturbed by the implementation of CEM due to the DC Stark shift. In this way we should be able to generate atom-

### *3 From theory to experiment*

---

photon entanglement detection with a fast and high-efficient state detection of the atom.

## 4 Experimental setup

In the preceding chapter I described theoretical aspects which are necessary for the understanding of our experiment. In this chapter I will introduce our experiment and will show the experimental steps to trap a single  $^{87}\text{Rb}$  atom optically.

One vital ingredient towards the trapping of a single  $^{87}\text{Rb}$  atom is the stable operation of an optical dipole trap (ODT). Using a microscope objective with a high numerical aperture we obtain a comparable high detection efficiency of photons scattered by the single atom. To ensure that only a single atom is trapped a blockade mechanism [36] is used which prevents double occupancy. Accordingly, this requires a large solid angle of the detection and trapping optics in a confocal arrangement and has been a main design criterion of our detection optics as the collisional blockade mechanism can be observed only for focal spot diameter  $< 5 \mu\text{m}$  [36].

To load the optical dipole trap we initially prepare a magneto-optical trap (MOT), providing us with a reservoir of cold atoms. To ease the optical access to the dipole trap region and to save laser power the design of the magneto-optical trap is chosen to be a retro-reflecting MOT.

After the installation and characterisation of the magneto-optical trap, the setup of the optical dipole trap is described. This is realised by a confocal arrangement in which we overlap simultaneously the trapping and the ionisation beam with the fluorescence detection. Once the atom is caught in the trap, in a first approximation, the lifetime of the atom is only limited by the collision rate with atoms from the hot background gas. To reduce this background pressure we assemble an ultra-high vacuum (UHV) chamber together with a glass cell as the experimental area. The setup of the vacuum is presented in the beginning of this chapter. Afterwards the

## 4 Experimental setup

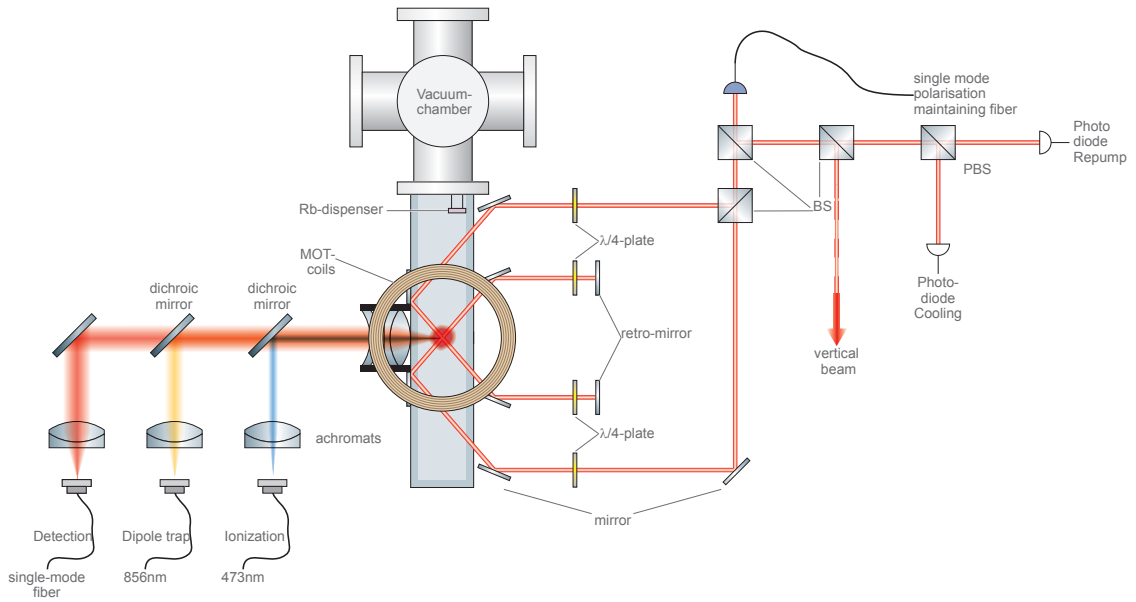


Figure 4.1: Schematic topview of the magneto-optical trap and the confocal dipole trap setup on the vacuum table:

The cooling and repump light is transferred from the optical table to the vacuum table in a polarisation maintaining fibre. The beam is split up into four beams with three 50/50 beam splitters (BS). Three of the beams are used for the magneto-optical trap and the fourth is guided to an polarising beam splitter. There the cooling and repump light is separated and the intensities of both are monitored with a photo diode accordingly. A control circuit stabilises the power of the cooling and repump light individually by regulating the amplitude of the respective AOM signal. This is done with an electronic circuit shown in fig. A.4 of the appendix.

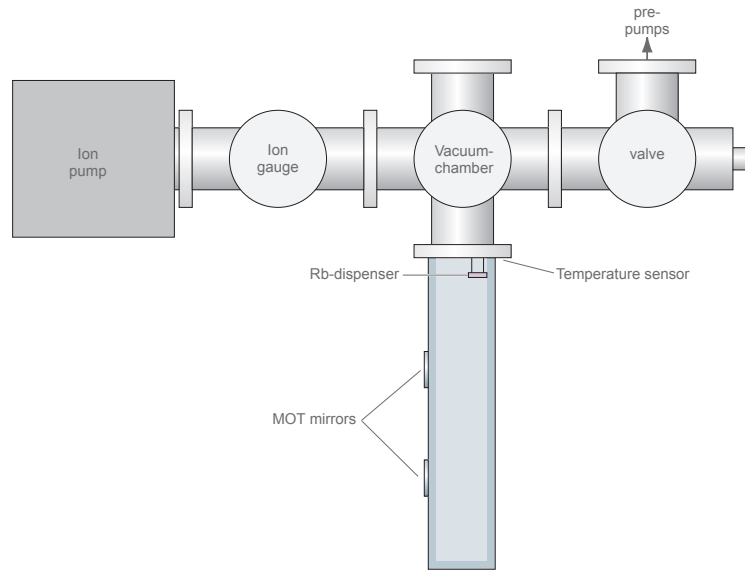


Figure 4.2: Schematic setup of the vacuum chamber pumped by a Varian VacIon Plus 20 ion getter pump. The temperature sensor outside the vacuum chamber is only installed during the bakeout procedure to monitor the temperature close to the Indium seal between the glass cell and the flange.

devices, which we further need for the trapping of a single  $^{87}\text{Rb}$  atom are presented.

## 4.1 Vacuum chamber

For pressures  $p \leq 10^{-9}$  mbar we expect a lifetime of the atom in the trap of  $\tau \geq 1$  s. For the enclosure of the magneto-optical trap and the optical dipole trap we use a glass cell (see fig. 4.2). It is sealed to a milled flange with a 2mm Indium (In) wire (a schematic drawing is given in fig. 4.2). On one outer surface of the glass cell reflecting coating is applied to enable back reflection of the trap beams for the MOT. This is done to achieve maximum optical access to the experimental area, as we will place the objective of the confocal microscope as close as possible to the glass cell, right in between the coated areas. Hence we are able to collect light from

#### 4 Experimental setup

---

the atom using the full numerical aperture (NA=0.6) of the microscope objective. To provide a controlled vapour pressure of Rb, dispensers are mounted inside the UHV chamber. As pure Rb metal has a vapour pressure at room temperature of  $6.7 \cdot 10^{-7}$  mbar [20] we can not use pure Rb. To circumvent a possible sublimation, Rb is mixed with other alloys inside the dispensers. We installed two different types, one SAES getters<sup>1</sup> and one Alvatec<sup>2</sup> dispenser.

The SAES device contains the anhydrous alkali metal salt  $\text{Rb}_2\text{CrO}_4$  together with a reducing agent alloy consisting of Zr 84%-Al16% (St101). Heating up the dispenser to a temperature of  $T_{\text{dispenser}} \approx 650^\circ\text{C}$ , a reduction reaction between the chromate and the alloy starts and pure Rb begins to evaporate. The Alvatec dispenser contains high melting intermetallic alkali compounds. It is sealed with Indium and the RbBi alloy is stored under a pure argon atmosphere. Both dispensers have in common that they are heated up via ohmic, resistance heating with typical evaporation currents of 6-7 A. The advantage of the Alvatec dispenser is that it evaporates less atmospheric contaminations than the SAES dispenser. Therefore we can achieve a higher partial pressure of Rb at a lower total pressure. We tested the SAES dispenser by heating with a current of 3 A and 7 A, respectively. For the first heating procedure, some surface deposits are evaporated. However for higher currents, pure Rb gets evaporated along with additional impurities which are evaporated out of the bulk of the material (see fig. 4.3).

After assembling the entire vacuum chamber we carried out a bakeout procedure to clean the apparatus. Due to the low melting point of Indium ( $156.6^\circ\text{C}$ ) the maximum temperature for the bakeout was chosen to  $100^\circ\text{C}$  measured at the transition flange close to the glass cell (see fig. 4.2). To avoid high temperature gradients in the system we increased the temperature by 2.5 K per hour. In fig. 4.4 one can see the progress of the pressure in time. Every time the pressure rises we increased the temperature by 5 K.

After cooling down the apparatus again we reached a final pressure of  $9.5 \cdot 10^{-10}$  mbar. The remaining bias pressure seems only to be limited due to internal leaks.

---

<sup>1</sup><http://www.saesgetters.com>

<sup>2</sup><http://www.alvatec.com>

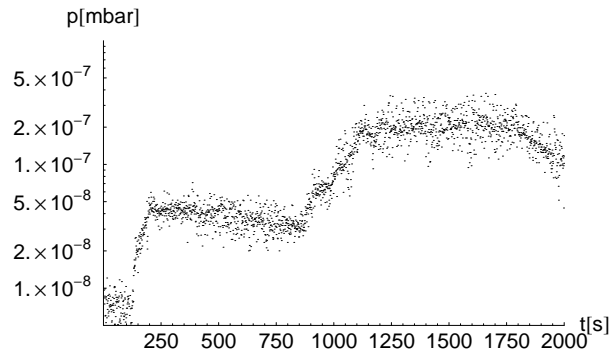


Figure 4.3: Heat up of the SAES dispenser. At the time  $t = 100\text{s}$  we apply a current of  $I = 3\text{A}$  and the pressure rises fast. Hence we evaporate only surface deposits and clean the dispenser. After  $t = 850\text{s}$  we rise the current to  $7\text{A}$ . The pressure rises slowly, reaches an equilibrium and stops increasing at  $p \approx 2 \cdot 10^{-7}$  mbar.

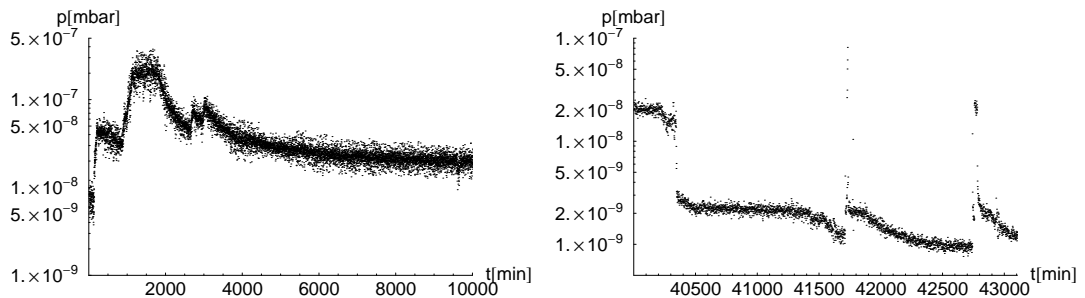


Figure 4.4: Pressure during bakeout of the vacuum chamber. The pressure rises every time we increased the temperature by  $5\text{K}$ . During the first night (between  $1750\text{min}$  and  $2500\text{min}$ ) and after  $50\text{h}$  we see an exponential decay of the pressure for nearly 5 days.

Right: Pressure during the cooling down cycle from  $100^\circ\text{C}$  to room temperature. The peaks occur as we turned on the dispenser to clean them. In the end we reach a residual bias pressure of  $9.5 \cdot 10^{-10}$  mbar.

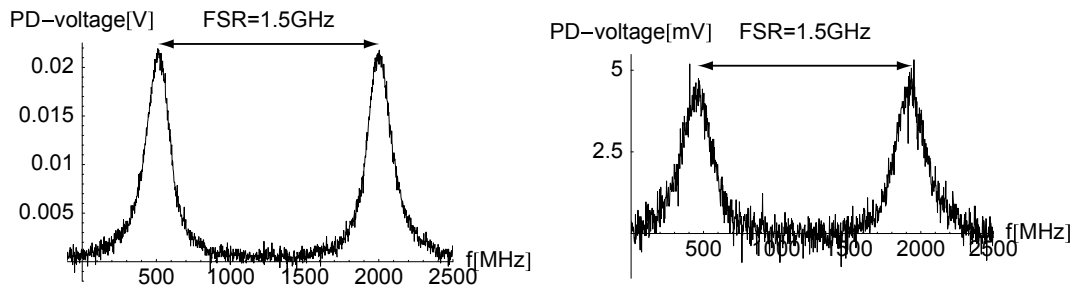


Figure 4.5: Cavity signals of the Cooling (left) and Repump (right) Laser.

Small external leaks have been detected with a mass spectrometer sensitive to Helium and closed with a Vacseal<sup>3</sup> spray.

## 4.2 Laser system

### 4.2.1 Cooling and repump laser

As depicted in fig. 2.11 we have to use two different laser frequencies for our MOT, the cooling and the repump laser. The corresponding laser systems are set up on a second, separate mobile table. Light is transferred via polarisation maintaining fibres to the experimental setup on the vacuum table.

The cooling laser consists of a compact grating stabilised diode laser at a wavelength of 780 nm with a linewidth of 0.6 MHz [49]. The grating can be tilted via a piezoelectric actuator. By tuning this additional external cavity one can continuously tune the laser frequency for several GHz without *mode hopping*. The temperature of the laser resonator is stabilised by a commercially available temperature controller adapted to the setup<sup>4</sup>. The setup of the entire laser table is shown in fig. A.2. To operate the MOT properly the frequency of the laser diode is locked on a Doppler-free saturation spectroscopy signal (see fig. 4.6)[50, 51]. To check whether the laser operates on a single, transverse mode, we monitor the mode structure with a confocal

<sup>3</sup><http://www.2spi.com>

<sup>4</sup>Thorlabs ITC 102

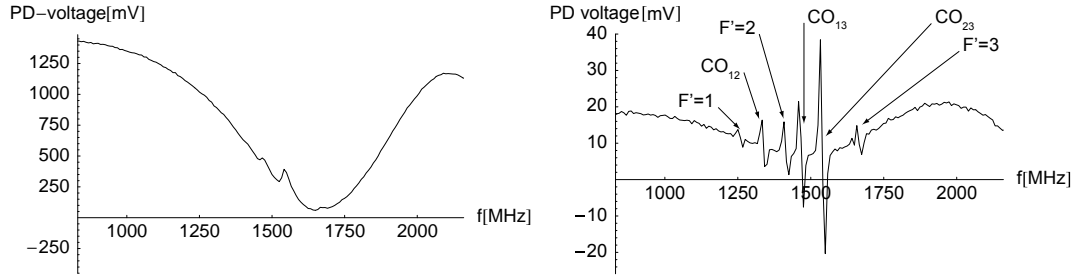


Figure 4.6: Spectroscopy signal and the dispersive locking signal [50] of  $^{87}\text{Rb}$  transitions  $|5^2S_{1/2}, F = 2\rangle \rightarrow |5^2P_{3/2}, F' = 1, 2, 3\rangle$ . The laser is locked on the crossover of the lines  $F = 2 \rightarrow F' = 1$  and  $F = 2 \rightarrow F' = 3$ .

scanning Fabry-Perot interferometer (FPI). The corresponding transmission signal recorded by a photo diode (PD) is shown in fig. 4.5.

The finesse of a cavity is

$$F = \frac{\pi}{2 \arcsin\left(\frac{1-\sqrt{\rho}}{2\sqrt[4]{\rho}}\right)} \approx \frac{\pi}{1-\sqrt{\rho}} \approx \frac{2\pi}{1-\rho} \quad (4.1)$$

where  $\rho$  is the reflectivity of the mirrors. In our case it is 98.9% and we reach a finesse of 570. The free spectral range of the cavity used for both cooling and repump light is

$$FSR = \frac{c}{4L}. \quad (4.2)$$

With  $L = 5$  cm we get a free spectral range of 1.5 GHz.

We lock the cooling laser to the crossover (CO) signal between the  $5^2P_{3/2}, F' = 1$  and  $5^2P_{3/2}, F' = 3$  states (see A.3). In this way the laser remains stable and locked for up to 10h. The lock system controls the wavelength of the laser by tilting the grating of the external laser resonator with a piezoelectric actuator. The respective spectroscopy signals for the cooling laser is shown in fig. 4.6.

To shift the frequency to the cycling transition  $|5^2S_{1/2}, F = 2\rangle \rightarrow |5^2P_{3/2}, F' = 3\rangle$ , we use an acousto-optical modulator (AOM) double pass setup at a frequency of 97 MHz. With the AOM we can adjust the detuning  $\Delta$  of the cooling laser up to

## 4 Experimental setup

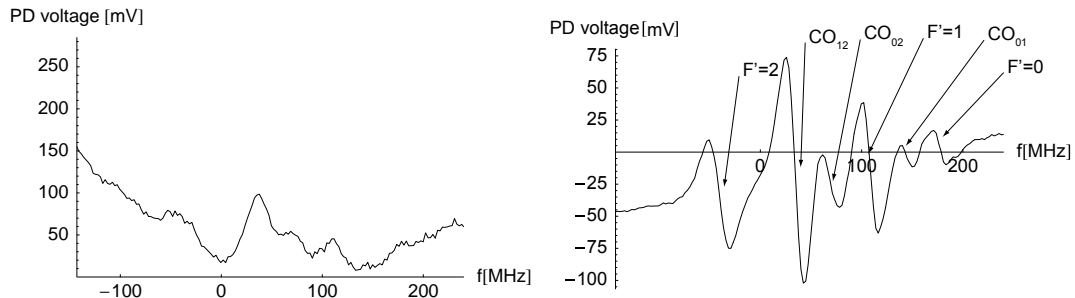


Figure 4.7: Spectroscopy signal and the regulation signal [50] of  $^{87}\text{Rb}$  for the transitions  $|5^2S_{1/2}, F = 1\rangle \rightarrow |5^2P_{3/2}, F' = 0, 1, 2\rangle$ . The laser is locked on the  $\text{CO}_{12}$

several natural linewidths [50, 52].

In a MOT, there is also off-resonant excitation to the  $F' = 2$  state (see fig. 2.11) and a consecutive decay channel into the non-resonant  $F = 1$  ground state.

To avoid losing atoms in this (dark) state we shine in additional light, so-called repump light, to excite the atom back to the  $5^2P_{3/2}, F' = 2$  state. In this way atoms are pumped back into the cooling cycling process.

The repump laser is locked to the CO signal between the  $F' = 1$  and  $F' = 2$  levels of the  $5^2P_{3/2}$  state (see fig. 4.7). To shift the frequency to the repump transition  $5^2S_{1/2}, F = 1 \rightarrow 5^2P_{3/2}, F' = 2$  we use an AOM in a single pass configuration setup at a frequency of 79 MHz.

To ensure a perfect spatial overlap of the cooling and repump light at the MOT setup, the light is overlapped on a polarising beam splitter (PBS), coupled into a polarisation maintaining single mode optical fibre and guided to the vacuum table. Polarisation maintaining optical fibres ensure that two well defined, perpendicular linear polarisations can be guided without phase shifts due to stress induced birefringence. For proper alignment the incoupled polarisation is rotated such that it hits the preferential axis. After the incoupled polarisation is aligned in a proper way,

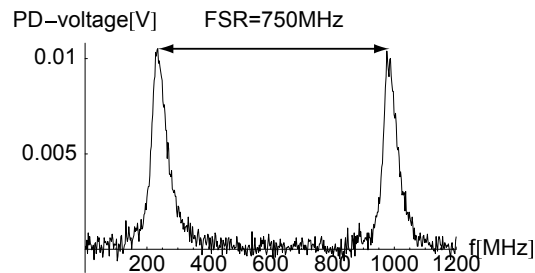


Figure 4.8: Cavity signal of the dipole trap Laser.

the outcoupled polarisation is stable<sup>5</sup> within 1.1%.

### 4.2.2 Dipole trap Laser

For the dipole trap a diode laser system similar to the cooling and repump setup [49] is established but at a wavelength of 853 nm. Here we do not need a frequency stabilised laser system and hence no RF spectroscopy for locking (see fig. A.2) is applied.

We collimate the laser light inside the laser head and compensate the ellipticity of the beam with an anamorphic prism pair. To protect the diode against any back reflections that can cause damage to the diode<sup>6</sup> an optical isolator with an isolation of -39.5 dB is installed in front of the laser diode. To monitor if the laser operates on a single longitudinal mode we observe the transmission signal of a scanning Fabry-Pérot interferometer (see fig. 4.8). This time a cavity with a calculated finesse of 600 and a free spectral range of 750 MHz is used.

To control the depth of the dipole potential we use an AOM and couple the dipole-

<sup>5</sup>Technical note: For the optimisation, knowing that we shine in a defined linear polarisation we put a polariser after the fibre and adjust it in a way that the transmitted intensity is minimal. Than we heat up the fibre and see the polarisation turned inside the fibre. The ratio  $\frac{\Delta U}{U_0}$  of the maximum of the oscillations  $\Delta U$  and the mean intensity  $U_0$  without polariser define the 1.1%

<sup>6</sup>These reflections are mainly caused by coupling into the optical fibre.

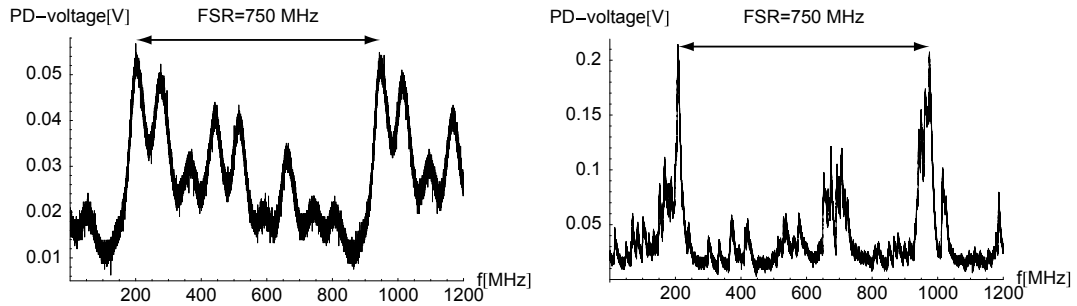


Figure 4.9: Cavity signal of the Laser Quantum (left) and the Shanghai Dream (right) lasers.

The Laser Quantum laser is running stable on a few modes. In contrast the Shanghai Dream laser is that unstable that the cavity signal does not show any orderliness as the modes are hopping too often.

light into a polarisation maintaining fibre guiding it to the experimental area on the MOT-table.

### 4.2.3 Ionisation Laser

In order to instantaneously photoionise  $^{87}\text{Rb}$  from the  $|5^2P_{3/2}, F' = 3\rangle$  state, we need a laser at a wavelength up to 479 nm (see fig. 2.6) and sufficient output power (350 mW). In this wavelength regime only a few commercial laser systems are available with an output power of 350 mW (all diode-pumped frequency-doubled solid state lasers). The first laser (manufactured by Shanghai Dream Lasers<sup>7</sup>) had severe defects. On the one hand, the pump light at a wavelength of 956 nm was not filtered out. There was still 30mW infra-red light in the output beam. On the other hand the specified TEM<sub>00</sub> mode could not be observed. Typically, two spatially separated intensity peaks occurred.

<sup>7</sup>[www.dreamlasers.com](http://www.dreamlasers.com)

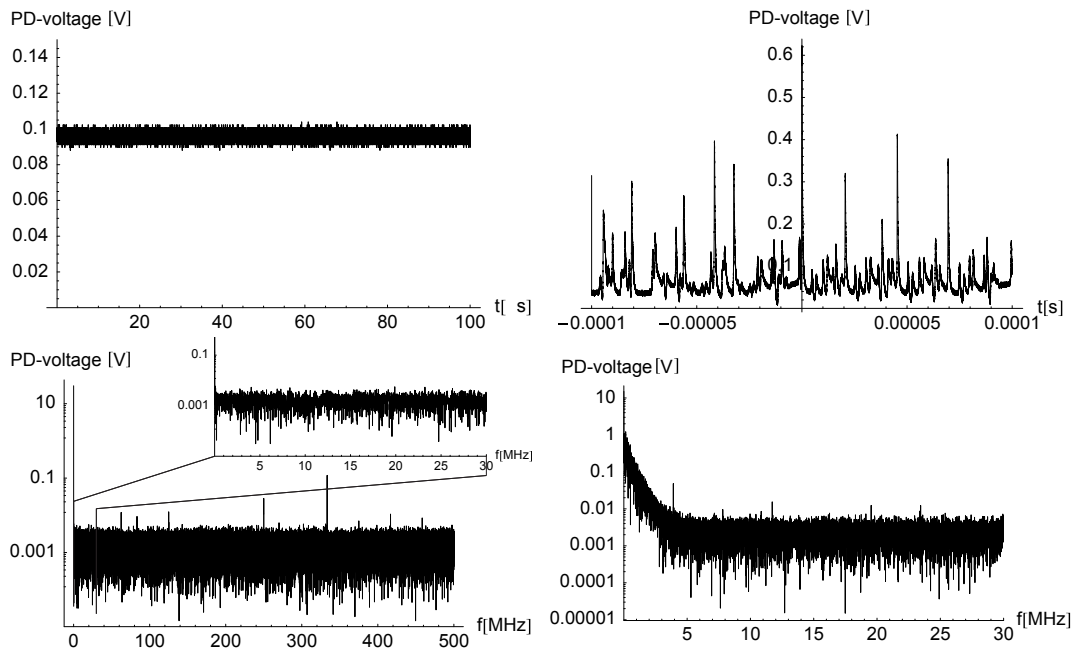


Figure 4.10: Comparison of the Laser Quantum laser system (left column) and the Shanghai Dream Laser system (right column):

The upper row shows the power fluctuations measured with a photo diode (PD) as a function of time. In the left graph mainly a flat line i.e. a stable intensity occurs whereas in the right graph high peaks occur followed by an exponential-decay like shape. The largest peak of the graph is approximately 10 times higher than the average of the signal. In the lower row, the respective power spectrum is shown. The Laser Quantum output power is sampled with a time resolution of 1 ns. According to the sampling theorem the highest resolvable frequency is 500 MHz. The power spectrum is flat from 10 kHz up to 500 MHz. Only 6 noise spikes at 50, 120, 280, 330 and 450 MHz can be identified. In contrast to that, the power spectrum of the Shanghai Dream laser system is completely different. The power spectral density between 2.5 kHz and 5 MHz is nearly proportional to the inverse of the frequency. This behaviour characterises so-called *pink noise* [53].

Moreover the main problem were the power and wavelength fluctuations (see fig. 4.9) due to the well known *spiking* behaviour [54]. Despite several exchanges of the complete laser system by the producing company they were still not able to supply a laser system satisfying their own specifications. Therefore we tested a second laser manufactured by Laser Quantum<sup>8</sup>. The spatial mode is a single TEM<sub>00</sub> mode and both, the time resolved signal and the cavity signal are stable on a short time scale (see 4.9 and 4.10). As the spatial mode is constant now, the coupling into a single mode fibre is significantly more efficient. We compared the two laser systems by measuring power fluctuations up to 1 GHz with a fast photo diode. The power spectrum of the Shanghai Dream laser shows pink noise in a range from 2.5 kHz up to 5 MHz (see fig. 4.10). In comparison with the Laser Quantum system there is neglectable noise up to a range of 500 MHz.

### 4.3 Magneto-optical trap

In this section all the steps are described that are necessary to assemble the MOT adapted to our experimental needs as cold atoms in the magneto-optical trap are the basic reservoir for loading the optical dipole trap with a single atom.

#### 4.3.1 Optics

The retro-reflecting magneto-optical trap consists basically of three incident beams that are backreflected into themselves (see 4.1) and an applied, external magnetic quadrupole field. To ensure equal intensities of the incident as well as of the retro-reflected beams the laser beams have to be focused down slightly (see fig. 4.11). This arises from non-neglectable reflection losses at the uncoated surfaces of the glass cell as the retro-reflecting beams pass them several times.

As described in section 2.5.1 we need circular polarised light at the centre of the MOT. For the horizontal beams not only the reflection losses on surfaces have to be considered but also the dependence of these losses on the polarisation of the light.

---

<sup>8</sup>[www.laserquantum.com](http://www.laserquantum.com)

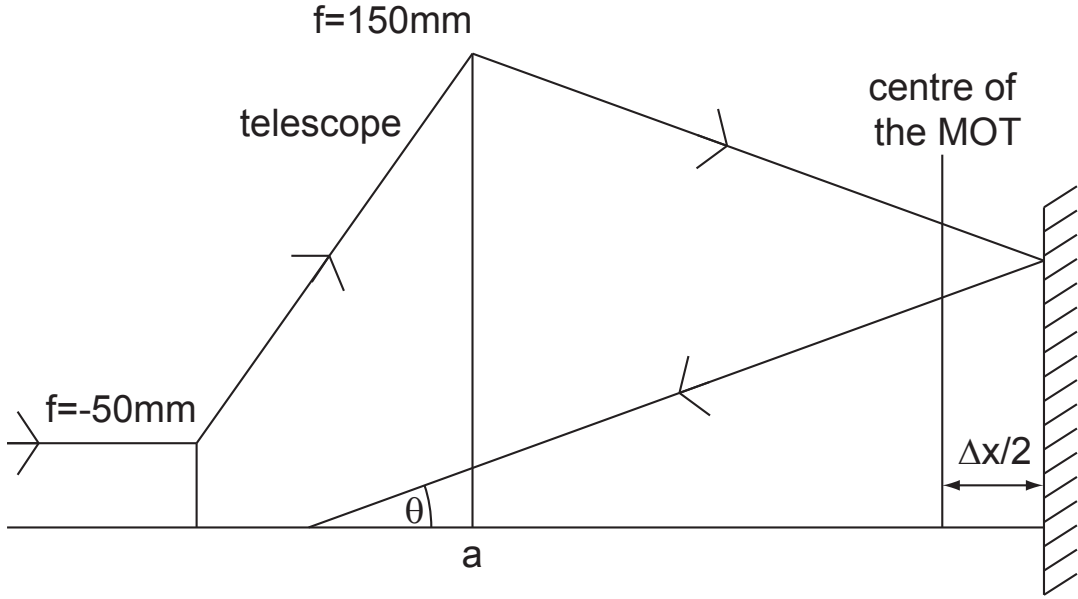


Figure 4.11: Sketch of the Galilean telescope: The telescope remains at the position  $a$  relative to the MOT.  $\Delta x$  is the distance the light travels to the retro mirrors and back to the centre of the MOT. For the vertical beam we measure  $\Delta x = 300\text{mm}$ , so the focus of the telescope is calculated to be at a distance  $f = 2.88\text{m}$  apart from the telescope.

The transmission coefficient for p and s polarised light<sup>9</sup> are  $T_p \approx 1$  and  $T_s = 0.86$ . In this way we can write:

$$\begin{aligned}
 E_{in} &= T_p^2 E_p + iT_s^2 E_s \\
 E_{out} &= iT_p T_s^3 E_p + T_s T_s^3 E_s \\
 &= T_p T_s (iT_s^2 E_p + T_p^2 E_s)
 \end{aligned}$$

<sup>9</sup>Light is p polarised when the plan of the incident, the reflected and transmitted beams are parallel to the polarisation of the incident light.

and the intensities are

$$\begin{aligned} I_{in} &= T_p^4 + T_s^4 \\ I_{out} &= T_p^2 T_s^2 (T_p^4 + T_s^4) = T_p^2 T_s^2 I_{in}. \end{aligned}$$

Accordingly, we see that we have to adjust  $I_{out} = 0.86^2 I_{in}$  to balance the intensities of the counterpropagating beams.

Similar considerations have to be done for the vertical beam. This time, the intensity losses do not depend on the polarisations as all the beams are perpendicular to the surfaces and the intensities. For the vertical beam we get

$$I_{out} = 0.96^4 I_{in} = 0.78 I_{in}.$$

The control of the focus is realised with a Galilean telescope shown in fig. 4.11

### 4.3.2 Quadrupole coils

The magnetic quadrupole field of the magneto-optical trap is generated by two coils in anti-Helmholtz configuration. Each coil consists of 121 windings, so we can produce the required magnetic field gradient with moderate currents of 4 ampere at maximum. In this manner we are able to operate the coils air cooled, reaching a field gradient of  $\frac{\partial \vec{B}}{\partial z} = 21 \frac{G}{cm}$  at 3A. The temperature of the coils reaches up to 55 °C at the surface if a current of 3 A is applied. As the wire used for the coils withstands temperatures up to 150 °C there is no danger in destroying the coils even if we operate the magneto-optical trap at higher field gradients corresponding to a current of 4 A.

The coils are mounted on a three dimensional translation stage. Therefore, the centre of the magnetic field can be manually adjusted to the intersection of the counterpropagating beams of the MOT. To compensate various unwanted magnetic stray fields, three pairs of coils in Helmholtz configuration are set up around the experimental area.

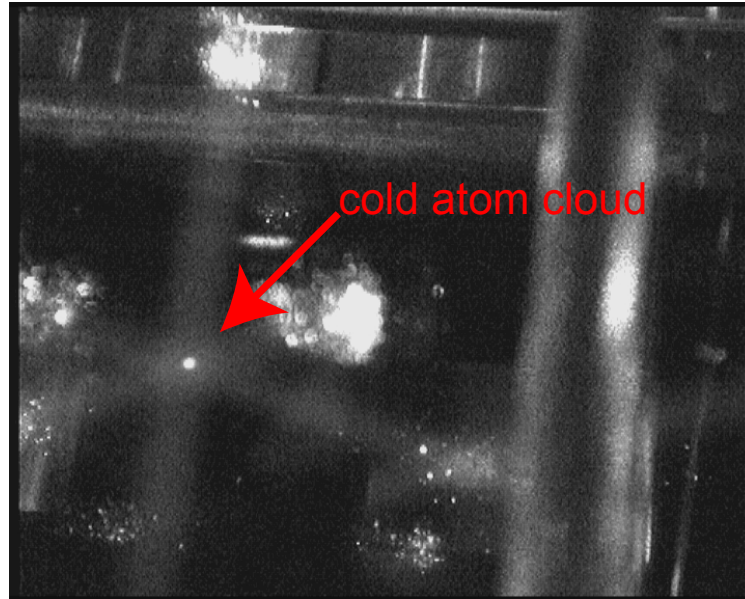


Figure 4.12: The cloud of cold  $^{87}\text{Rb}$  atoms inside the magneto-optical trap. The image is taken with an infra-red camera.

## 4.4 Determination of the atom number

To observe a cloud of cold atoms as shown in 4.12 we used the following parameters.

- Current of the quadrupole coils:  $I_{coils} = 3 \text{ A}$
- Current of the SAES dispenser:  $I_{dispenser} = 6 \text{ A}$
- Pressure in the UHV chamber:  $p = 2.1 \cdot 10^{-8} \text{ mbar}$
- Detuning of the cooling laser  $\Delta = -12 \text{ MHz}$
- Intensity of the all six cooling beams  $65 \text{ mW/cm}^2$
- Intensity of the repump light  $0.7 \text{ mW/cm}^2$

To characterise the magneto-optical trap more precisely with these parameters we have measured the number of trapped atoms. For this purpose, we collect the fluorescence light scattered by these atoms. Each atom scatters  $1.7 \cdot 10^7$  photons per

second isotropically as  $s_0 = \frac{I}{I_s} = 19$  [21] with  $I_s = 3.4 \text{ mW/cm}^2$ .

We want to collect the scattered light with an achromatic lens into a multi-mode fibre. The fibre has a diameter of  $50 \mu\text{m}$ . The coupling lens is adjusted such that the focus is in the origin of the cloud at a distance of 90 mm. With this configuration a region of the magneto-optical trap with 0.36 mm diameter is mapped onto the  $50 \mu\text{m}$  diameter of the fibre core. The estimated diameter of the cloud is 1 mm so we collect only the light of the atoms in a cylinder of 0.36 mm diameter and a height of 1 mm. The numerical aperture of the achromatic lens is 0.040. The collected light is guided to an Avalanche Photo Diode (APD) operated in Geiger-mode. The detection efficiency of the APD is assumed to be 10%. To make sure that only atomic fluorescence light is detected we insert interference filters in front of the APD. To assure that the APD is working linearly we insert a neutral density filter with an optical density of 3.0, i.e only one out of thousand photons is transmitted.

If we consider the geometry of the setup (see fig. 4.13), the losses and the detection efficiency, the probability to detect one scattered photon is  $3.9 \cdot 10^{-8}$ .

To determine the number of trapped atoms we record the counts of the APD as the magneto-optical trap is switched on. This is done for various currents. The temporal behaviour of the atom number during the loading stage is shown in fig. 4.14. We performed this procedure for three magnetic field gradients.

For a magnetic field gradient of  $\frac{\partial \vec{B}}{\partial z} = 21 \frac{\text{G}}{\text{cm}}$  for a current  $I_{\text{coils}} = 3 \text{ A}$ . With this current we can trap 29000 atoms in the entire MOT cloud. The number of atoms decreases to 23000 for  $\frac{\partial \vec{B}}{\partial z} = 14 \frac{\text{G}}{\text{cm}}$  (2 A), and 15000  $\frac{\partial \vec{B}}{\partial z} = 7 \frac{\text{G}}{\text{cm}}$  for 1 A.

These results show that the magneto-optical trap is sufficiently dense so we can load the optical dipole trap in an adequate time.

## 4.5 Optical dipole trap

The next step in the experiment is to set up a confocal microscope with which we can focus down the dipole laser beam to generate the dipole potential (shown in fig. 2.12), the ionisation beam for the state selective ionisation and collect at the same time the fluorescence light of the trapped atom. For this purpose we use a

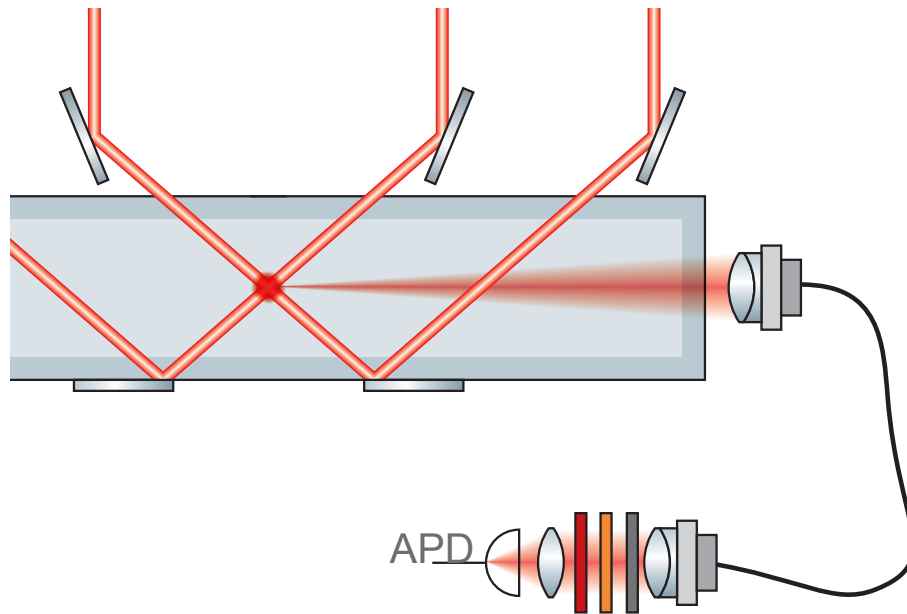


Figure 4.13: Setup to measure the atom number inside the MOT. The fluorescence light of the trapped atoms is collected by a lens coupled into a multi mode fibre at a distance of 90mm and guided to an APD operated in Geiger-mode. The numerical aperture of the system is 0.040 and with an efficiency of the APD of 0.1 we get the atom numbers shown in fig. 4.14 with an overall detection efficiency of  $3.9 \cdot 10^{-8}$  per scattered photon.

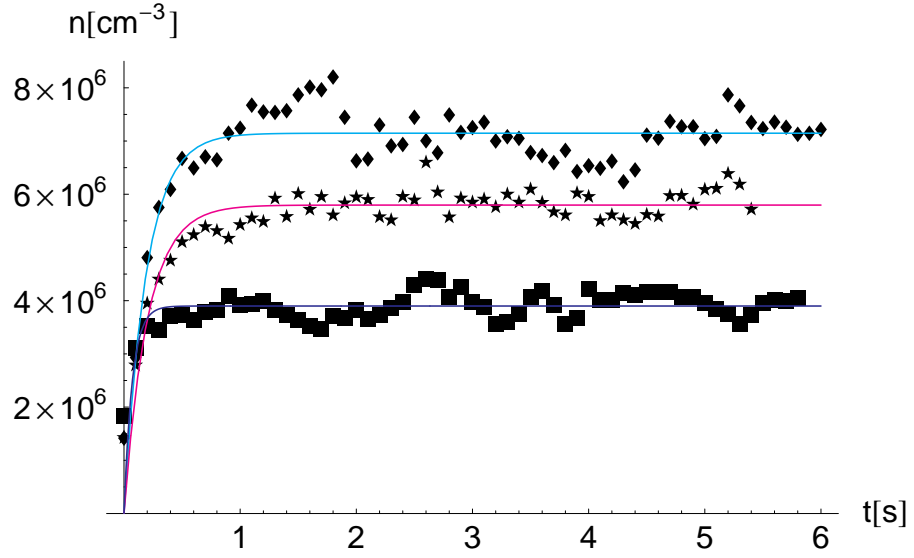


Figure 4.14: Loading of the MOT. The density of trapped atoms  $n$  inside the magneto-optical trap for three different currents of the quadrupole coils ( $\frac{\partial \vec{E}}{\partial z} = 21 \frac{G}{cm}$ ,  $\frac{\partial \vec{E}}{\partial z} = 14 \frac{G}{cm}$ ,  $\frac{\partial \vec{E}}{\partial z} = 7 \frac{G}{cm}$ ) reaches an equilibrium after 0.7 s. The background pressure was  $p = 2.1 \cdot 10^{-8}$  mbar and the SAES dispenser was operated at a current of  $I_{dispenser} = 6$  A.

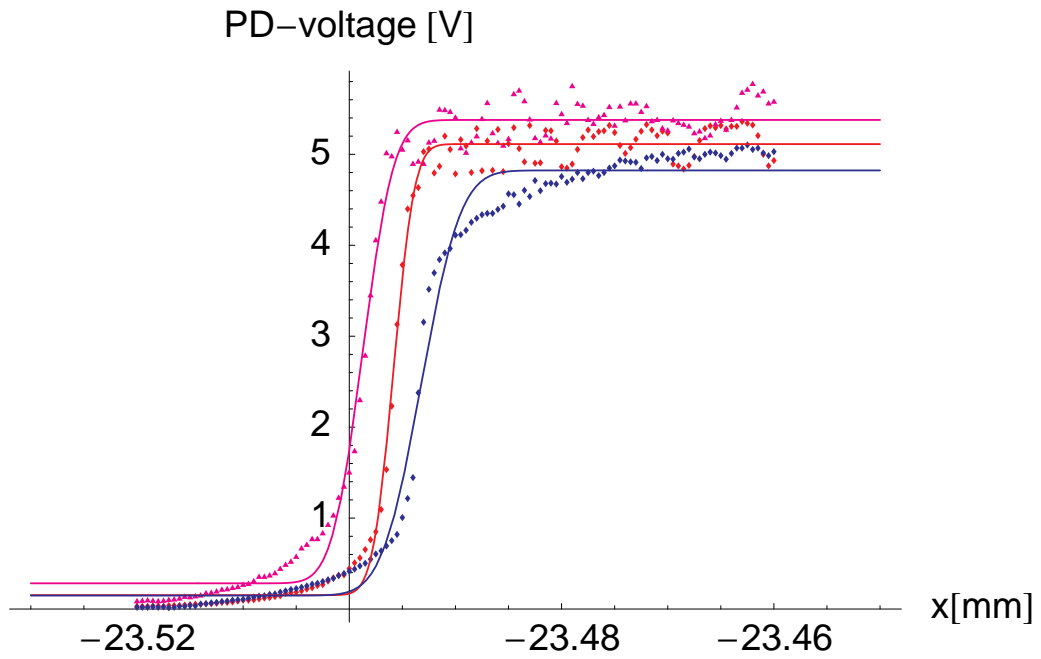


Figure 4.15: Recorded intensities depending on the x-position of the razor blade in the focus, for 780 nm, 850 nm and 473 nm. The solid line shows a fit of the data on eq. 4.3. One can see that our estimation of a  $\text{TEM}_{00}$  mode is wrong and we have to consider higher modes. This is seen from the plateaus that occur outside the focus area.

## 4 Experimental setup

---

wavelength	$z_0$	$W_0$	$M^2$	NA
780 nm	0.027 mm	1.99 $\mu\text{m}$	1.313	0.417
850 nm	0.023 mm	2.18 $\mu\text{m}$	1.415	0.477
473 nm	0.025 mm	2.28 $\mu\text{m}$	2.124	0.561

Table 4.1: Characterisation of the confocal microscope

commercial microscope objective<sup>10</sup> with a numerical aperture of 0.6 and a working distance of 13 mm. The schematic setup is shown in fig. 4.1.

In and outcoupled light is guided from and to the confocal microscope with optical fibres. For proper coupling aspheric lenses are used. Dichroic mirrors are used to overlap the different beams before they reach the objective. Both dichroic mirrors transmit fluorescence light independent of its polarisation.

Due to chromatic aberration of the microscope objective the (longitudinal)  $z$ -position of the foci differ for each wavelength. To compensate the chromatic aberration we slightly change the divergence angles of the incoming nearly collimated beams using precise translation mounts for the achromatic lenses collimating the beams.

To measure the exact position of the focus we set up a 1:1 telescope with an identical objective. To simulate the glass cell of the vacuum we put an optical window in front of the focusing objective. In the focus of the telescope we assemble two step motors with a minimum step width of 500 nm. These stepper motors move a razor blade through the focus. We record the transmitted intensity of each wavelength with a photo diode (PD) and the result is shown in fig. 4.15.

Assuming a TEM<sub>00</sub> mode in the focus we get the intensity function

$$I(x) = I_0 \int_{-\infty}^x \int_{-\infty}^{\infty} e^{-\frac{2(x^2+y^2)}{w_0^2(z)}} = y_0 + y_1 \operatorname{erf} \left( \sqrt{\frac{x-x_0}{w_0^2}} \right). \quad (4.3)$$

We fit the values for  $w_0$  and  $x_0$  and their errors, whereas  $y_0$  and  $y_1$  describe the background and the intensity of the used laser light, respectively. A characteristic plot of the recorded data in the foci is given in fig. 4.15.

---

<sup>10</sup>Thales Optem High Resolution 20x

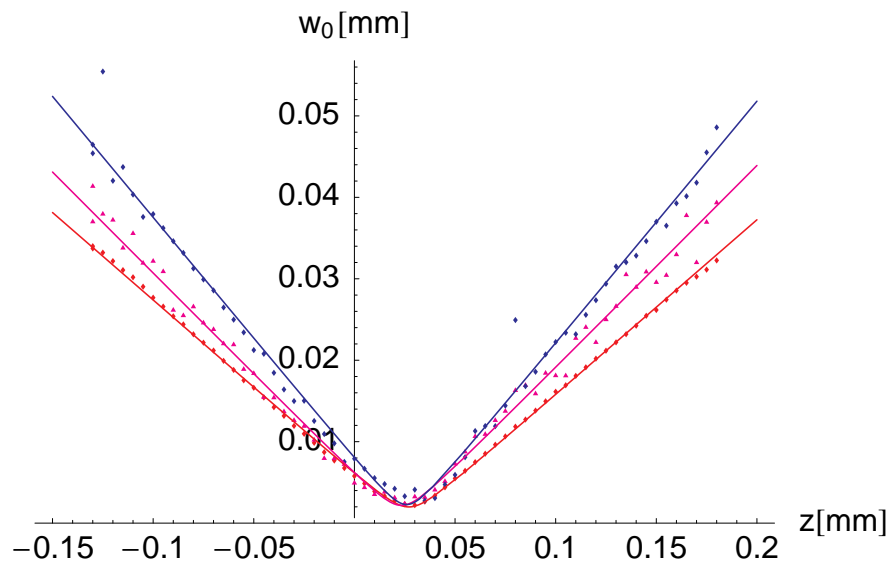


Figure 4.16: Results of the waist scan for every single beam, i.e. **780 nm**, **850 nm** and **473 nm**. The step size in  $z$ -direction is  $0.5 \mu\text{m}$ . The straight lines are numerical least-square fits to the function 4.5. The calculated values are given in tab. 4.1.

In this plot one can see that the measured profiles do not correspond to a perfect TEM<sub>00</sub> mode as plateaus arise in the areas outside the foci.

To further characterise now the quality of an optical system one can use the concept of  $M^2$  [55]. In contrast to an idealised Gaussian beam every real beam consists not only of a TEM<sub>00</sub> mode but also of higher modes and therefore the beam is  $M$  times larger than a Gaussian beam ( $M = 1$ ) everywhere. Hence we can say<sup>11</sup> that

$$w_0 = \frac{W_0}{M}. \quad (4.4)$$

The beams propagate in the  $z$ -direction and the waists  $W(z)$  are

$$W(z) = 2W_0 \sqrt{1 + \frac{(z - z_0)^2}{z_R^2}}. \quad (4.5)$$

where the Rayleigh length  $z_R$  is given by

$$z_R = \frac{\pi w_0^2}{\lambda} = \frac{\pi W_0^2}{M^2 \lambda} \quad (4.6)$$

Here  $\lambda$  is the wavelength of the considered light beam.

The numerical aperture of the objective is given by

$$NA = \sin \theta = \frac{4\lambda}{\pi} \frac{M^2}{2W_0} \quad (4.7)$$

and for each beam the results are given in 4.1. The detection efficiency of the objective for the fluorescence light is therefore estimated to be 3.3%.

### 4.5.1 Experimental results

To load the optical dipole trap, the cooling and repump light are turned on and the dipole trap beam provides the potential needed to trap a single atom. The quadrupole coils are operated at a current of 3A to generate a field gradient of 21 G/cm. In this way we ensure that the trap is loaded with a sufficiently high loading rate.

---

<sup>11</sup>We use the convention that uppercase quantities refer to real beam while lowercase letters refer to an idealised Gaussian beam.

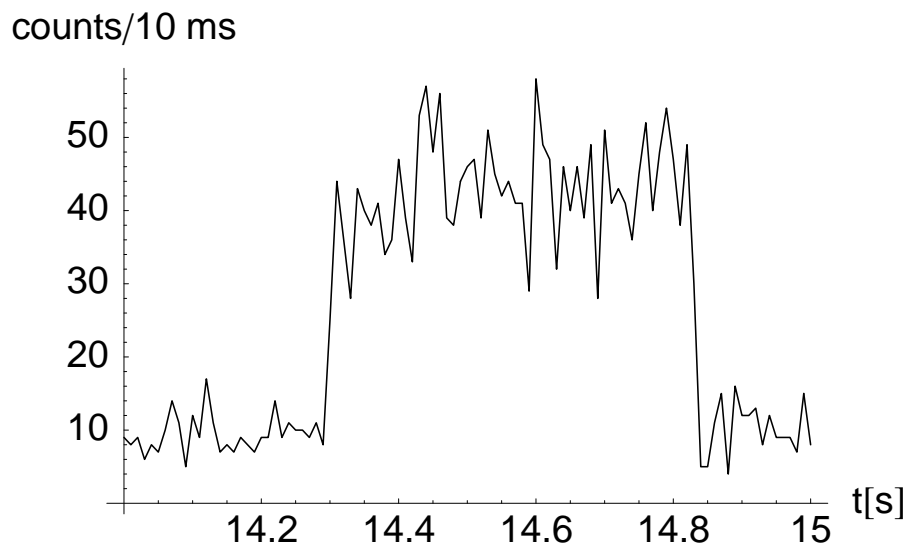


Figure 4.17: Time resolved behaviour of the fluorescence counts out of the trap region. In case there is no atom inside the trap, the count rate is  $1000 \text{ s}^{-1}$ , whereas the count rate increases to  $4000 \text{ s}^{-1}$  when a single atom inside the trap is present.

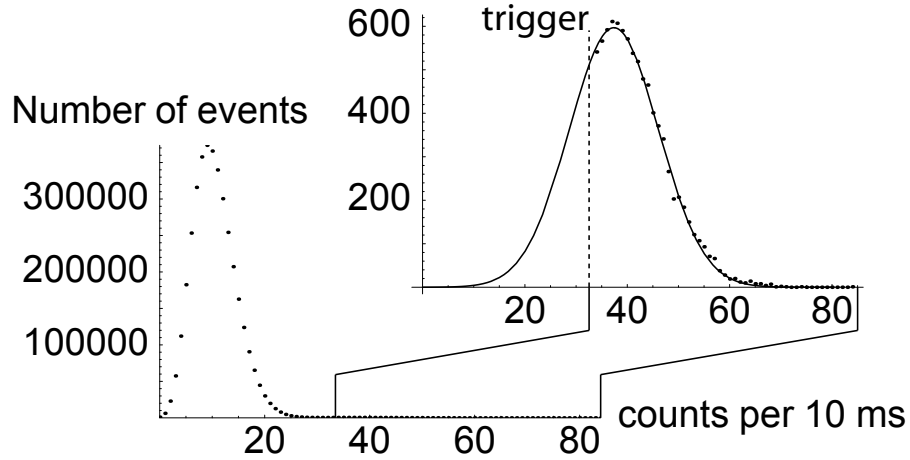


Figure 4.18: Histogram of the fluorescence counts per 10 ms for a total measurement time of 10.4 h. The first peak around a countrate of 10 per 10 ms corresponds to the count rate caused by stray light and dark counts of the APD [15]. The second is caused by a single atom inside the trap. In the inlet, a magnification of the second peak and a Gaussian fit on the count rate are shown. The trigger to distinguish the two cases of “one atom” and “zero atom” is set to 33 counts per 10 ms, therefore there are no data points below 33 in the inlet.

The scattered photons are collected with the microscope objective and coupled into a single mode optical fibre and guided to a avalanche photo diode (APD). In the case that a single atom is present we see an increase of the fluorescence light recorded by the APD. The time-resolved signal of the APD is shown in fig. 4.17. The background signal is 1000 counts/s whereas with an atom inside the dipole trap, the countrate increases to 4000 counts/s. Hence we collect additional 3000 photons per second from the atom.

By histogramming the count rate over a measurement time of 10.4 h we get two distinct peaks. The first peak is caused by the dark count rate of the APD module and by resonant stray light inside the vacuum chamber. The second peak occurs due

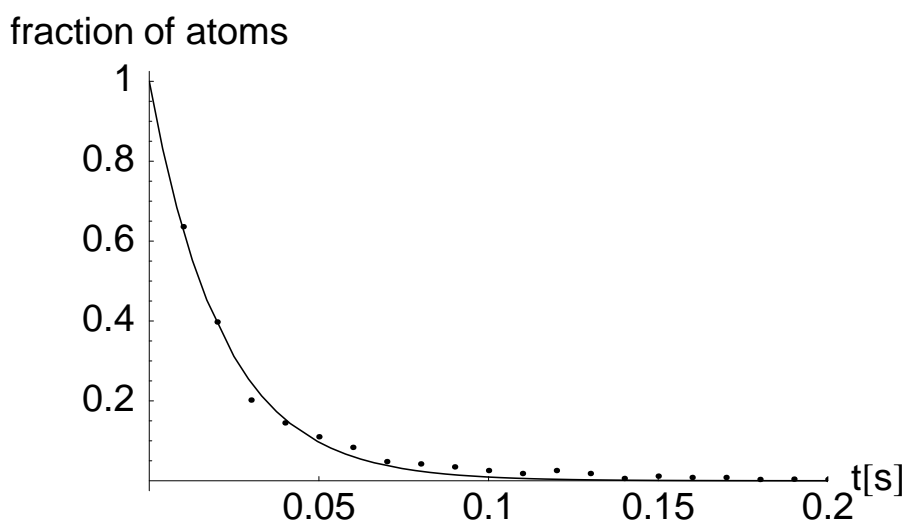


Figure 4.19: The lifetime of the atom in the trap is mainly limited by collisions with the hot background gas. In this measurement the pressure was  $\approx 1.2 \cdot 10^{-8}$  mbar which corresponds to a 1/e-life time of  $\approx 20$  ms.

to the fluorescence light of the trapped single atom (See fig. 4.18). The nonexistence of a third peak around a count rate of 7000 counts per second indicates that there is only one atom in the trap [15, 16, 19, 50].

The life time of the atom inside the optical dipole trap is limited by collisions with hot background gas. As all the results shown in this chapter are preliminary and rather uncalibrated, rough measurements, the lifetime of the atom is only 20 ms (see fig. 4.19). Assumingly, this is mainly limited by collisions with atoms out of the hot background at the considerable high pressure of  $\approx 1.2 \cdot 10^{-8}$  mbar. The dark count rate is very high as the dispensers were turned off so there were very few atoms present. Therefore the event rate of a single atom is lower by a factor  $10^3$  as the dark count events.

**Summary** We assembled a magneto-optical trap that provides us with a reservoir of 29000 atoms at a magnetic field gradient of 21 G/cm. This is sufficient to load the optical dipole trap with a single atom. The dipole trap is loaded with only one atom

#### *4 Experimental setup*

---

whereas the life time of the atom in the trap has to be increased up to 1 s. Further calibrations and characterisations of the optical dipole trap have to be made, but we have shown that we have only a single atom inside the trap.

## 5 Summary and outlook

In this thesis, a possible loophole free test of Bell's inequality is proposed and first steps towards this goal are presented. For this experiment, it is essential to achieve an extensive control of two remote, single atoms, swap the entanglement between them and detect the state of the atom with high accuracy within 1  $\mu$ s.

In the framework of this thesis, the installation of a magneto-optical trap and a single atom optical dipole trap is realised as a first ingredient towards this test. In our current setup, the magneto-optical trap is fully aligned and characterised. The design is chosen to be very compact for enhanced optical access. It is operating stable and provides a sufficient reservoir of cold atoms for the optical dipole trap that is designed in a confocal microscope arrangement together with the detection optics for the fluorescence light as well as the ionisation beam. The trap beam, with respect to the D<sub>2</sub>-line of <sup>87</sup>Rb far red-detuned, is focused down to a waist of  $w_0 = 2.18 \mu\text{m}$  and provides a trap potential of 1 mK. The fluorescence beam collects the light corresponding to a focus of  $w_0 = 1.99 \mu\text{m}$ . This way, we see the scattered light of the trapped atom with a high efficiency of an accordant numerical aperture of 0.417. In a first run, the lifetime of the trapped atom inside the optical dipole trap exceeds 20 ms. For future enhanced operation cycles of the optical dipole trap, this has to be increased, e.g., by lowering the background pressure level significantly compared to the present one. The next steps in the experiment will be the installation of the optics for the atomic preparation. With this, we can prepare the trapped atom in the  $5^2P_{3/2}, F = 0$  state, the starting point for our  $\Lambda$  decay. Furtheron, the STIRAP laser system has to be implemented and the detection system for the ionisation fragments. Moreover, in a further step the Bell state analyser has to be set up. To close the locality as well as the detection loophole we want to ionise the atom

state-selectively. With the new ionisation laser system, the state-selective ionisation is possible within 120 ns with an efficiency of 99.9%. In order to achieve this, different laser systems had been tested and characterised according to their specifications and the intensity noise is suppressed up to a frequency of 500 MHz. Together with the detection of the ionisation fragments and the stimulated adiabatic Raman passage (STIRAP), the entire state detection of the atom will require approximately 400 ns [56].

The performance estimations of the state-selective ionisation shows that the locality loophole can be closed if the two atoms are separated by 300 m. The detection efficiency of the channel electron multipliers is estimated to 96.5 % for coincidence detecting the electron and the ion [57, 56], allowing us to close the detection loophole.

We can estimate the efficiency to detect the photon of the entangled atom-photon pair to be  $\eta_{ph} = 2.8\%$ . This also holds for two atom-photon pairs and we get the total probability for the generation of an atom-atom pair  $\eta_{atom-atom} = \frac{1}{4}\eta_{ph}^2 t_{fibre} = 1.4 \cdot 10^{-6}$ . The factor  $\frac{1}{4}$  arises due to the fact that we detect only the photonic state  $|\Psi^-\rangle$  out of the four Bell states 2.10 to 2.13 and  $t_{fibre}$  is the transmission probability of the fibre after a length of 300 m, i.e. 72 %. In the actual setup we can run the preparation cycles with a mean repetition rate of 40 kHz. In this way, we are able to generate one atom-atom pair within approximately 18 s. The visibility of the atom-photon entanglement is 0.86 [13, 16, 35, 58, 59]. If we consider the errors of the Bell state measurement and of the APD's we get a visibility of the atom-atom entanglement of 0.75 [56].

For these values, approximately 2000 atom pairs are required for the loophole-free test of Bell's inequality in the formulation of CHSH [60] for a violation by three standard deviations. From these estimations a loophole-free test should be feasible within 10 hours of total measurement time.

# A Appendix

## A.1 Addition of angular momenta

In the next step we want to connect two different Hilbert subspaces spanned by two angular momentum operators  $\mathcal{A}_1$  and  $\mathcal{A}_2$  with the properties

$$[\mathcal{A}_{1i}, \mathcal{A}_{1j}] = i\hbar\mathcal{A}_{1k} \quad (\text{A.1})$$

$$[\mathcal{A}_{2i}, \mathcal{A}_{2j}] = i\hbar\mathcal{A}_{2k} \quad (\text{A.2})$$

$$[\mathcal{A}_{1k}, \mathcal{A}_{2l}] = 0 \quad (\text{A.3})$$

We now define the new operator of total angular momentum

$$\mathcal{A} = \mathcal{A}_1 \otimes 1 + 1 \otimes \mathcal{A}_2 \quad (\text{A.4})$$

that we will write in a more common way as

$$\mathcal{A} = \mathcal{A}_1 + \mathcal{A}_2 \quad (\text{A.5})$$

that naturally fulfils the commutator relation  $[\mathcal{A}_i, \mathcal{A}_j] = i\hbar\epsilon_{ijk}\mathcal{A}_k$  and is therefore an angular momentum operator as well. The difference occurs as  $\mathcal{A}$  is the generator for the entire system and we have now two options for choosing our base kets:

The first option is to define our base kets as eigenkets of the operators  $\mathcal{A}_1^2$ ,  $\mathcal{A}_2^2$ ,  $\mathcal{A}_{1z}$  and  $\mathcal{A}_{2z}$  designated as  $|j_1j_2; m_1m_2\rangle$ . They commute with each other and we get the defining equations as

$$\mathcal{A}_1^2 |j_1j_2; m_1m_2\rangle = j_1(j_1 + 1)\hbar^2 |j_1j_2; m_1m_2\rangle \quad (\text{A.6})$$

$$\mathcal{A}_2^2 |j_1j_2; m_1m_2\rangle = j_2(j_2 + 1)\hbar^2 |j_1j_2; m_1m_2\rangle \quad (\text{A.7})$$

$$\mathcal{A}_{1z} |j_1j_2; m_1m_2\rangle = m_1\hbar |j_1j_2; m_1m_2\rangle \quad (\text{A.8})$$

$$\mathcal{A}_{2z} |j_1j_2; m_1m_2\rangle = m_2\hbar |j_1j_2; m_1m_2\rangle \quad (\text{A.9})$$

## A Appendix

---

The second option are the base kets as eigenkets of the operators  $\mathcal{A}^2$ ,  $\mathcal{A}_1^2$ ,  $\mathcal{A}_2^2$ ,  $\mathcal{A}_z$  and we denote the base ket as  $|j_1 j_2; jm\rangle$  and get

$$\mathcal{A}^2 |j_1 j_2; jm\rangle = j(j+1)\hbar^2 |j_1 j_2; jm\rangle \quad (\text{A.10})$$

$$\mathcal{A}_1^2 |j_1 j_2; jm\rangle = j_1(j_1+1)\hbar^2 |j_1 j_2; jm\rangle \quad (\text{A.11})$$

$$\mathcal{A}_2^2 |j_1 j_2; jm\rangle = j_2(j_2+1)\hbar^2 |j_1 j_2; jm\rangle \quad (\text{A.12})$$

$$\mathcal{A}_z^2 |j_1 j_2; jm\rangle = m\hbar |j_1 j_2; jm\rangle \quad (\text{A.13})$$

As  $\mathcal{A}^2$  does commute neither with  $\mathcal{A}_{1z}$  nor  $\mathcal{A}_{2z}$  we can't add it to the set of operators of our first option, nor vice versa, so we're left with two bases of mutually compatible observables.

The next step now will be to connect the two bases and we'll end up with the Clebsch-Gordan-coefficients.

$$|j_1 j_2; jm\rangle = \sum_{m_1} \sum_{m_2} |j_1 j_2; m_1 m_2\rangle \langle j_1 j_2; m_1 m_2 | j_1 j_2; jm\rangle \quad (\text{A.14})$$

with  $\sum_{m_1} \sum_{m_2} |j_1 j_2; m_1 m_2\rangle \langle j_1 j_2; m_1 m_2| = 1$  for given  $j_1$  and  $j_2$ . The elements of this unitary transformation matrix  $\langle j_1 j_2; m_1 m_2 | j_1 j_2; jm\rangle$  are the Clebsch-Gordan-coefficients with the properties

- $m = m_1 + m_2$
- $|j_1 - j_2| \leq j \leq j_1 + j_2$
- $\langle j_1 j_2; m_1 m_2 | j_1 j_2; jm\rangle = \langle j_1 j_2; jm | j_1 j_2; m_1 m_2\rangle$
- $\sum_j \sum_m \langle j_1 j_2; m_1 m_2 | j_1 j_2; jm\rangle \langle j_1 j_2; m'_1 m'_2 | j_1 j_2; jm\rangle = \delta_{m_1 m'_1} \delta_{m_2 m'_2}$
- $\sum_{m_1} \sum_{m_2} \langle j_1 j_2; m_1 m_2 | j_1 j_2; jm\rangle \langle j_1 j_2; m'_1 m'_2 | j_1 j_2; j' m'\rangle = \delta_{jj'} \delta_{mm'}$

Sometimes they are also written in terms of Wigner's 3-j symbol

$$\langle j_1 j_2; m_1 m_2 | j_1 j_2; jm\rangle = (-1)^{j_1 - j_2 + m} \sqrt{2j+1} \begin{pmatrix} j_1 & j_2 & j \\ m_1 & m_2 & m \end{pmatrix} \quad (\text{A.15})$$

and for our purpose we can find them all in the literature i.e. [61]

## A.2 Spontaneous decay as a source of entanglement

In our experiment we want to use the spontaneous decay of a single  $^{87}\text{Rb}$  atom as an EPR source. In this way we can get entanglement between different species, i.e. an atom and a photon because of the conservation of angular momentum. Using two different species we can get an interface between quantum memories (atom) and quantum communication (photon). In this section I will describe the theory of spontaneous decay and will introduce our decay channels as the source of the EPR pairs.

### A.2.1 Spontaneous decay in a two-level system

#### A.2.1.1 Interaction Hamiltonian

The Hamiltonian of an atom interacting with a radiation field can be described by a Hamiltonian separated into three parts

$$\mathcal{H} = \mathcal{H}_A + \mathcal{H}_R + \mathcal{H}_{ED} \quad (\text{A.16})$$

where  $\mathcal{H}_A$  are  $\mathcal{H}_R$  the Hamiltonian of a two-level atom and the radiation field, respectively, and are given as

$$\mathcal{H}_A = \sum_i \hbar\omega_i |i\rangle \langle i| \quad (\text{A.17})$$

$$\mathcal{H}_R = \sum_{\lambda, \mathbf{k}} \hbar\omega_{\mathbf{k}} \left( \hat{a}_{\lambda, \mathbf{k}}^\dagger \hat{a}_{\lambda, \mathbf{k}} + \frac{1}{2} \right) \quad (\text{A.18})$$

with the atomic states  $|i\rangle$  and the radiative field creation and annihilation operators  $\hat{a}_{\lambda, \mathbf{k}}^\dagger$  and  $\hat{a}_{\lambda, \mathbf{k}}$ . The Hamiltonian for the interaction of the radiative field and the atom is

$$\mathcal{H}_{ED} = \mathcal{E}(\mathbf{r}, t) \cdot \mathbf{d} = e \cdot \iota \sum_{\lambda, \mathbf{k}} \sum_{i, j} g_{ij\lambda\mathbf{k}} e^{i(\omega_i - \omega_j)t} \left( \hat{a}_{\lambda, \mathbf{k}} e^{-i\omega_{\mathbf{k}}t} - \hat{a}_{\lambda, \mathbf{k}}^\dagger e^{i\omega_{\mathbf{k}}t} \right) |i\rangle \langle j| \quad (\text{A.19})$$

with the coupling coefficient

$$g_{ij\lambda\mathbf{k}} = \sqrt{\frac{\omega_{\mathbf{k}}t}{2\hbar\epsilon_0 V}} \hat{\mathbf{e}}_{\lambda\mathbf{k}} \langle i | \hat{\mathbf{d}} | j \rangle. \quad (\text{A.20})$$

## A Appendix

---

We can rearrange the terms of eq. A.19 such that  $\omega_j > \omega_i \quad \forall j > i$  and knowing that the dipole matrix elements  $\langle i | \hat{\mathbf{d}} | i \rangle$  vanish because of the fact that  $\hat{\mathbf{d}}$  has odd parity. We get:

$$\mathcal{H}_{ED} = i\hbar \sum_{\lambda\mathbf{k}} \sum_{j>i} \left( g_{ij\lambda\mathbf{k}} e^{i\omega_{ji}t} |j\rangle \langle i| + g_{ij\lambda\mathbf{k}}^* e^{-i\omega_{ji}t} |i\rangle \langle j| \right) \left( \hat{a}_{\lambda,\mathbf{k}} e^{-i\omega_{\mathbf{k}}t} - \hat{a}_{\lambda,\mathbf{k}}^\dagger e^{i\omega_{\mathbf{k}}t} \right) \quad (\text{A.21})$$

where  $\omega_{ji} = \omega_j - \omega_i$  are the atomic transition frequencies. In eq. A.21 there are four different terms. The term  $|j\rangle \langle i| \hat{a}_{\lambda,\mathbf{k}}$  describes the excitation of the atom while absorbing (annihilating) a photon. On the other hand  $|i\rangle \langle j| \hat{a}_{\lambda,\mathbf{k}}^\dagger$  describes a decay process of the excited atom. The other two terms would violate the conservation of energy and therefore are neglected. This approximation is called rotation-wave approximation (RWA) [21] and with  $\Delta\omega_{ijk} = \omega_{ij} - \omega_{\mathbf{k}}$  the detuning of the light relatively to the atomic transition and the Hamiltonian is finally

$$\mathcal{H}_{ED} = i\hbar \sum_{\lambda\mathbf{k}} \sum_{j>i} \left( g_{ij\lambda\mathbf{k}} |j\rangle \langle i| \hat{a}_{\lambda\mathbf{k}} e^{-i\Delta\omega_{ijk}t} - g_{ij\lambda\mathbf{k}}^* |i\rangle \langle j| \hat{a}_{\lambda\mathbf{k}}^\dagger e^{i\Delta\omega_{ijk}t} \right) \quad (\text{A.22})$$

### A.2.1.2 Atom in a radiative field

The two-level atom interacting with the radiative field can be described by a combined atom-field state rewriting eq. A.22

$$|\Psi\rangle = c_e(t) |e\rangle |0\rangle + \sum_{\lambda\mathbf{k}} c_{g,\lambda\mathbf{k}}(t) |g\rangle |1_{\lambda\mathbf{k}}\rangle. \quad (\text{A.23})$$

where  $c_e(t)$  is the time dependent amplitude of the excited state and  $c_{g,\lambda\mathbf{k}}(t)$  the amplitude of the combined atom-photon in the mode  $\lambda\mathbf{k}$  state. Here we see the crucial step that the atom (state  $|e\rangle |0\rangle$ ) is entangled with the radiative field ( $|g\rangle |1_{\lambda\mathbf{k}}\rangle$ ), respectively.

### A.2.1.3 Polarisation modes

Until now we just talked about an idealised two level system, but now we consider a real atom with multiple decay channels that lead to different atomic ground states, whereas in the decay the photon can carry away some angular momentum. In detail I

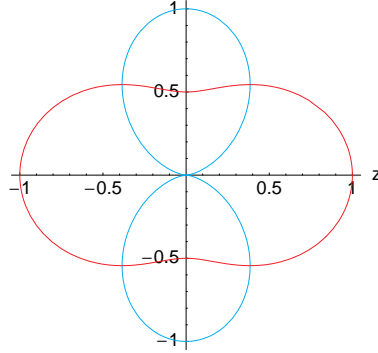


Figure A.1: The emission characteristics of  $\pi^-$  (cyan) and  $\sigma^{\pm}$ - (magenta) polarised light. The polarisation axis is along the  $z$ -axis.  $\theta$  is the off-axis angle. Our detection optics is in the same direction, hence we can not detect  $\pi$  polarised light.

will explain the properties of angular momentum in section 2.3. Until now we define a quantisation axis for our system and we can decompose the angular momentum degrees of freedom of the atom and the photon into eigenstates of this system. As the main focus of this work is on the state detection of the atom I will keep this part rather short [13, 15, 16].

$m$  defines the projection of the photonic spin on the quantisation axis and in this way we get the three basis states for the emitted photon

$$|m = +1\rangle = |\sigma^+\rangle \quad (\text{A.24})$$

$$|m = 0\rangle = |\pi\rangle \quad (\text{A.25})$$

$$|m = -1\rangle = |\sigma^-\rangle, \quad (\text{A.26})$$

where  $|\sigma^+\rangle(|\sigma^-\rangle)$  are left(right) circularly and  $|\pi\rangle$  linearly i.e. parallel to the quantisation axis polarised light. The emission characteristics of dipole radiation leads to different emission probabilities in space depending on the angle relative to the

polarisation axis (see fig. A.1) and we get for the three polarisations [62]

$$|\Sigma^\pm\rangle = \sqrt{\frac{3}{16\pi}}(1 + \cos^2\theta \cdot |\sigma^\pm\rangle) \otimes \sum_{\theta,\omega} g_\omega |\theta,\omega\rangle \quad (\text{A.27})$$

$$|\Pi\rangle = \sqrt{\frac{3}{8\pi}} \sin\theta \cdot |\pi\rangle \otimes \sum_{\theta,\omega} g_\omega |\theta,\omega\rangle. \quad (\text{A.28})$$

Because of the dependence on the emission angles of these distributions we do not detect any  $|\pi\rangle$  photons as they are not emitted along the quantisation axis, in contrast to the  $|\sigma^\pm\rangle$  that have a maximum in this direction.

### A.3 The mobile lab

To close the locality loophole the distances between the two entangled atoms has to be bigger than the time we need to measure times the speed of light

$$x_1 - x_2 \geq c\tau_{meas}. \quad (\text{A.29})$$

To realise this we have to be able to move our experiment to other buildings after its initial installation in rooms of the physics department. Therefore we took care of

- using only mobile shelves
- reducing the number of different cable tracks
- centralise the power supply when possible

The first item was done by our workshop. They built two carriers on wheels where the optical tables are put. The entire carrier is made of non-magnetic stainless steel. The damping is done by six small bicycle tires between the carrier and the bread-board.

When the entire experiment is ready we have to move and we have to pass the spatial bottle neck of the elevator. This elevator can carry only one of the two experimental tables not mentioning all the electronics, so we have disconnect all power supply cables and data cables in an organised way. For the power supply we installed a split box that divides a three phase current into three normal 230V connectors. With one

---

Voltage	max. Currenncy	max. Power
+5V	10A	50W
-5V	10A	50W
+15V	10A	150W
-15V	10A	150W
+24V	20A	480W

Table A.1: Characteristics of the central power supply installed in the electronics cabinet

of these split boxes on each table we can supply each table with max.  $11kW$  and we have only one cable to disconnect.

Most of the data cables are ordinary BNC connected  $50\Omega$  cables. We arranged them in a bus system of ten cables each bus. This bus system is easily extendable and the mobility is guaranteed as we do not have to disconnect every wire coming from various components. We just have to unplug the single buses going from the table to the electronics cabinet.

This electronics cabinets will gather all the electronics controlling our experiments and again, they are on wheels. Only the electronics for the laser systems is placed on the table itself, all other devices are installed into these cabinets. The first cabinet related to the experiment until now has a central power supply and there are only entire cable buses between the single components (tables, cabinets). This design of the experimental setup leads to some temperature problems, as we installed all the amplifiers of acousto-optical modulators (AOM's) in the cabinet. They are very sensible to over heating and therefore we installed four ventilators each with a conveyance-mass of  $\approx 100m^3/h$ , two blowing into the amplifier section, two out of it. Because of the generation of noise, we decided to let always two of them run in a series connexion. We installed the same ventilator array at the central power supply that provides all the electronics with the maximum output currencies described in tab. A.1

## A.4 Laser system

The following figures give an overview about the design of the optical table and the frequencies chosen by the AOM's.

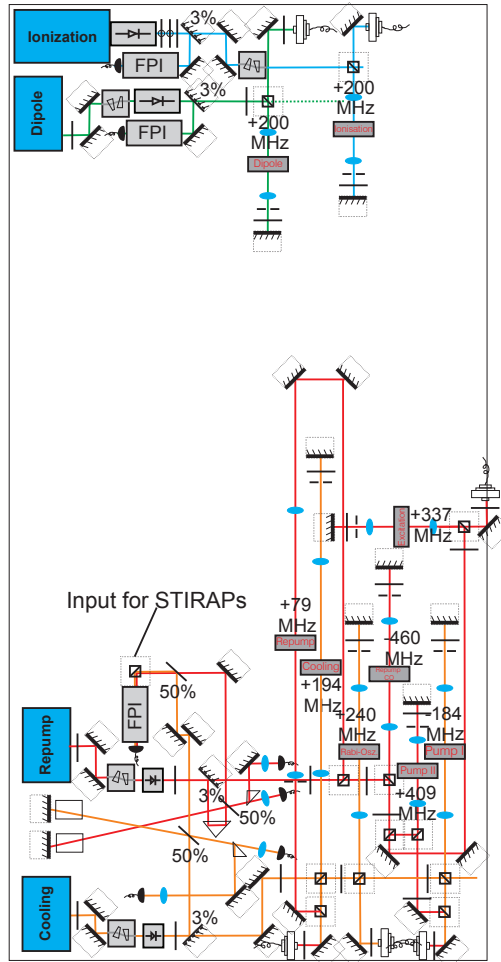


Figure A.2: Sketch of the optical table:

To save space on the table a sketch of all laser systems and AOM lines is made. In this way we can find out the optimal arrangement of all components.

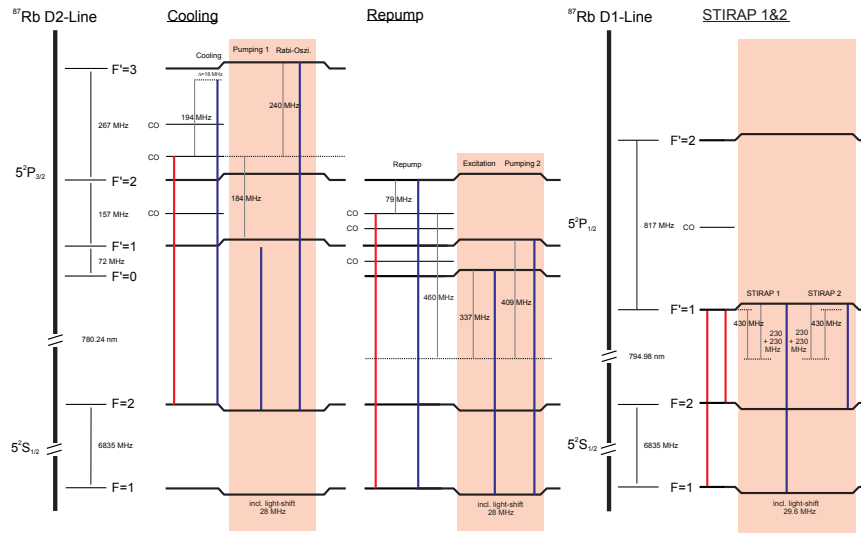


Figure A.3: Diagram of the laser frequencies:

This graph shows the relative frequencies to various transitions depending on the laser lock.

## A.5 Power stabilisation

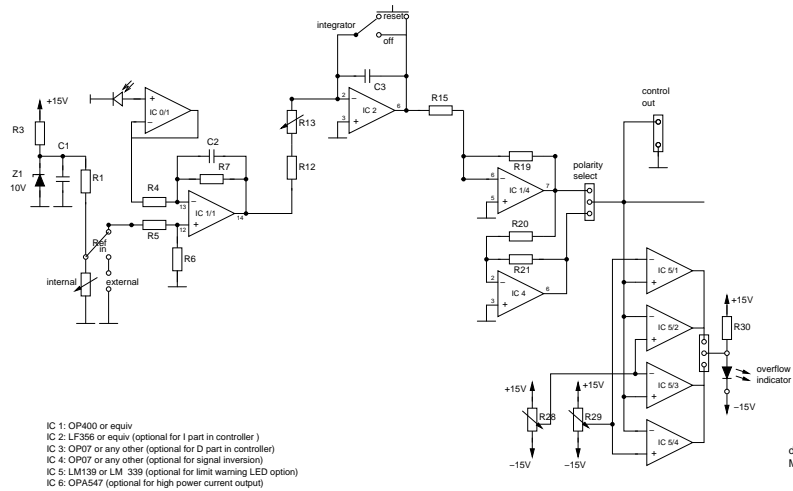


Figure A.4: Circuit diagram of the intensity stabilisation. This electronic device is used to stabilise the cooling, repump and the dipole trap laser.

## **A.6 Photos of the setup**

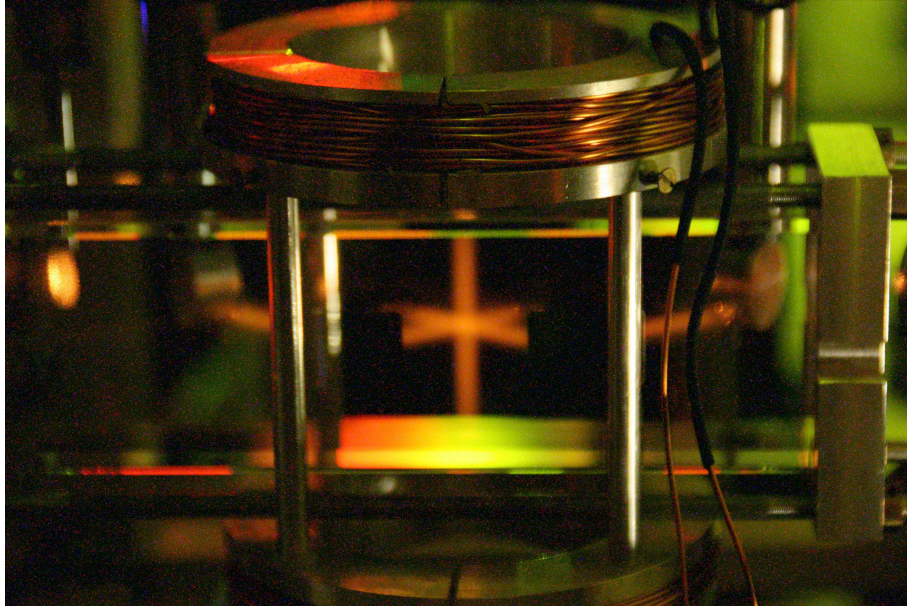


Figure A.5: Long term exposure (10 min) image of the vacuum chamber with a high  $^{87}\text{Rb}$  vapour pressure.

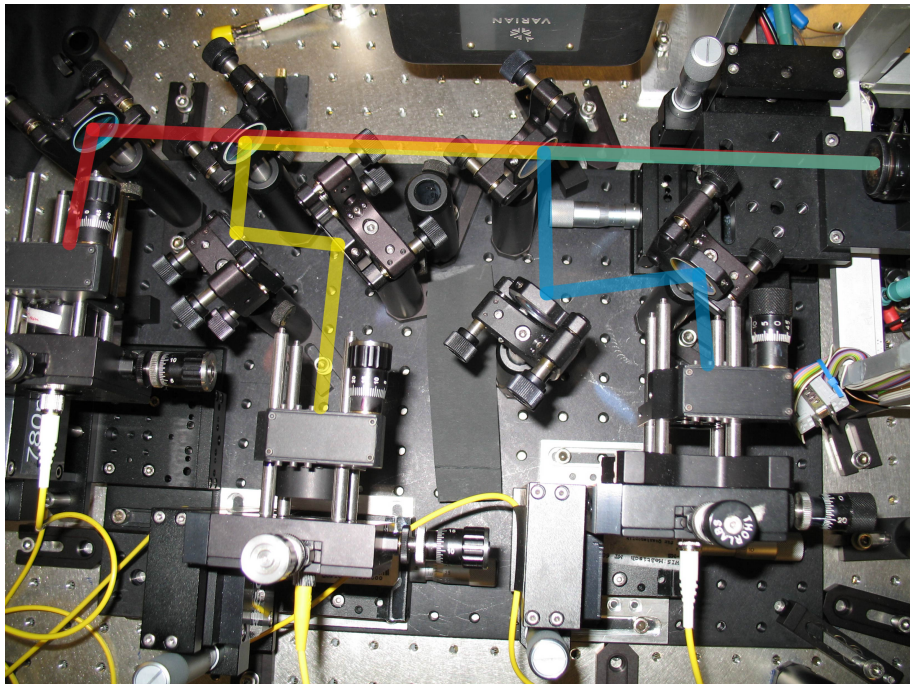


Figure A.6: Topview of the confocal microscope with the different beams, red fluorescence, yellow dipole trap beam, blue ionisation beam

# Bibliography

- [1] J. S. Bell. *Speakable and unspeakable in quantum mechanics*. Cambridge University Press, 1993.
- [2] Erwin Schrödinger. Die gegenwärtige Situation in der Quantenmechanik. *Die Naturwissenschaften*, 23:807–812, 823–828, 844–849, 1935.
- [3] A. Einstein, B. Podolsky, and N. Rosen. Can Quantum-Mechanical Description of Physical Reality Be Considered Complete? *Phys. Rev.*, 47(10):777–780, May 1935.
- [4] N. Bohr. Can Quantum-Mechanical Description of Physical Reality be Considered Complete? *Phys. Rev.*, 48(8):696–702, Oct 1935.
- [5] D. Bohm and Y. Aharonov. Discussion of Experimental Proof for the Paradox of Einstein, Rosen, and Podolsky. *Phys. Rev.*, 108(4):1070–1076, Nov 1957.
- [6] J. S. Bell. On the Einstein-Podolsky-Rosen paradox. *Physics*, 1964:195, 1964.
- [7] S. J. Freedman and J. F. Clauser. Experimental test of local hidden-variable theories. *Phys. Rev. Lett.*, 38:938–941, 1972.
- [8] J. F. Clauser and A. Shimony. Bell's theorem: experimental tests and implications. *Rep. Prog. Phys.*, 41:1881–1927, 1978.
- [9] A. Aspect, P. Grangier, and G. Roger. Experimental tests of realistic local theories via Bell's theorem. *Phys. Rev. Lett.*, 47:460–463, 1981.
- [10] A. Aspect, P. Grangier, and G. Roger. Experimental realisation of Einstein-Podolski-Rosen-Bohm Gedankenexperiment: A new violation of Bell's inequality. *Phys. Rev. Lett.*, 49:91–94, 1982.

- [11] A. Aspect, J. Dalibard, and G. Roger. Experimental test of Bell's inequality using time-varying analyser. *Phys. Rev. Lett.*, 49:1804–1807, 1982.
- [12] G. Weihs, T. Jennewein, C. Simon, H. Weinfurter, and A. Zeilinger. Violation of Bell's inequality under strict Einstein locality conditions. *Phys. Rev. Lett.*, 81:5039–5043, 1998.
- [13] Jürgen Volz, Markus Weber, Daniel Schlenk, Wenjamin Rosenfeld, Johannes Vrana, Karen Saucke, Christian Kurtsiefer, and Harald Weinfurter. Observation of Entanglement of a Single Photon with a Trapped Atom. *Physical Review Letters*, 96(3):030404, 2006.
- [14] M. A. Rowe, D. Kielpinsky, V. Meyer, C.A. Sacket, W. M. Itano, C. Monroe, and Wineland D.J. Experimental violation of Bell's inequality with efficient detection. *Nature*, 409:791–794, 2001.
- [15] M. Weber. *Quantum optical experiments towards atom-photon entanglement*. PhD thesis, Ludwig-Maximilians-Universität München, 2005.
- [16] J. Volz. *Atom-photon entanglement*. PhD thesis, Ludwig-Maximilians-Universität München, 2006.
- [17] J.-W. Pan, D. Bouwmeester, H. Weinfurter, and A. Zeilinger. Experimental entanglement swapping: Entangling photons that never interacted. *Phys. Rev. Lett.*, 80:3891–3894, 1998.
- [18] D. Bouwmeester, J.-W. Pan, H. Weinfurter, and A. Zeilinger. *The physics of quantum information*. Springer-Verlag, Berlin, 2000.
- [19] Markus Weber, Jürgen Volz, Karen Saucke, Christian Kurtsiefer, and Harald Weinfurter. Analysis of a single-atom dipole trap. *Physical Review A (Atomic, Molecular, and Optical Physics)*, 73(4):043406, 2006.
- [20] D. A. Steck. Rubidium 87 d line data. <http://steck.us/alkalidata>, 2001.
- [21] H. J. Metcalf and P. van Straten. *Laser Cooling and Trapping*. Springer, New York, Berlin, Heidelberg, 1999.

- 
- [22] J. J. Sakurai. *Modern Quantum Mechanics*. Prentice Hall, Englewood Cliffs, 1993.
- [23] Dariusz Chruściński. Geometric aspects of quantum mechanics and quantum entanglement. *Journal of Physics:Conference Series*, 30:9–16, 2006.
- [24] A. Einstein. *Philosopher-Scientist*. Open Court, La Salle, Illinois, 1970.
- [25] Eugen G. Wigner. On hidden variables and quantum mechanical probabilities. *Americal Journal of Physics*, 38(8):1005–1009, 8 1970.
- [26] F. A. Bovino, A. M. Colla, G. Castagnoli, S. Castelletto, I. P. Degiovanni, and M. L. Rastello. Experimental eavesdropping attack against ekert’s protocol based on wigner’s inequality. *Phys. Rev. A*, 68(3):034309, Sep 2003.
- [27] C.H. Bennett, G. Brassard, C. Crépeau, R. Jozsa, and A.and Wooters W. K. Peres. Teleporting an unknown quantum state via dual classical and Einstein-Podolski-Rosen channels. *Phys. Rev. Lett.*, 70:1985–1899, 1993.
- [28] H.-J. Briegel, W. Dür, J. I. Cirac, and P. Zoller. Quantum repeaters: The role of imperfect local operations in quantum communication. *Phys. Rev. Lett.*, 81(26):5932–5935, Dec 1998.
- [29] W. Pauli. Über den Einfluß der Geschwindigkeitsabhängigkeit der Electronenmasse auf den Zeemaneffekt. *Z. Phys.*, 31:373, 1925.
- [30] E. Arimondo, M. Inguscio, and P. Violino. Experimental Determinations of the Hyperfine Structure in the Alkali Atoms. *Reviews of Modern Physics*, 49:31–75, 1977.
- [31] S. Bize, Y. Sortais, M.S. Santos, C. Mandache, A. Clairon, and C. Salomon. High-accuracy measurement of the  $^{87}\text{Rb}$  ground state hyperfine splitting in an atomic fountain. *Europhys. Lett.*, 45:558, 1999.
- [32] G.P. Barwood, P. Gill, and W.R.C. Rowley. Frequency measurements on optically narrowed Rb-stabilised Laser diodes at 780nm and 795nm. *Appl. Phys. B*, 53:142, 1991.

- [33] J. Ye, Swartz, P. S. Jungner, and J.L. Hall. Hyperfine structure and absolute frequency of the  $^{87}\text{Rb}$   $5p_{3/2}$  state. *Opt. Lett.*, 21:1280, 1996.
- [34] C. Cohen-Tannoudji, J. Dupont-Roc, and G. Grynberg. *Atom-Photon Interactions, Basic Processes and Applications*. Wiley, New York, 1998.
- [35] D. Schlenk. Atom-Photon-Verschänkung. Master's thesis, Ludwig-Maximilians-Universität München, 2004.
- [36] N. Schlosser and P. Reymond, G.and Grangier. Collisional blockade in microscopic optical dipole traps. *Phys. Rev. Lett.*, 89:230051–230055, 1998.
- [37] E.L. Raab, M. Prentiss, A. Cable, S. Chu, and P.E. Pritchard. Trapping of neutral sodium atoms with radiation pressure. *Phys. Rev. Lett.*, 23:2631:2642, 1987.
- [38] R. Grimm, M. Weidemüller, and Y. B. Ovchinnikov. Optical dipole traps for neutral atoms. *Adv. At. Mol. Opt. Phys.*, 42:95, 2000.
- [39] C. Cohen-Tannoudji, B. Diu, and F. Laloë. *Quantum mechanics*. John Wiley & sons, 1977.
- [40] S. Hensler. *Wechselwirkungen in ultrakalten dipolaren Gasen*. PhD thesis, University of Stuttgart, 2004.
- [41] M. Aymar, O. Robaux, and S. Wane. Central-field calculations of photoionisation cross sections of excited states of Rb and  $\text{Sr}^+$  and analysis of photoionisation cross sections of excited alkali atoms using quantum defect theory. *J. Phys. B: At. Mol. Phys.*, 17:993–1007, 1984.
- [42] R. Unanyan, M. Fleischhauer, B.W. Shore, and K. Bergmann. Robust creation of an phase-sensitiv probing of superposition states via stimulated Raman adiabatic passage (STIRAP) with degenerate states. *Optics Communications*, 155, 1998.

- 
- [43] T.P. Dinneen, C. D. Wallace, N. K.-Y. Tan, and P.L. Gould. Use of trapped atoms to measure absolute photoionization cross sections. *Opt. Lett.*, 17:1708, 1992.
- [44] A. N. Klyucharev and V. Y. Sepman. Two-stage photoionization of rubidium. *Optics and Spectroscopy*, 38:712–713, 1975.
- [45] C. Gabbanini, S. Gozzini, and A. Lucchesini. Photoionization cross section measurement in a Rb vapor cell trap. *Opt. Lett.*, 17:1708, 1992.
- [46] Th. M. Miller. *Handbook of Chemistry and Physics*. CRC Press, Boca Raton, 2000.
- [47] K.E. Miller, D. Krause, Jr. Hunter, and L.R. Hunter. Precise measurement of the Stark shift of the rubidium and potassium D1 lines. *Phys. Rev A*, 49:5128, 1994.
- [48] C. Krenn, W. Scherf, O. Khait, M. Musso, and L. Windholz. Stark effect investigations of resonance lines of neutral potassium, rubidium, europium and gallium. *Z. Phys. D*, 41:229, 1997.
- [49] L. Ricci, M. Weidemüller, T. Esslinger, A. Hemmerich, C. Zimmermann, V. Vuletic, W. König, and T.W. Hänsch. A compact grating-stabilized diode laser system for atomic physics. *Optics Communications*, 117:541–549, 1995.
- [50] K. Saucke. Optische Dipolfalle für Einzelatome. Master’s thesis, Ludwig-Maximilians-Universität München, 2002.
- [51] F. Henkel. Fermionische Kalium in einer dreikomponentigen magnetooptischen Falle. Master’s thesis, Ludwig-Maximilians-Universität München, 2005.
- [52] C.C. Davis. *Laser and electro-optics*. Cambridge university press, 1996.
- [53] Paul Horowitz and Winfield Hill. *The art of electronics*. Cambridge University Press, second edition, 1989.
- [54] John Hawkes and Ian Latimer. *Lasers: Theory and practice*. Prentice Hall, 1995.

## Bibliography

---

- [55] T.F. Johnston. Beam propagation ( $M^2$ ) measurement made as easy as it gets: the four-cuts method. *Applied optics*, 37:4840–4850, 1998.
- [56] Jürgen Volz. Atom-photon entanglement. MPQ, Lehrstuhlseminar T. W. Hänsch, Ringberg 2006.
- [57] Henkel, Florian. private communication, 2007.
- [58] Volz, Jürgen. private communication, 2007.
- [59] Weber, Markus. private communication, 2007.
- [60] J. F. Clauser, M. A. Horne, A. Shimony, and R. A. Holt. Proposed experiment to test local hidden-variable theories. *Phys. Rev. Lett.*, 23:880–884, 1969.
- [61] D.J. Griffiths. *Introduction to quantum mechanics*. Prentice Hall, Englewood Cliffs, 1994.
- [62] J.D. Jackson. *Classical electrodynamics*. Wiley, 3 edition, 1998.

# Danke

”Leider läßt sich eine wahrhafte  
Dankbarkeit mit Worten nicht  
ausdrücken.”

*J. W. v. Goethe*

An dieser Stelle möchte ich mich bei allen bedanken, die mich während meiner  
Diplomarbeit und meines Studiums begleitet und unterstützt haben:

## Physiker

- Professor Harald Weinfurter für die Aufnahme in seine Gruppe, seine Inspiration und Geduld
- Dr. Markus Weber für seine organisatorischen Fähigkeiten und sein scheinbar grenzenloser Optimismus
- Dr. Jürgen Volz für seinen unermüdlichen Einsatz im Labor bis spät in die Nacht und seine Erklärungsversuche
- Florian Henkel für seine umfassende Betreuung innerhalb und außerhalb des Labors. Ohne Dich könnte ich bis heute keinen Post richtig anschrauben...
- Wenjamin Rosenfeld für seine umfassenden Bemühungen, mir Theorie beizubringen und die Einführung in Elektronik
- Fredrik Hocke für die dunklen Stunden im Labor...
- Allen Mitgliedern der Arbeitsgruppe: Danke für alle physikalischen und nicht-physikalischen Diskussionen im Laufe des letzten Jahres.

Der Belegschaft des K8 für das sichere Verwalten unseres Warenlagers.  
Was wären wir ohne Euch...

Daniel für die Geduld mit meinem Rechner und die erfolgreiche Reparatur  
der Kaffeemaschine

Jürgen für die kreative Kuchenbeschaffung und die erfolgreiche Reparatur  
der Kaffeemaschine

- Gabi, Nicole und Toni für alle Verwaltungs-, technischen und Elektronikfragen.  
Ihr hattet es manchmal echt schwer.
- Dirk Aschoff für die graphische Unterstützung
- Dirk, Ulrike, Max, Oli, Johannes, Simon, Felix, Julia, Nina, Yannis, Eleonora  
und viele mehr, die ich während meines Studiums begleitet und mir eine schöne  
Studienzeit beschert haben.

#### Nicht-Physiker

- Meike für die Geduld im letzten Jahr. Schön, dass es Dich gibt!
- Meiner Familie für die lebenslange Unterstützung
- Den Mitgliedern von *special guest* für den Soundtrack meines Lebens
- Dirk D. und Dirk A. für die schönen Ouzoabende
- Klaus und Tom für all die schönen Festivals
- Allen Freunden für den Beistand in schweren Zeiten
- Allen Freunden für die schönen Zeiten

Hiermit versichere ich, daß ich die vorliegende Arbeit selbständig und nur unter Verwendung der angegebenen Quellen und Hilfsmittel verfaßt habe.

München, den 20. Mai 2007

